Università degli Studi di Padova
Facoltà di Ingegneria

UNIVERSITÀ DEGLI STUDI DI PADOVA
FACOLTÀ DI INGEGNERIA

—

DIPARTIMENTO DI INGEGNERIA DELL'INFORMAZIONE

—

TESI DI LAUREA IN BIOINGEGNERIA

MODELS FOR THE PET QUANTITATIVE IMAGING OF THE ADENOSINE RECEPTOR RADIOLIGAND [^{11}C]SCH442416 IN HUMANS

RELATORE: CH.MA PROF. ALESSANDRA BERTOLDO
CORRELATORE: ING. GAIA RIZZO

LAUREANDA: ILARIA BOSCOLO GALAZZO

ANNO ACCADEMICO 2009-2010

To my family

Contents

Chapter 1

Introduction

Increasing life expectancy will inevitably lead to a raise in the incidence of neurodegenerative diseases, such as Alzheimer's disease (AD), Huntington's disease (HD) and Parkinson's disease (PD), with a social impact that can not be trascured. In particular, PD affects 1 in 500 of the general population and 1 in 100 of those individuals aged 60 or over: it is considered the second most common neurodegenerative disease after AD.

Beside several studies to investigate the aetiology and the pathogenesis of this illness, new potential treatments are being tested, in order to overcome the problematics showed by the traditional ones. In fact, current therapies for PD can be reasonably described as highly effective and at the same time inadequate: substantial, even if partial, improvements in the motor deficits of PD are reliably produced by standard therapies, which are primarily designed to boost dopaminergic signaling in the striatum. Usually, to increase the production of endogenous dopamine, its precursor, L-DOPA, is used but, even if all the dopaminergic therapies are effective in the initial stages of the illness, they become inadequate as the disease progresses, do not reverse non-motor symptomatology and become associated with adverse effects that are difficult to manage. In particular, the most irreversible adverse effect of chronic dopaminergic therapy is the development of involuntary jerking or writhing movements known as dyskinesias.

This latter shortfall of dopaminergic therapy has prompted a search for new nondopaminergic modulators of basal ganglia motor circuits that may provide

alternative or adjunctive treatment with a reduced side-effect profile. The basal ganglia is in fact involved in motor control and sensorimotor integration, and recent studies have demonstrated how dopamine and adenosine interact to modulate motor function at this level. In this background, the antagonists of the A_{2A} subtype of adenosine receptors have emerged as a leading candidate class of non-dopaminergic antiparkinsonian agents, based primarily on their functional effects of improving motor deficits in rodent and primate models of PD, as well as several preliminary clinical studies. In particular, their relatively restricted pattern of expression within the Striatum area likely contributes to the low side-effect profile observed thus far in PD patients and the results suggest that they can be used as a monotherapy or togheter with L-DOPA, interacting positively with this type of drug.

In our work, we have analyzed a dataset offered by the Imperial College of London: it is composed of six subjects (3 dyskinetic Parkinson's disease subjects, 2 Parkinson's disease subjects and 1 healthy control) who were scanned on a PET camera after the injection of a new tracer, [^{11}C]SCH442416. It is an antagonist of A_{2A} receptors whose kinetics in rodents and monkeys suggest its potential use for in vivo imaging of this subtype of receptors and, considered in its unlabelled form and so as a drug, it possible use as a new treatment for PD.

We performed the Positron Emission Tomography quantification at region of interest (ROI) level: the advantages are the good signal to noise ratio of the time activity curves and the existence of well-estabilished techniques for the estimation of the unknown parameters. One major drawback of this approach is the loss of resolution of the original PET image.

The aims of this work are manifold: first, the study of the main characteristics of this tracer, in order to compare the evaluations in human subjects with the ones found with ex vivo and in vivo experiments in rats and in monkeys (our set of data is relative to the first experiment in unhealthy subjects). The second, principal and main important objective is the estimation of the most parsimonious compartmental model to describe the kinetics of the tracer within the brain: we know that a compartment represents a space or volume in which the tracer is distributed, while rate constants link compartments and represent the various

rates of intercompartmental tracer exchange. The validity of a compartmental approach rests on the validity of some assumptions that may involve tracer administration, pharmacologic and metabolic properties of the radiotracer, or the heterogeneity/homogeneity of tissue.

To find the best compartmental structure we first resort to an input-output technique, which is usually referred to in PET literature as Spectral Analysis: it is able to identify the kinetic components of the tissue tracer activity without specific model assumptions. Starting from the result of this I/O model we defined some compartmental models, and through their comparison and evaluation we proposed one of them as the best structure to describe the activity of [^{11}C]SCH442416.

Finally, we tried to indagate the characteristics of the proposed compartmental model, in particular in order to find any possible correlations between the subjects, even if the reduced number of patients involved in the study impedes to apply the main methods of the statistical analysis. In this way the comparison is reduced to a simple observation of the different micro/macroparameters for each subject.

Chapter 2

The Adenosynergic System

Adenosine is present in all tissues of a mammalian organism where it modulates a variety of important physiological processes, in particular they involve an inhibitory tone of neurotransmission and neuroprotective actions in pathological conditions. The understanding of adenosine production and release in the brain is therefore of fundamental importance and has been extensively studied.
In this chapter, main events underlying adenosine biosynthesis as well as its important receptors are presented and discussed.

2.1 Main Characteristics of Adenosine

Adenosine is an endogenous purine nucleoside, composed of a molecule of adenine attached to a ribose sugar molecule.

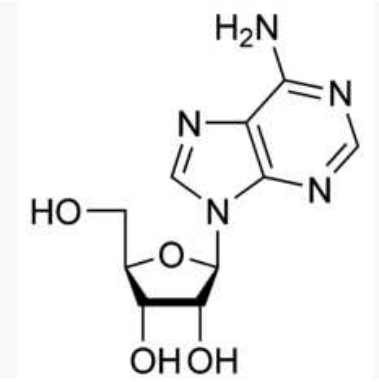

Figure 2.1: Adenosine: chemical structure

Over the past 25 years a general consensus has been reached on the crucial role of adenosine in the Central Nervous System (CNS) as a modulator of neurotransmission and a neuroprotective agent against neuronal injury. Moreover it has also been proposed to be a potent regulator of cerebral blood flow: so adenosine is mainly considered as a neuromodulator which is able to control the release of some neurotransmitters and to regulate many important biochemical processes [1]. In particular it is the major regulator of striatal functions, acting as an intrinsic signal since it is locally produced as a result of the activity of striatal circuits. Intracellularly, adenosine may be formed from degradation of adenosine monophosphate (AMP), and then may exit via bi-directional nucleoside transporters, whereas there seem to be two main sources for extracellular concentration. First, when there is an increasing workload of the circuit, a greater consumption of adenosine triphosphate (ATP) in neurons and astrocytes is required to maintain membrane potential. Dephosphorylation of ATP (present intracellularly in the millimolar range) generates adenosine, which levels increase substantially over basal intracellular levels: this build-up of intracellular adenosine is translated into increased levels of extracellular. This mechanism ensures that there is a local fluctuation of extracellular adenosine levels as a function of local activity in the striatum. There is also a second process which increases the concentration: it is connected to the degradation and metabolism of adenine nucleotides distributed in the extracellular space [2]. However, irrespective of its source, under physiological conditions extracellular adenosine concentration remains very low (nanomolar range) whereas traumatic or hypoxic events and increased neurotransmitter release lead to a several augmentation of adenosine levels.

Besides its more general involvement in cellular metabolism, specific actions of adenosine in the CNS as neuroeffector are believed to be mediated through some receptors, which have different characteristics and affinities for adenosine as we can see in the next paragraph.

2.2 Adenosine Receptors

The action of adenosine is mediated by specific receptors located on cell membranes, which belong to the family of G protein-coupled receptors, each with 7 transmembrane domains. Currently, four adenosine receptors have been cloned and characterized: $\mathbf{A_1}$, $\mathbf{A_{2A}}$, $\mathbf{A_{2B}}$ **and** $\mathbf{A_3}$. Each is encoded by a separate gene and has different functions, although with some overlapping, they have a widespread distribution all over the body and their recruitment is profoundly dependent on the specific pathophysiological situation, which can modulate the extracellular nucleoside concentrations ([3],[4]).

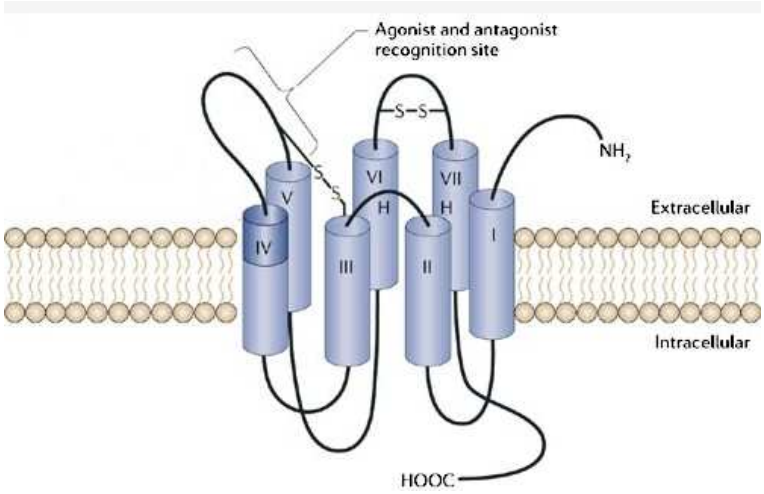

Figure 2.2: Adenosine receptor's structure

The *adenosine* A_1 *receptor* is activeted by nanomolar adenosine concentrations, this process of activation inhibits adenylyl cyclase (a lyase enzyme) and, as a consequence, the formation of cyclic adenosine monophosphate (cAMP, a second important messenger) [5].

This subtype is present on neurons and glial cells, both pre and postsynaptically: the highest expression has been found in the cortex, cerebellum, thalamus and hippocampus. Moreover it is also present in basal ganglia structures especially in striatum and here these receptors are present on dopaminergic and glutamatergic terminals, colocalized with dopamine D_1 receptors. A_1 receptors have been reported to mediate the protective effects of adenosine in preconditioning and during ischemia or during reperfusion injury in the brain (even if we have to

notice they are found in the entire body).

The *adenosine A_{2B} receptor* has long remained the least known subtype, it is sure it is expressed at low levels in all tissues and it has a low affinity for the natural ligand. This subtype activates adenylyl cyclase and so increase the cAMP: it is the less spread in brain areas.

The *adenosine A_3 receptor* behaves in a similar way to the A_1 subtype, although it needs much higher adenosine concentrations to be activated; it inhibits adenylyl cyclase and so the formation of cAMP. In appearent contrast with its low affinity for the endogenous ligand, this receptor seems to contribute to the defense mechanism during ischemic episode, together with A1 receptors. A_3 subtype is mainly present at intermediate levels in cerebellum and hippocampus areas. Finally it has been suggested that low-affinity receptors (A_3 and A_{2B}) may be activeted only under pathological conditions, when adenosine concentrations are markedly increased [5].

The most important subtype is *adenosine A_{2A} receptor*, which is a glycoprotein containing a single carbohydrate chain and has a molecular mass of 45 kDa: like the A_1 receptor, it binds adenosine with high affinity. This adenosine receptor makes an activation of adenylyl cyclase, leading to intracellular cAMP increase and resulting in stimulation of neuronal activity; this effect is mediated by a Gs type protein in the periphery, in platelets, neutrophils and lymphocytes whereas by a Golf subtype in the CNS. In contrast to the widespread distribution of the other subtypes, A_{2A} receptors are more selectively distributed in the brain, being abundantly expressed in striatum, globus pallidus, nucleus accumbens and tuberculum olfactorium; moreover they are present not only on neurons but also on the vessel walls where they mediate vasodilatation, on blood platelets, on other blood corpuscolar elements and on glial cells ([4],[6]).
Regarding to our research, this adenosine receptor plays the main important role, since the tracer of our interesting is specifically for this subtype. So in the next sections we will see better the distribution and the interaction of A_{2A} with other neurotransmitters.

In figure 2.3 it's represented the mechanism of coupling of adenosine to its receptors and its consequences.

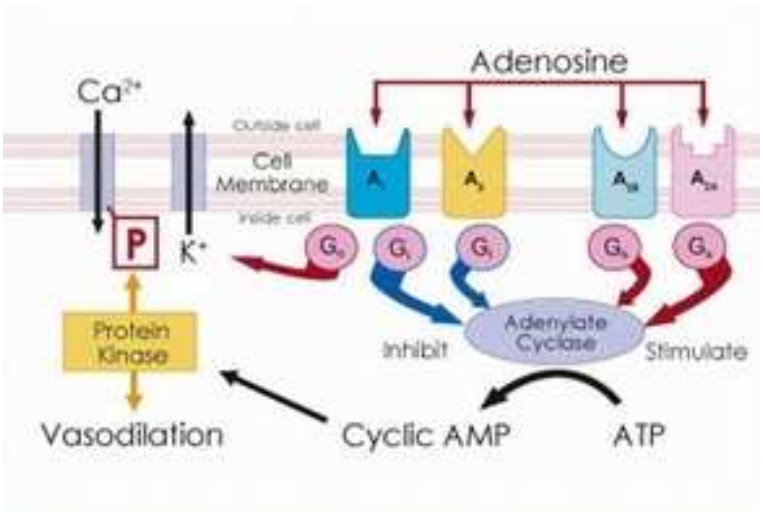

Figure 2.3: Adenosine receptor coupling

2.3 A_{2A} Receptors and Basal Ganglia

The basal ganglia are a richly interconnected neural network involved in adaptive control of behavior through interactions with sensorimotor, motivational and cognitive brain areas: the striatum, which is composed of putamen and caudate nucleus, is the major input structure of the basal ganglia. The other structures that compose the basal ganglia are globus pallidus, subthalamic nucleus and substantia nigra [2].

Ninety percent of striatal neurons are medium-size spiny neurons, named for their high density of dendritic spines. These are the population of GABAergic striatal efferent neurons, which are equally divided into two groups: *GABAergic enkephalinergic* (striatopallidal) and *GABAergic dynorphinergic* (striatonigral) neurons. They give rise to two striatal efferent pathways, which connect the striatum with the output structure, called "direct" and "indirect" pathways. In the first case, GABAergic dynorphinergic neurons directly connect the striatum with the substantia nigra pars reticulata (SNr) and the internal segment of the globus pallidus (GPi). The indirect pathway instead consists of GABAergic enkephalinergic neurons, which connect the striatum with the external segment of the globus pallidus (GPe), which in turn project to the subthalamic nucleus (STN) and then this connects to the output structures. Because of these differences in connectivity,

stimulation of the direct pathway results in motor activation and stimulation of the indirect pathway produces motor inhibition.

As we said before A_{2A} receptor expression is considerably enriched in the striatum and also within the striatum in the population of GABAergic enkephalinergic neurons, and so involved in the indirect pathway, together with D_2 dopamine receptors, both pre and postsinaptically (instead, the other subpopulation of neurons contains adenosine A_1 and dopamine D_1 receptors). Moreover the A_{2A} receptor is enriched in all dopamine rich areas of the brain. The discovery of the colocalization of D_2 and A_{2A} receptors has provided the demonstration of the functional antagonism between adenosine and dopamine in the basal ganglia, probably because they are both coupled with adenylyl cyclase, but with opposite effects. So under physiological conditions, activation of A_{2A} receptors is responsible of the increase of cAMP, on which dopamine can exert its inhibitory action: the activation of the adenosine receptor induces hypolocomotion, while the opposite is observed after D_2 stimulation. The study of adenosine/dopamine interaction has provided the molecular and biochemical basis to postulate the possible therapeutic use of A_{2A} receptors antagonists in Parkinson's disease (PD).

About **Parkinson's disease** it is known that is age related and this remains the only clearly estabilished predisposing factor. It is characterized by akinesia, rigidity, tremor and postural abnormalities, but increasingly there is awareness that it is a much broader illness that induces also non-motor symptoms such as falling, speech difficulties and neuropsychiatric components like depression, anxiety and cognitive decline [7]. Many of these features can precede the onset of motor symptoms and they are being investigated as early diagnostic features of PD. The motor symptoms of PD are due primarily to the degeneration of the dopaminergic nigrostriatal pathway, in fact there is the progressive damage of dopaminergic neurons in the substantia nigra, even if the pathology is widespread, with cell loss also occurring in many other brain areas. Unluckly the clinical symptoms appear after approximately 60% of the dopaminergic neurons are damaged and the dopamine concentration in the striatum drops by about 80%: for this reason new tecnologies and methods to early recognize this illness are of great interest and are being developed in these last years. The current therapy for PD is based

on dopaminergic replacement using L-DOPA and dopamine agonists, these lead to almost complete reversal of motor symptoms in the early stages of the disease, even if the dopamine agonists do not possess a great efficacy. Moreover with the disease's progression and chronic drug treatments the dopaminergic drugs show a shortening of duration of effect and a significant part of patients develop involuntary movements of dyskinesia, particularly when treated with L-DOPA. Finally, the major limitations of the current pharmacological treatment of PD is represented by its substantial ineffectiveness in counteracting the degeneration of dopaminergic neurons. In this regard, it has recently been emphasized that the blockade of adenosine A_{2A} receptors may potentially represent a valuable approach in counteracting neuronal death in PD, as explained below.

2.4 A_{2A} Antagonists and Parkinson's Disease

To understand how this adenosine antagonist can be useful in treatment of PD, it is better to start from the analysis of the normal condition.
As we said before, the basal ganglia are thought to mediate the learning and processing of motor acts through the balance of the direct (striatonigral) and the indirect (striatopallidal) pathways. In the normal state, dopamine facilitates motor activity both by exciting D_1 receptor expressing neurons in the direct pathway and by inhibiting D_2 receptor expressing neurons in the indirect pathway. Adenosine excites neurons in the indirect pathway via adenosine A_{2A} receptors in the striatum and globus pallidus pars externa (GPe): there are evidences that activation of these receptors decreases the affinity of D_2 for dopamine. So the inhibitory influence of the striatonigral direct pathway on output, composed of substantia nigra pars reticulata and globus pallidus pars interna (SNr/GPi complex), is counterbalanced by the disinhibitory influence of the striatopallidal indirect pathway to this complex (Figure 2.4 - left side).

In PD, dopamine deficiency causes reduced activation of the dopamine receptors, which results in reduced inhibition of neurons of the indirect pathway and decreased excitation of the direct pathway neurons: striatopallidal neurons, loosing the inhibitory effect of dopamine while undergoing the stimulatory influence

of adenosine, become hyperactive, while striatonigral ones become hypoactive. Such imbalanced activity leads to a markedly increased inhibitory output from SNr/GPi complex to thalamocortical neurons, which produces reduced movements of PD (Figure 2.4 - middle part).

Many authors have suggested that the positive effects of A_{2A} antagonists in PD rely on the blockade of this subtype of receptors on striatopallidal neurons, which should dampen their excessive activity and restore some balance between the two pathways, consequently relieving thalamocortical activity ([6],[7])(Figure 2.4 - rigth side). However the reduced activity in the direct pathway would not be normalized by blocking sdenosine A_{2A} receptors and so the motor deficits in PD may be only partially reversed by these antagonists alone. Significantly, the use of A_{2A} antagonists can occur with no risk of the development or expression of dyskinesia.

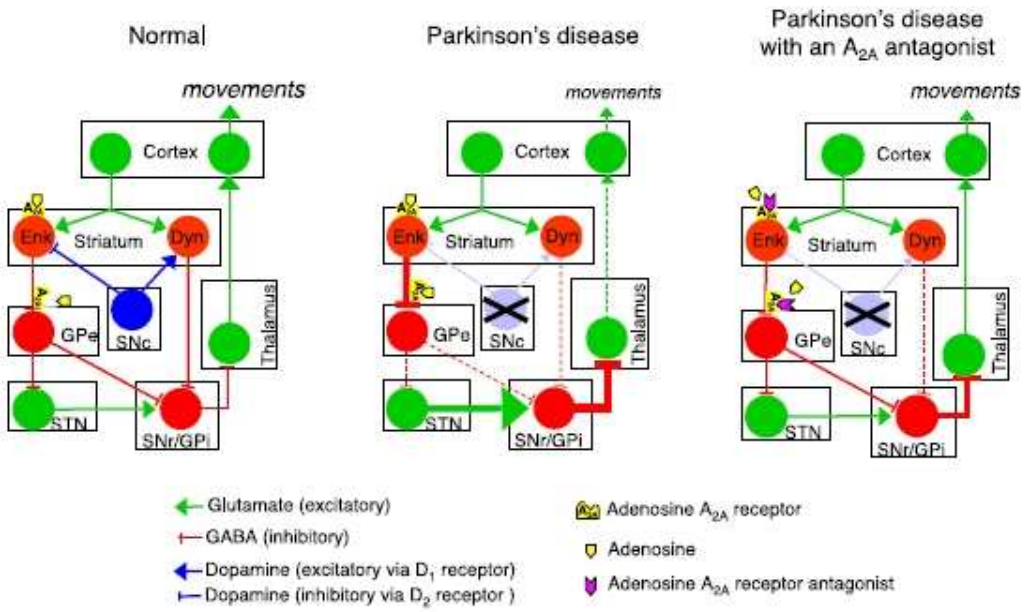

Figure 2.4: Schematic representation of adenosine A_{2A} receptor antagonist activity in Parkinson's disease. Abbreviations: Dyn, dynorphin; Enk, enkephalin; GPe, globus pallidus pars externa; GPi, globus pallidus pars interna; SNC, substantia nigra pars compacta; SNr, substantia nigra pars reticulata; STN, subthalamic nucleus [6]

Moreover A_{2A} blockade may contribute to counteract tremor and attenuate

dopaminergic cells' degeneration (neuroprotection) through a mechanism that may involve the receptors located presinaptically or on glial cells.

Finally, data obtained from several preclinical studies indicate the existence of beneficial effects of chronic A_{2A} antagonists on patients with PD who have also developed dyskinetic complications after a long L-DOPA therapy. So they can be used alone or in combination with dopaminergic drugs. However, although the neuroprotective and neuroexcitatory effetcs of adenosine A_{2A} antagonists on parkinsonian neuronal demise appear to be most promising, it should be noted that (i) activation of A_{2A} receptors produce vasodilation (ii) by acting on A_{2A} receptors on inflammatory cells, adenosine produces anti-inflammatory responses, and (iii) by acting on A_{2A} receptors on endothelial cells, adenosine decreases endothelial permeability. Therefore, blockade of A_{2A} receptors may produce adverse effects in regions other than the brain, such as the heart, kidney, lung and inflammatory responses in general [6].

Chapter 3

Positron Emission Tomography

In the last decades, the evolution of medicine has demanded new ways of imaging which can improve the knowledge on tissues and body's organs in comparison with the simple morfological observations. In this chapter, we will focus our attention on the characterists and principles of an important imaging technique, called *Positron Emission Tomography* (PET), which is moving from the research domain to clinical applications for oncology, neurology and cardiology.

3.1 Basic Principles of PET Imaging

Positron Emission Tomography is a nuclear imaging modality that excels in depicting the biology of living tissue and that enables regional function to be assayed in a fully quantitative and noninvasive manner. While the resolution of magnetic resonance imaging (MRI) for structural tissue changes is unsurpassed, the ability of structural MRI to demonstrate alterations in the physiology and metabolic function of tissues remains poor. For this reason, combining the functional PET data with with the high-resolution anatomical maps produced by MRI provides powerful data sets which allow corrispondences to be identified and analyze in a better way the different structures [8]. This combination of techniques is recommanded especially for the brain, as in our study, since it is a complex neuronal network in which all subunits can communicate directly or indirectly with each other.

This nuclear technique involves the introduction, usually via an intravenous injection, of a radioactive tracer into the human body: a tracer is essentially a biological compound of interest labelled with a positron-emitting isotope,where a positron is a particle with the same mass and charge of an electron, but opposite sign (it's the electron's antiparticle). The isotopes usually used are ^{11}C, ^{18}F, and ^{15}O, because they have relatively short half-lives (minutes to less than two hours), allowing the tracers to reach equilibrium in the body, but without exposing the subjects to prolonged periods of radiation.
They are prepared in a cyclotron that accelerates a beam of protons and directs it towards the target nuclei, thereby incorporating an extra proton into them: this generates new compounds that are energetically unstable. The isotopes are then coupled to the compound of interest and that is the tracer. Since they are unstable, the isotopes undergo a process of decay whereby the excess proton is converted into a neutron, a positron, and a neutrino: the emitted positron travels up to a range of a few millimetres in tissue before annihilates with an electron [9](Figure 3.1 a). This mutual annihilation process produces two 511 keV γ rays going in opposite directions (they are released at 180) and which are detected by the several rings of PET scanner. This consists of circumferential arrays of detectors which look for coincidence events, in witch two γ ray interaction occur almost simultaneously on opposite side of the head (Figure 3.1 b).
Finally, through reconstruction software the tomographic image is obtained: the count density in the resulting images, assuming appropriate data corrections are applied, reflects the concentration of the positron-emitting isotope in the tissue.

The main characteristics that make PET a charming technique in the neuroimaging field are superior sensitivity, high quantity of information and a greater flexibility of incorporating positron labels into biomolecules. On the other side, the main disadvantage of PET is greater expense in comparison with other techniques.

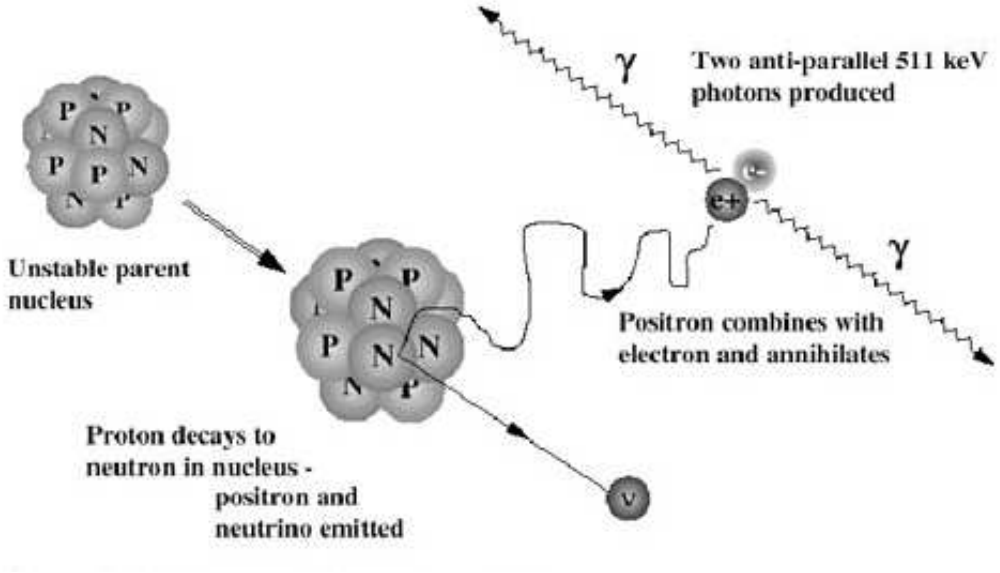

(a) Positron emission and annihilation

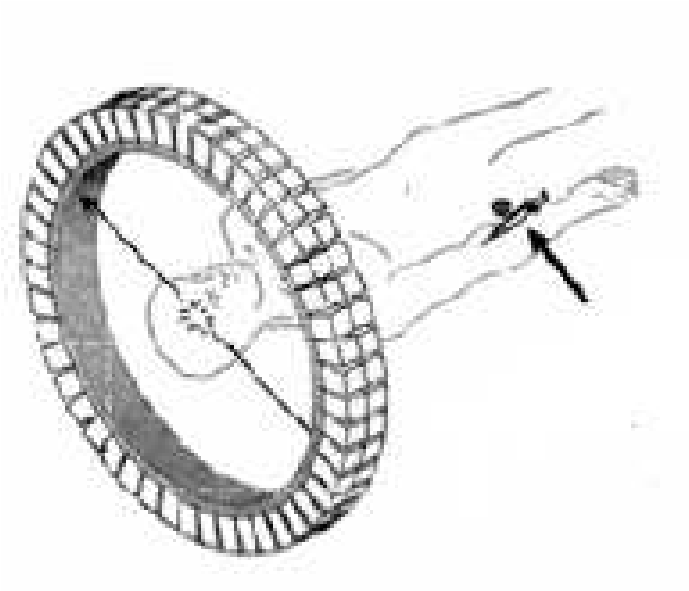

(b) Schematic representation of detectors in PET

Figure 3.1: The main principles of PET imaging

3.2 PET tracers

As we said before, a tracer is an indicator molecule that follows a systemic substance that might be involved in flow, metabolism or drug-binding processes. The tracer properties should be analogous to the systemic substance and it should be introduced into the system in small amounts and not perturb it. Actually different kinds of tracers exist and are chosen to illustrate the particular brain functions the investigators are interested in: for example [^{18}F]FDG is commonly used to study the glucose metabolism and [^{15}O]H_2O to stimate cerebral blood flow [11]. All the positron-emissing isotopes used are characterized by short half lives (Table 3.2) and this is ideal for medical imaging purposes. In fact, if the half life is too short there is not sufficient time to label the compound of interest and get the dose to the patient before it decays away; on the other side, if the half life is too longer many of the positrons are emitted after the patient has left the scanner. However the short half life of positron emitter limits the PET technology to centers with an on-site cyclotron unit and a nuclear chemistry laboratory: also for these reasons, it is mainly considered an expensive technique and often limited to the research area.

Isotope	**Half-Life (min)**
Carbon-11	20.4
Nitrogen-13	9.96
Oxygen-15	2.07
Fluorine-18	109.8

Table 3.1: Common positron-emitting isotopes used

A lot of studies are undergoing in order to develop new tracers with characteristics suitable for molecular imaging of particular metabolic, biochemical or physiological functions. In particular some specific tracers, like [^{11}C]SCH442416 and [^{18}F]DOPA, are being studied to evaluate different receptor systems: in vivo receptorial studies with a PET tracer allow for example to calculate parameters like distribution volume or binding potential and to assess the penetration

through the blood brain barrier (BBB).
However radioligands suitable for PET studies should fulfill several criteria, in particular the properties of an ideal tracer include

receptor affinity in the nanomolar range (high affinity);

high selectivity for the studied process;

permeability across BBB;

high specific uptake in target tissue;

low nonspecific binding.

All these characteristics ([10]) are being investigated in vitro e in vivo also in [^{11}C]SCH442416, which is a new radioligand used in this research work, as we will see in the next chapters.

The analysis of PET images obtained with one of these tracers can be qualitative, through visive ispection, or quantitative, in this case a mathematical model or a specific method are required. Tracer kinetic models in PET provide the mathematical framework to calculate the concentration of reactants and products, and the rate of a biological process, based upon the time course of tracer distribution in a series of images and the blood concentration of tracer.
Among these, compartmental models are the most common used in PET area, as we will largely discuss along this thesis.

3.3 PET and [^{11}C]SCH442416

After describing the general principles and functions of positron emission tomography, in the next sections we will focus on the characteristics of this new potent radioligand, which seems to be the first tracer suitable for in vivo imaging of adenosine A_{2A} receptor, giving also some information about the state of art.

3.3.1 Structure and biological profile of [^{11}C]SCH442416

As explained in Chapter 2, the adenosine A_{2A} receptor subtype is selectively expressed in some brain's areas, in particular the high level is reached in the

striatum, where it is functionally linked to dopamine D_2 receptors. Experimental evidence indicates that in striato-pallidal neurons the administration of adenosine A_{2A} receptor agonists decreases the affinity of dopamine for D_2 receptors. These findings suggest that adenosine A_{2A} receptor antagonists may be useful in the treatment of Parkinson's disease and so in the last years an increasing number of antagonists for this subtype has been evaluated and developed.

To better understand it is important to underline the difference between an agonist and an antagonist in pharmacology. An *agonist* is a substance that binds to a specific receptor of a cell and mimics the response of the natural endogenous ligand: there is the activation of the receptor. Also the *antagonist* binds to a specific receptor but does not active it and does not provoke a biological response, it has affinity but no efficacy on the receptor and it blocks the binding of the corrispondent agonist or natural ligand: so there is the inhibition of the receptor.

Several xanthine derivatives with antagonist activity for A_{2A} receptors have been labeled with positron-emitting isotopes, for example [^{11}C]CSC is highly selective, but its affinity for this subtype is relatively low, instead [^{11}C]KF17837 has higher affinity for but a low striatum-to-cerebellum ratio was found when tested in vivo with PET. Among the [^{11}C]-labeled xanthine ligands the most suitable ligand for PET application appears to be [^{11}C]KF18446, which shows good in vivo selectivity and specificity for the target tissues. Neverthless, the above compounds are xanthine derivatives and are subject to photoisomerization, which is a specific drawback of this class of molecules [10].

To avoid these problems, recently some novel non-xanthine compounds with antagonistic properties toward the adenosine A_{2A} receptor subtype have been synthesized. Among them, the most important compound is SCH442416 used in its [^{11}C] radiolabelled form (molecular formula $C_{20}H_{19}N_7O_2$, Figure 3.2).

Biodistribution studies indicate that all over the body [^{11}C]SCH442416 preferentially accumulates not only in adrenal glands and kidneys, where A_{2A}receptors are highly expressed, but also in lung and liver, instead tracer accumulation is lower in the heart, where adenosine receptors are mainly represented by the A_1 subtype. Concerning the brain, which is the organ of interest for our work, the results clearly show that this tracer permeates the BBB and accumulates in some

brain's areas, in agreement with the known regional distribution of adenosine receptors [10].

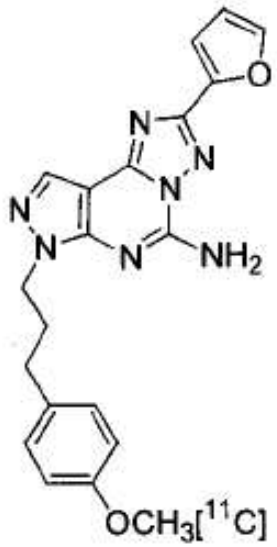

Figure 3.2: [^{11}C]SCH442416: chemical structure

3.3.2 In vitro and in vivo evaluation of [^{11}C]SCH442416

In the first receptor-binding study by Todde and coworkers on human cells and tissues [10], the affinity of this tracer for A_{2A} receptors expressed by the parameter K_i was 0.048 nM, >10.000 for A_{2B} and A_3 and 905 nM for A_1: so this tracer showed a good selectivity and high affinity for the target receptor subtype. The next step was the evaluation in vivo, first on rodents ([12]): in addition to confirm the results previously reported, these tests found that in all areas the time of maximum uptake was reached 5 min after the injection, moreover [^{11}C]SCH442416 mainly accumulated in the striatum (Figure 3.3 a), whereas in the remaining brain regions examined the tracer distribution was lower and homogeneous (this is in accordance with the localization of A_{2A} receptors). It displayed a good striatum to cerebellum radioactivity concentration ratio and this reached the maximum value (4.6±0.27) 15 min after the injection. Analysis of plasma extracts showed the presence of three main radioactive compounds, one more lipophilic and two hydrophilic compounds, probably attributable to metabolites; the metabolism of

[^{11}C]SCH442416 revealed to be slow and the plasma concentration of the injected tracer accounted for more than 40% of total plasma activity after 60 min.
Moresco and coworkers [12] in one of their studies on rats decided also to inject an intrastriatal dose of quinolinic acid (QA), that it is known produces a selective destruction of striatal neurons, included GABA enkephalinergic neurons which express A_{2A} receptor subtype. So the QA induced a reduction of striatal A_{2A} receptors (Figure 3.3 b) and in particular two weeks after the operation they observed a 50% decrease in striatum to cerebellum radioactivity concentration ratio, in comparison with control rats.

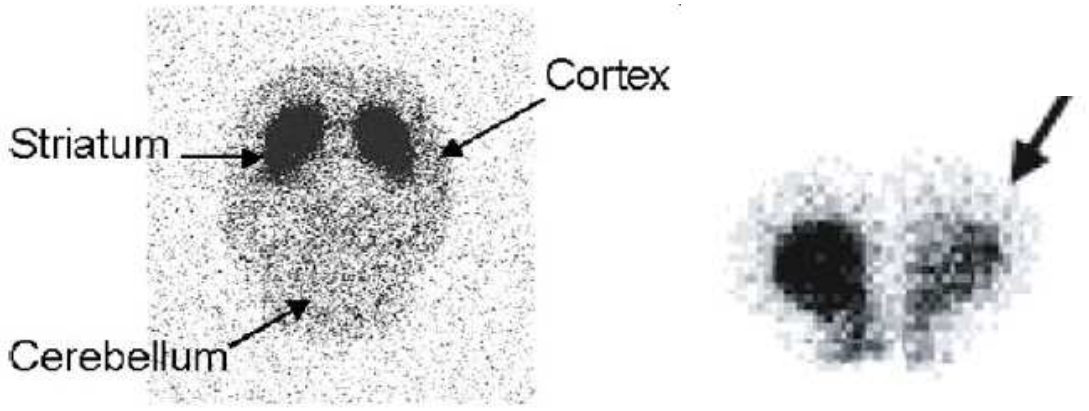

(a) Transaxial image: high binding in striatum area

(b) Coronal image from an unilaterally quinolinic acid (QA)-treated rat(arrow=injected side)

Figure 3.3: Autoradiography of brain sections obtained at the level of the basal ganglia after an intravenous injection of [^{11}C]SCH442416 in rats.

This group also performed a study on monkeys and the results were similar: as previously, they found a rapid brain uptake, in particular reaching in striatum the maximum value between 2-4 min after the injection and then declined.Striatum to cerebellum ratio increased with time, reaching a maximum value of 2.2 at about 15 min (as observed in rats); this value was only slightly reduced during the following minutes. Also in monkeys, the radioactive compounds present in the plasma extracts were the same previously observed in rats and also in this case the metabolism was slow([12],[13]). However, the PET experiment on monkey's brain indicated the presence of a high fraction of non specific binding, in fact

it was noted the striatum to cerebellum ratios were two times lower than those measured in rats. We have to underline that in all these studies they used the cerebellum as a reference region because in this area the number of A_{2A} receptors is negligible and they found low values of tracer uptake.
In Figure 3.4 we report as an example the tipical curves of concentration of some regions of interest, which are related to the experiment made by Moresco et al. on rats and monkeys.

In conclusion, the regional distribution in brain and also in periphery, the good signal to noise ratio, the low presence of radioactive metabolites and the good striatum to cerebellum ratios(even if values are a bit low) suggest that [^{11}C]SCH442416 is applicable as the first nonxanthine, highly selective ligand suitable for the in vivo imaging of adenosine A_{2A} receptors using PET.

Data used in this work regard the first in vivo quantification of A_{2A} receptors in human subjects with Parkinson's disease: recently, Brooks and his coworkers also have used this tracer, in healthy subjects, but their aim was to demonstrate the efficacy of a new drug, vipadenant, as a potential treatment of Parkinson's disease [14]. They found the binding of this tracer was blocked after some oral administrations of vipadenant (which binds to the same receptor subtype); they also proposed a kinetic model and calculated some important parameters, as distribution volume. Finally, specific [^{11}C]SCH442416 binding to the cerebellum brought them to preclude its use as a reference region, in disagreement with precedent results on animals.

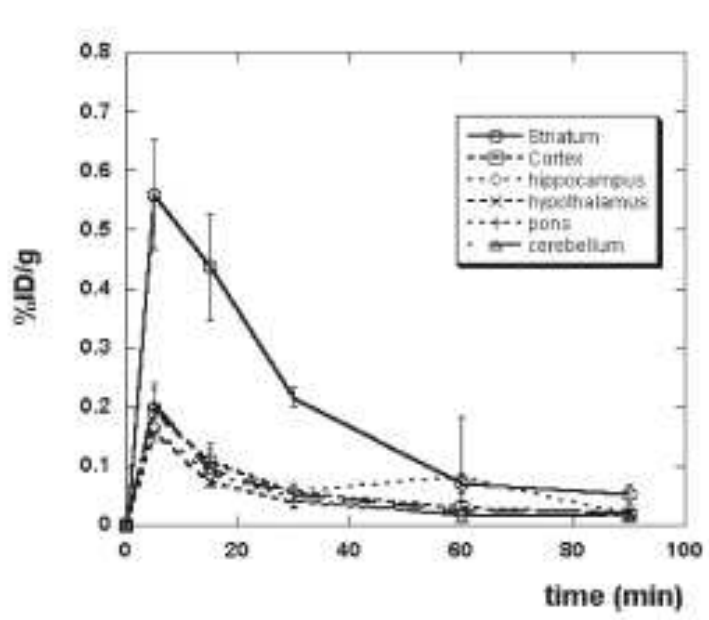

(a) Rats

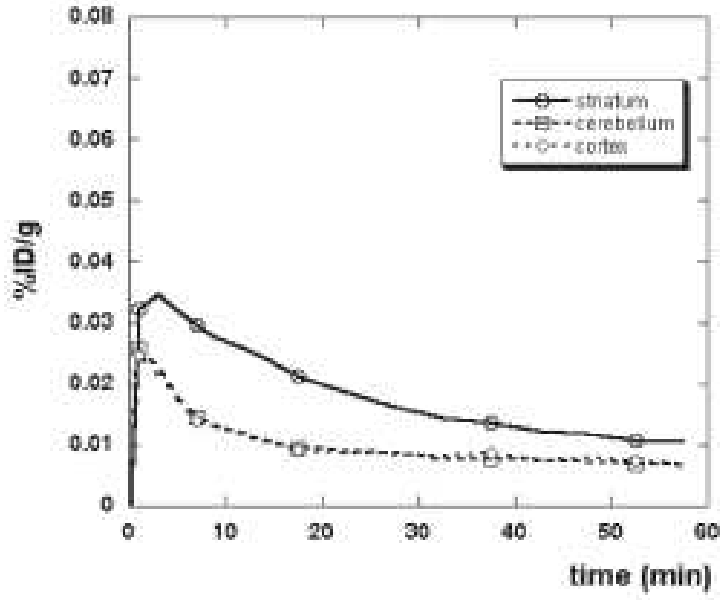

(b) Monkeys

Figure 3.4: Tipical time course of regional radioactivity concentration present in literature. % ID/g represents the percentage of injected dose per gram of tissue.

Chapter 4

[^{11}C]SCH442416: Subjects and Sperimental Data

In this chapter we present the data used for the quantitative analysis, the protocol and the subjects.

4.1 Protocol and Subjects

PET experiments were performed at Hammersmith Imanet, London, using ECAT EXACT HR+ (Siemens/CTI, Knoxville, TN): this scanner consists of four rings, each made up of 72 block detectors. The ring diameter is 82.7 cm and the axial field of view (FOV) is 15.5 cm; the entire brain can be imaged simultaneously with a spatial resolution of 4-5 mm.
The number of slices acquired by this tomograph was 63, and for each slice the protocol expected 34 frames of different length, in particular it respected the following time grid: 1 x 30 sec, 6 x 10 sec, 3 x 20 sec, 3 x 30 sec, 4 x 1 min, 6 x 2 mins, 8 x 5 mins, 3 x 10 mins, for a total of 90 mins. Moreover all subjects underwent a T1 weighted MRI of the brain, useful to have information about the region of interest (ROI) placement and to examine the structure of the brain.

This study involved six patients, each with a particular clinical history: in table 4.1 we report the diagnosis for each subject and the dose of radioactivity injected for the analysis, even if for one subject we do not have the last information.

Number	Subject	Diagnosis	Injected dose(MBq)
1	1814	Parkinson's disease with Dyskinesia	656.28
2	1711	Parkinson's disease	-
3	2241	Parkinson's disease with Dyskinesia	588
4	1804	Parkinson's disease	485.45
5	1866	Parkinson's disease with Dyskinesia	656.99
6	2300	Healthy	635

Table 4.1: Subjects involved in the study. Dyskinesia involves uncontrolled and unusual movements of the body, it often spreads after a long treatment with L-DOPA drug.

4.2 [11C]SCH442416 Data

4.2.1 [11C]SCH442416 Blood Sample Analysis

Arterial blood sampling was initiated concurrently with the start of the tracer infusion and samples were automatically collected during all the experiment using a flow-through monitoring system that measures the radioactivity, so we have about 5400 samples for each subject. Also the total plasma (i.e without red cells) radioactivity concentration is measured.
Additionally, other 9 (or 8 in same cases) blood samples were collected at specific time points throughout the study and used to determine the fraction of unmetabolized [11C]SCH442416 (of total plasma radioactivity concentration) using high-performance liquid chromatography HPLC. Plasma data were corrected for the presence of radiolabeled metabolites of the tracer using the HPLC data: the parent plasma concentration was obtained. So for each subject we have, besides the fraction of radioactive metabolites, the radioactivity concentration in total blood $C_b(t)$, in total plasma $C_{tp}(t)$ and in parent plasma $C_p(t)$.

In Figure 4.1 we report for each subject the time course of parent compound measured in plasma, i.e the fraction of unmetabolized tracer. From the observation of the curves, it is clear the difference with results already present in

literature, in fact while during previous evaluation in vivo on animals, a low metabolism and a big amount of unmetabolized tracer even at the end of the experiments were found, here we can observe a rapid decrease and after 7 mins, on average, the fraction of unmetabolized [^{11}C]SCH442416 in plasma decreases by approximately 50%.

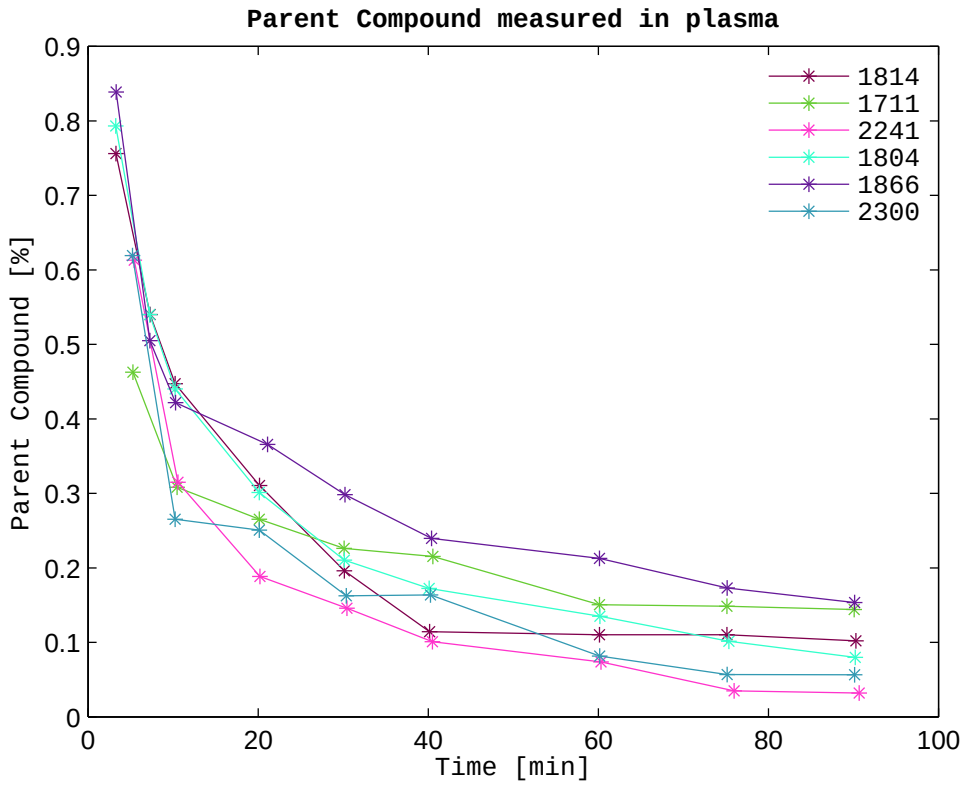

Figure 4.1: Parent compound

All blood signals were first corrected for the presence of delay, which is due to a comprehensive difference between the tracer arrival in the brain and the arterial sampling site and can greatly influence the goodness of estimates if not taken into account. In Table 4.2 we report the delay values stimated for the subjects: for subject 2300 (control), since we did not have the precise value, we applied to the arterial input function some different values (from 7 to 15 secs) and, fitting the time-activity curve of some regions of interest with a simple two-tissue compartmental model, we selected the delay time that minimized the Akaike Information Criterion (AIC).

Subject	Delay (sec)
1814	7
1711	13
2241	15
1804	14
1866	7
2300	7

Table 4.2: Delay values for the 6 subjects

Moreover, all blood misures were corrected for the decay, using the formula

$$A_0 = A_t \times e^{\lambda t} \tag{4.1}$$

where A_t and A_0 are respectively the uncorrected and corrected value of concentration at time t, which is expressed in minute, $\lambda = \frac{\ln 2}{T_{1/2}}$ with $T_{1/2}$ half-life of the radioactive isotope (in our case 20.4 mins).

4.2.2 PET data

PET data were corrected for attenuation and scatter; 43 Regions of interest (ROIs) were drawn and applied to the dynamic PET data to generate time activity curves. The following ROIs were considered: Hippocampus, Amygdala, Anterior Temporal Lobe-medial part, Anterior Temporal Lobe-lateral part, Parahippocampal and Ambient Gyri, Superior Temporal Gyrus, Middle and Inferior Temporal Gyrus, Occipital Temporal Gyrus, Cerebellum, Brainstem, Insula, Occipital Lobe, Anterior Cingulate Gyrus, Posterior Cingulate Gyrus, Frontal Lobe, Posterior Temporal Lobe, Parietal Lobe, Caudate nucleus, Nucleus accumbens, Putamen, Thalamus, Pallidum.
Each region, expect Brainstem, is separately considered in its left and right part. In our work, we applied the different models and methods to all ROIs, but the most relevant ones are the regions closely connected with the distribution of adenosine A_{2A} receptors, i.e Caudate Nucleus, Putamen, Nucleus Accumbens, Pallidum where this subtype is particulary aboundant and Cerebellum, Thala-

mus, Anterior Cingulate Gyrus where the distribution of receptors is negligible. To undestand where these areas are collocated in the human brain, we report in Figure 4.2 some T_1 weigthed MRI slices, relative to subject 1711.

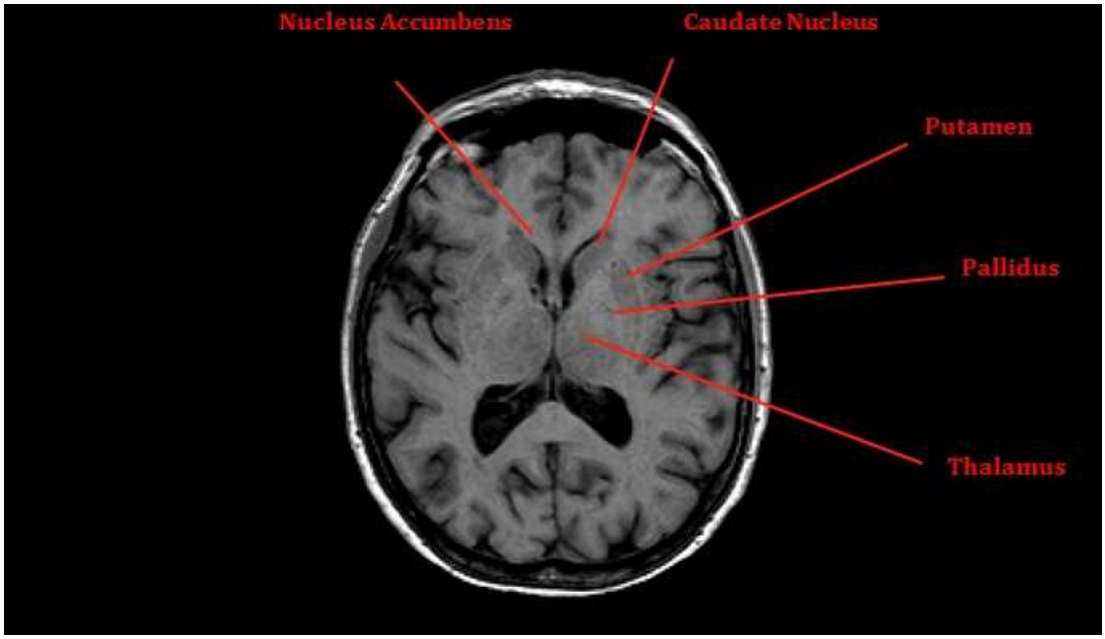

(a) Transaxial view-Slice 83

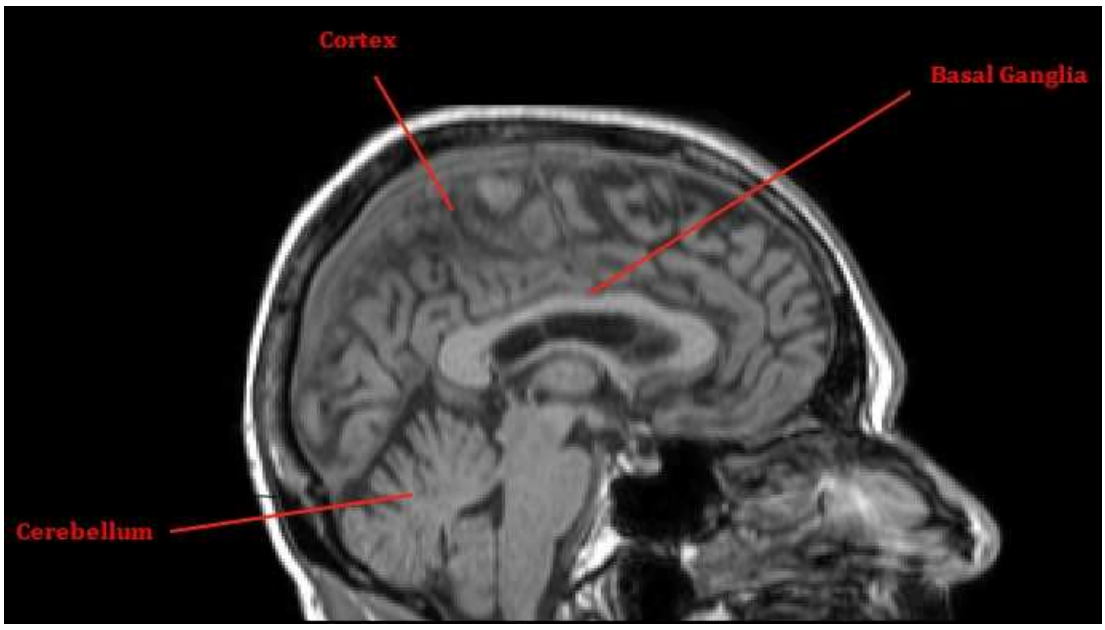

(b) Sagittal view-Slice 128

Figure 4.2: Different slices from subject 1711 showing the position within the brain of the most important areas for our work

For each subject, PET image was transfered to Matlab and we obtained a 4D matrix, 128x128x63x34 where 63 is the number of slices and 34 the number of frames of different length. We made a first qualitative analysis, in order to see the distribution of tracer in the brain, so after summing multiple time frames, we made a mask to limite the noise in the images obtaining in this way new summed PET images. Usually the sum of first minutes is made, because it better reflects the arrival and distribution of tracer, but in our case, after trying different combinations of sum, we did not find significant differences in the resulting summed PET images and so we decided to consider the sum from 0 to 90 mins after the tracer injection. From the observation of summed PET images, it is clear that there is a rapid uptake of [^{11}C]SCH442416 in the brain, following the known regional distribution of A_{2A} receptors, in particular, as we can see in Figure 4.3, tracer rapidly accumulates in Striatum - Globus Pallidus whereas in the other regions the accumulation of radioactivity is significantly lower. So the internal structures show higher activity than cortical brain areas.

Finally, the decay correction, as before explained for the blood misures, was applied to the data relative to each region of interest, generating the tissue-time activity curves (TACs): in Figure 4.4-6 for the 6 subjects we represent in the left column the total blood curve ($C_b(t)$) and the parent plasma curve ($C_p(t)$), which are corrected for delay and decay, instead in the right column there are some decay corrected TACs of the regions of our interesting.

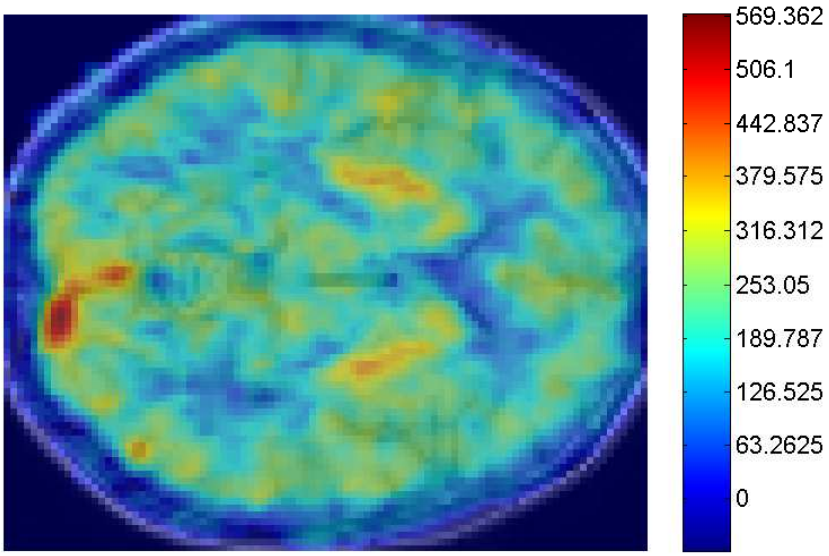

(a) High tracer uptake in the Striatum area and Globus Pallidus

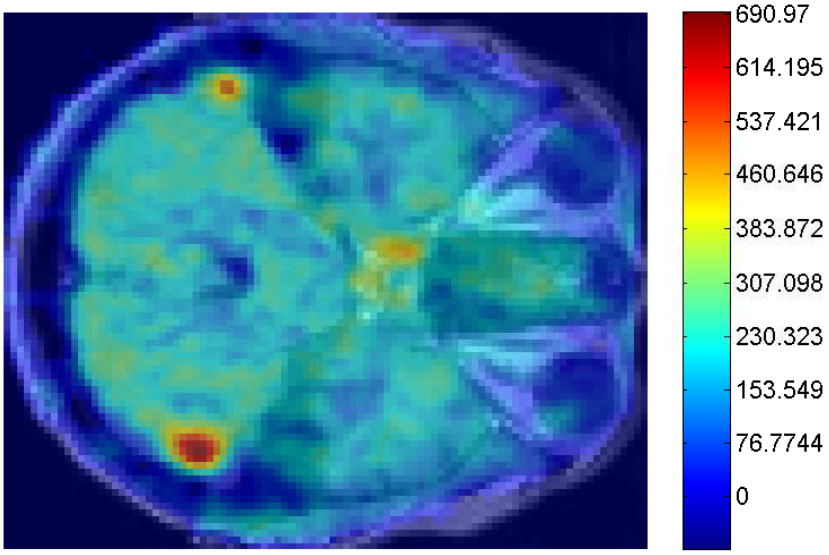

(b) Particular of Cerebellum area, where the uptake is very low

Figure 4.3: In these figure we represent some summed PET images coregistered to their relative MRI for subject 1711, in order to display the different tracer uptake

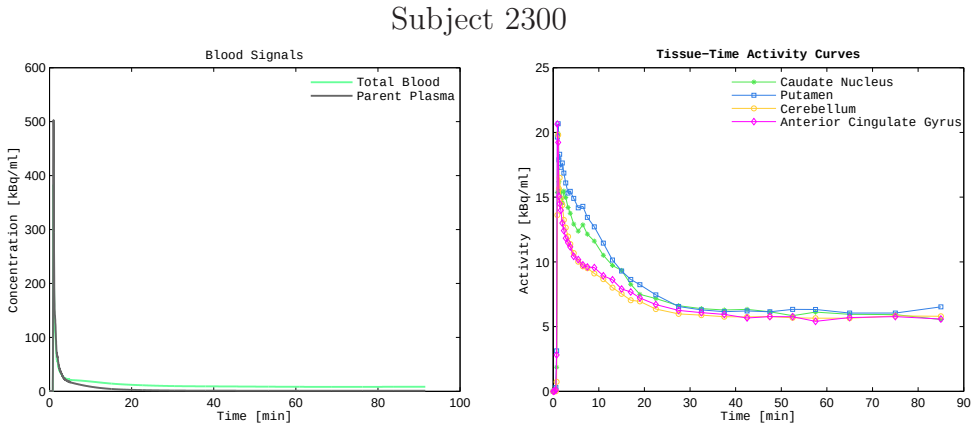

Figure 4.4: Control Subject. Left column: blood and unmetabolized plasma activity curves. Right column: tissue-time activity curves for 4 regions of interest, after averaging the left and right part.

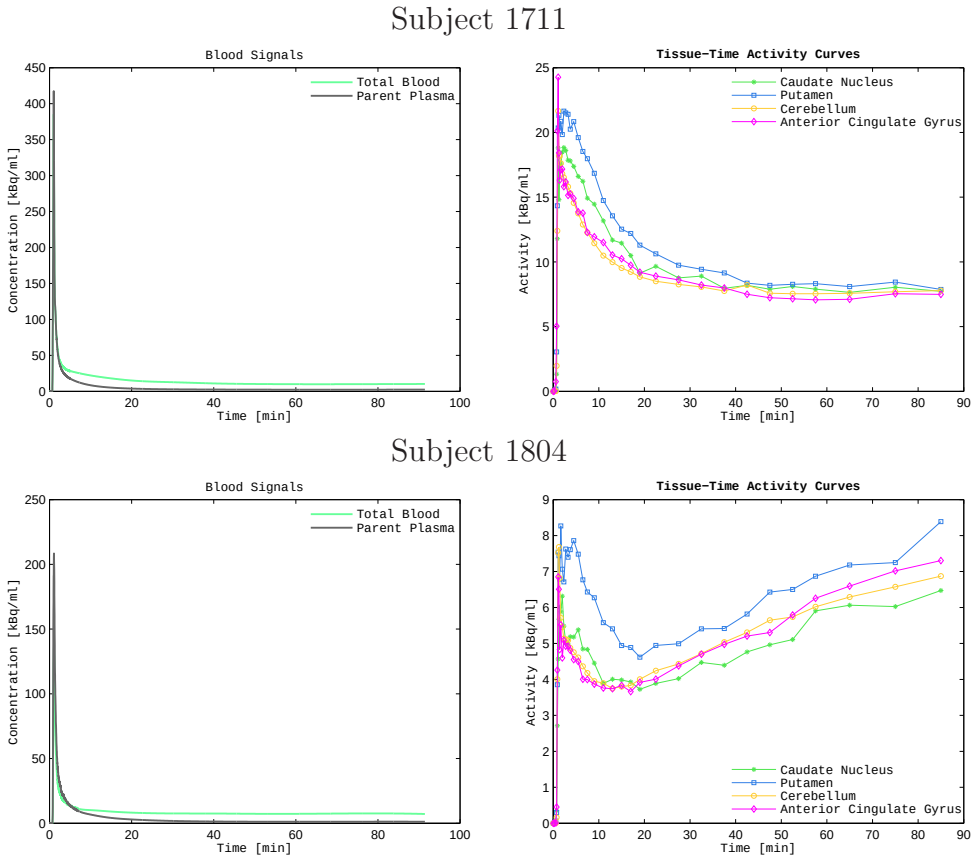

Figure 4.5: Subjects with Parkinson's disease. Left column: blood and unmetabolized plasma activity curves. Right column: tissue-time activity curves for 4 regions of interest, after averaging the left and right part.

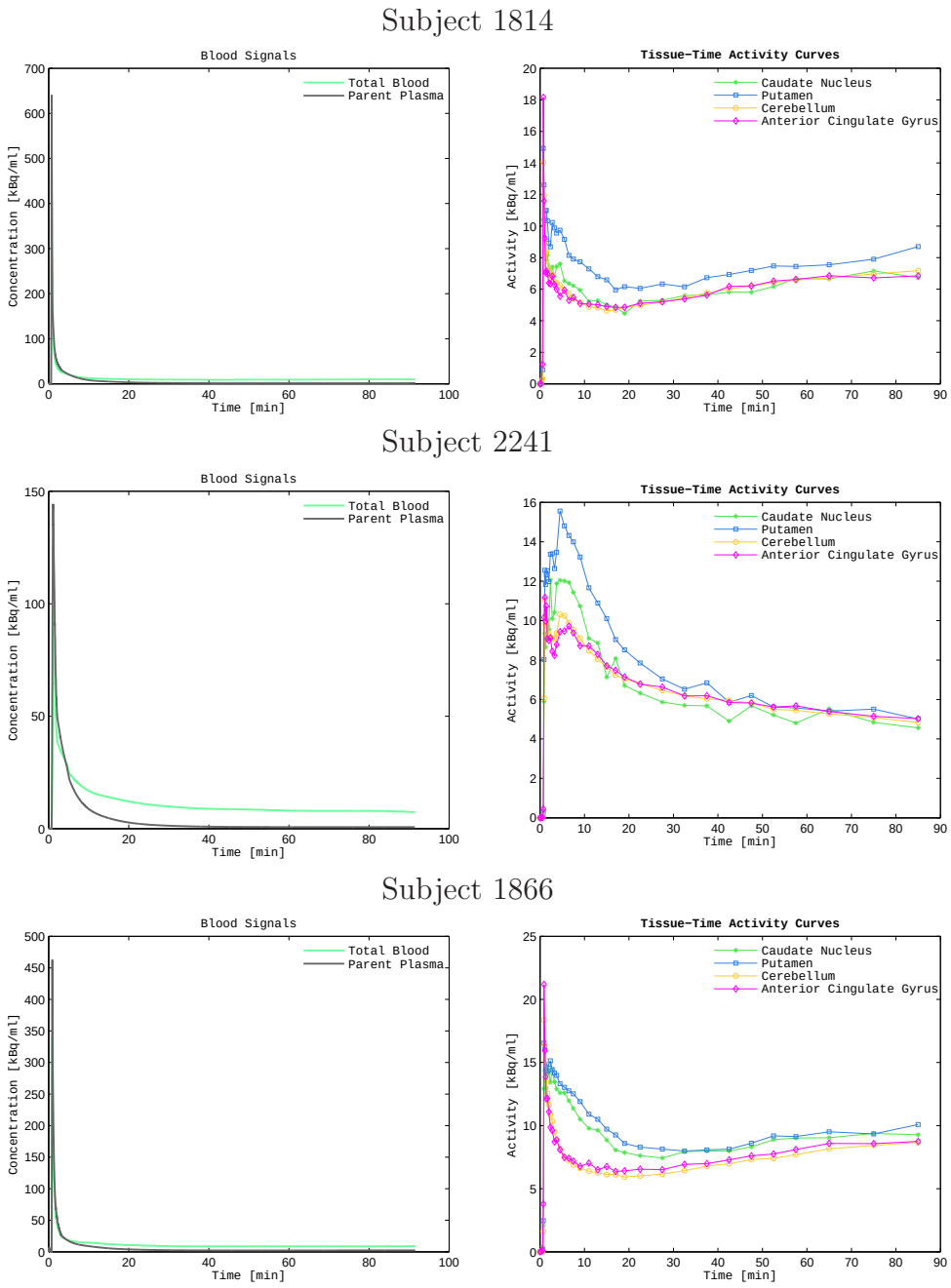

Figure 4.6: Subjects with Parkinson's disease and Dyskinesia. Left column: blood and unmetabolized plasma activity curves. Right column: tissue-time activity curves for 4 regions of interest, after averaging the left and right part.

Chapter 5

Models and Methods

This chapter is dedicated to all ROI models used to analyze [^{11}C]SCH442416: models are divided into input/output models (Spectral Analysis), which principles and potentialities are described in the first part and models with arterial input function (Compartmental Models).

5.1 I/O Models: Spectral Analysis

5.1.1 Definition of Spectral Analysis

The most widely used I/O model in PET studies is the so called *Spectral Analysis (SA)*, a technique that was introduced by Cunningham and Jones in 1993 in order to determinate local metabolic rate of glucose in the brain, but now is commonly used with various PET tracers to study physiological systems other than brain e.g. liver, heart, kidneys, etc ... [15]. It is a method for analysis of dynamic PET data that allows identification of kinetic components of the tissue tracer activity without prior assumptions, e.g about tissue equilibration, product loss and the presence or absence of homogeneity in the tissues.

SA is based on the fact that if a system is linear, the impulse response can be written as

$$h(t) = \sum_{j=1}^{M} \alpha_j \cdot e^{-\beta_j t} \tag{5.1}$$

and the radioactivity in the tissue at time t, $C_{tiss}(t)$, is modelled as a convolution

of the plasma concentration $C_p(t)$ with a sum of M exponential terms:

$$C_{tiss}(t) = C_p(t) \otimes h(t) = \sum_{j=1}^{M} C_p(t) \otimes \alpha_j \cdot e^{-\beta_j t} \tag{5.2}$$

This can be rewritten as:

$$C_{tiss}(t) = \sum_{j=1}^{M} \alpha_j \cdot \int_0^t C_p(\tau) e^{-\beta_j (t-\tau)} d\tau \tag{5.3}$$

where α_j and β_j parameters are assumed to be positive or zero. This constrain derives from an assumption of first order tracer kinetics. The upper limit M represents the maximum number of terms to be included in the model and this is set to a large number, usually 100. The values of β_j are predetermined and fixed in order to cover an appropriate spectral range, so that the model is linear in α_j. For in vivo studies involving short lived positron emitting isotopes this range needs to extend to the slowest possible event of the tracer in the tissue up to a value appropriate to transient phenomena (e.g. the passage of activity through the tissue vasculature).

In general the corresponding term for $\beta_j \to \infty$ (i.e. β_j with a very large value) is proportional to $C_p(t)$ and can be seen as a "high-frequency component". In the same way the corresponding term with a $\beta_j \to 0$ is proportional to $\int C_p$ and can be considered as a "low-frequency" component, i.e accounting for irreversible trapping of the tracer. Finally, the components corresponding to the intermediate values β_j, "intermediate frequency", reflect the extravascular activity of the tracer [16]. This late number is very important because it gives an idea of tissue heterogeneity. Moreover, if the analysis is performed at ROI level, as in our work, the contribute of the vascular component can not be disregarded (as at pixel level) and so there is the introduction in the previous formula of a term, V_b (that has to be estimated together with alfa values) accounting for blood volume and which is proportional to the blood activity curve $C_b(t)$.

Starting from these features, is very common to define SA model equation explicitly showing the trapping in the following way:

$$C_{tiss}(t) = \alpha_0 \cdot \int_0^t C_p(\tau) d\tau + \sum_{j=2}^{M} \alpha_j \cdot \int_0^t C_p(\tau) e^{-\beta_j (t-\tau)} d\tau + V_b C_b(t) \tag{5.4}$$

with $\beta_1 = 0$.

The first step to implement the SA model is to define a grid of β_j values: different distributions can be used but, since in our work this procedure has required different tests, we will describe in detail the choice of these exponents in the next section.
Fixed the M beta values, the M+1 unknown values of the kinetic components (α_js and V_b) are estimated via non-negative linear weighted least squares algorithms. In our work this operation has been done using the *lsqnonneg* function included in Matlab, which requires the definition of

vector W, size *N*x*1* with N number of time points, it contains the chosen weights (in our case they are the inverse of variance);

matrix C, size *N*x*(M+1)*, which has in the first M columns the value of the convolution of the input function with the exponential term, while in the last one it has the total blood concentration. All these values are multiplied for the square root of weights;

vector d, size *N*x*1*, which contains the weighted values of tissue activity, measured at N time points;

vector x, size *(M+1)*x*1*, with the unknown elements α_j and V_b.

This function minimizes the weighted sum of squares of the residuals and returns an optimal vector of parameters which are ≥ 0. The result of the estimation is called "spectrum": it is important to note that, even if there is a large number of coefficients to be estimated, at most N of them can be nonzero, so there are few positive peaks in the spectrum.
The interpretation of the spectrum and its components are discussed in Section 5.1.3.

5.1.2 Selection of the Set of Exponents: Beta Grid

The selection of the best set of exponents β_j as input in spectral analysis consists of choosing an upper and a lower bound for the values of β_j, as well as a distribution of these coefficients within the chosen interval. Several distributions are

used, including linear, quadratic, logarithmic ones, but usually the traditional SA grid follows the DiStefano distribution, which was used for the first time in SA with [^{18}F]FDG PET data [16].

This is the *first beta grid* that we tested for our SA approach. The lower limit of this distribution is defined as $\beta_1 = (1/3T_{end})$ where T_{end} represents the length of the experiment (in our case 90 mins). The upper limit is given by $\beta_M = (3/T_{in})$ where T_{in} is the value of the first scan (in our case 30 sec). Within this interval, the values are distributed in the following way:

$$\beta_j = \frac{1}{\tau_j} \tag{5.5}$$

where

$$\tau_j = \tau_{j-1} \cdot \left(\frac{T_{end}}{T_{in}}\right)^{\frac{1}{M-1}} \tag{5.6}$$

with j = 2,3,..., M-1.

We chose M = 100 and added at the beginning of the grid $\beta_0 = 0$.

For the *second beta grid* we followed a linear distribution of the exponents: using PET data relative to subject 1814, we started with a fixed grid from 0 to 1.6 min^{-1} linearly divided into a large number of values, M = 3200. After applying SA with this grid to all ROIs of the examined subjects, the representation of all beta values connected to positive alfa coefficients showed two peaks corresponding respectively to the first and the last values of the fixed grid, instead, within the interval, a normal distribution could be observed.

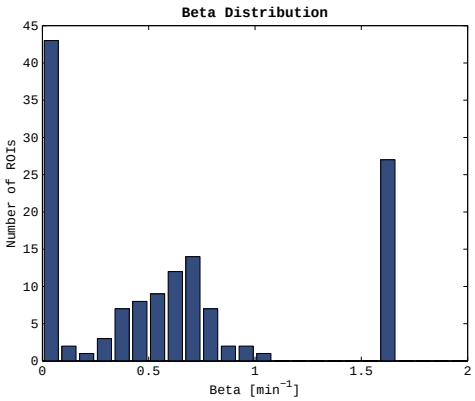

Figure 5.1: Distribution of β values for all the ROIs of subject 1814

So we described this Gaussian function with its mean and standard deviation and using these information we created a new grid linearly equispaced in 100 values from mean-3std to mean+3std, adding then at the beginning and at the end the values of 0 and 1.6 (which is a sufficient high value). We used this last grid for all the 6 subjects even if it was set starting from the data of the first subject.

Lastly, a *third beta grid* was tested, starting from the analysis of the results obtained with the previous grid approach we decided to thicken the linear grid in its first part, in order to better characterize the subjects with slow kinetics.
So this last grid ranges from 0 to 0.00945 with spacing of 0.00005, from 0.0095 to 1.1778 with spacing of 0.0118 and in the last position there is as previous the value 1.6.
In Table 5.1 we report the main characteristics of each examined beta grid, in particular we report the SA approaches implemented with each specific grid. In fact, before choosing the best one, we tested each grid on different SA techiques.
In Figure 5.2 we show the different distribution of betas with the three fixed grid; we have to underline that the formula suggested by DiStefano was modified in the value of the exponent, in order to obtain an increasing distribution with $\beta_1 < \beta_2 < \cdots < \beta_M$.

Grid	First value	Last value	Step	Number M of components	Methods
First Beta Grid	0	6	Variable (Equations 5.5-6)	101	Traditional SA
Second Beta Grid	0	1.6	0.0118	102	Traditional SA SAIF
Third Beta Grid	0	1.6	from 0 to 0.00945:0.00005 from 0.0095 to 1.6: 0.0118	291	Traditional SA SAIF SA with double input

Table 5.1: For each grid, we report the minimum and maximum value, the step between two adjacent components and the methods tested with the grid under consideration. At the end, we choose to use for all the different approaches the third beta grid

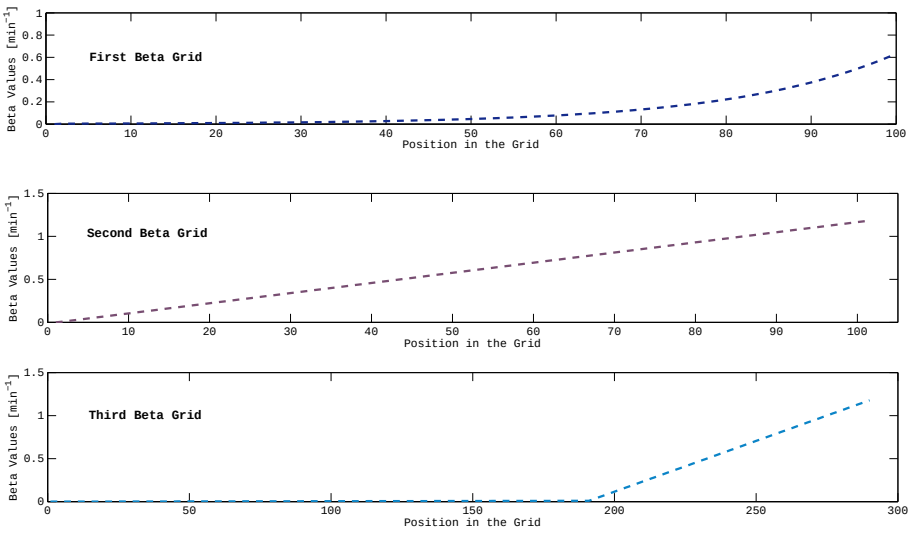

Figure 5.2: Comparison between different grid distributions

5.1.3 The Features of Spectral Analysis

The estimation of α_j and β_j from data provides useful insight into the system behavior and their interpretation can led to the definition of the best compartmental model: spectral analysis and compartmental model approach are strong correlated each other.

As we said before, a distinction is made between low, intermediate and high β_j components (frequency components). The amplitude α_j corresponding to the highest β_j value ($\beta_j \to \infty$) gives a measure of the vasculature within the ROI; the estimated α value in the last position (M+1) represents the blood volume term V_b. The amplitude α_j corresponding to the lowest β_j value ($\beta_j = 0$ or $\to 0$) reveals the trapping of the tracer and suggests the presence of an irreversible compartment in the related model. Finally, the number of nonzero α_j corrisponding to the intermediate β_j values is connected to the number of identificable reversible compartments within the ROI exchanging with plasma. So in SA each component refers at least to one compartment; the problem is that the spectrum can not say how the compartments are linked each other, for example discrimination of two reversible tissue compartments does not estabilish if they are parallel (heterogeneous tissues) or catenary (homogenous tissues). Therefore it is impossible to determine an unequivocal correspondence between the spectrum and model, this tecnique can only suggest a set of possible compartmental representations which has the same number and type of components.

Components detected with SA can also be combined in order to obtain parameters of physiological interest. For example Cunningham et al.([15],[17]) used the resulting α and β components to estimate the unidirectional clearance of tracer from blood to tissue, K_1, and the volume of distribution of the tracer in the tissue,V_d, determined as:

$$K_1 = h(t=0) = \sum_{j=0}^{M} \alpha_j \tag{5.7}$$

$$V_d = \int_0^{\infty} h(t)dt = \sum_{j=1}^{M} \frac{\alpha_j}{\beta_j} \tag{5.8}$$

Instead, if the α_0 component corrisponding to $\beta = 0$ is detected (the coefficient of the integral of the plasma concentration), it represents the uptake rate constant, K, i.e the unidirectional trapping of the tracer:

$$K = \alpha_0 \tag{5.9}$$

Sometimes results of SA are used to obtain kinetic parameters and rate constants but in this case a specific compartmental system structure is required to interprete them.

This tecnique has many positive elements, first of all the fact that it does not require to fix the number of components necessary to characterise the data, but rather it provides an estimate of the minimum number of compartments useful to describe the kinetics of the system. Furthermore the SA does not require steady state conditions for the tracer, as the graphical analysis technique and it provides a very good fit of data, this because only the data, without any prior assumptions, are used to provide the spectrum and so the final results are in perfect correlation with them. This last characteristic has on the other side a negative consequence: SA fits the data so well that it tracks also the noise and so the results can be corrupted by the presence of noise, with changes in the shape of the spectrum. In fact noise in the data usually shifts the components from their true positions and sometimes can produce non-realistic components called "phantom components", both at high and low frequencies. About the accuracy, the SA technique has lower precision in parameter estimates than the compartmental model approach, this is due to the large number of parameters of the SA model equation (100 or more) and it is also conditioned by the fixed grid. Moreover there is usually the problem of "double components", due to the discrete nature of the beta grid: the SA can not place all the components in their correct positions, but only at betas defined by the grid. As a consequence, sometimes the algorithm splits the real kinetic components in two adjacent parts and so the corresponding α values are estimated with low precision.

Lastly we can say that the SA tecnique has a good efficiency and, even if for the non-negativity constrain on α values it is possible to use only algorithms that implement this condition, it is extremely fast compared to non linear methods.

5.1.4 Other Spectral Analysis Tecniques

After applying the standard SA approach, to try to overcome the limits of this Cunningham method we used a new spectral analysis algorithm, which was recently adjusted with leucine PET data: **Spectral Analysis Iterative Filter** (SAIF) [18]. The starting point of this idea is the Turkheimer SA method, in particular the double Turkheimer filter: with this method, all the identified components with exponents greater than zero but less than $\beta_{lowcut-off}$ are assumed to have been shifted from β_0 due to noise in the data and components with exponents greater than $\beta_{highcut-off}$ are assumed to be connected to the blood volume term. The two values β_{low} and β_{high} define che cut-off interval and the goal of the method is to eliminate all the components outside this interval and thereby improving the quality of estimation for the trapping component α_0 and for the V_b. The SAIF method starting from this idea defines a correction filtering composed of two parts: in the first, it removes the equilibrating components and new values of the trapping component and Vb are estimated; in the second part the trapping and the blood volume are removed from the data and the method re-estimates the equilibrating components. These two steps are repeated until a stabilization of the WRSS is reached and its name is due to the presence of this iterative cycle. So the operative mechanism of the SAIF can be summerized in the following points:

1. traditional Cunningham SA, in order to provide the spectrum for the filtering process;

2. selection of the cut-off interval;

3. double Turkheimer filter, so that new values of the trapping and V_b are estimated (*1st filtering*);

4. new estimation of the equilibrating components, using the same principles and values of the 1st filtering (*2nd filtering*);

5. stop criterion, in particular the WRSS variation is used; in this way the a priori definition of the number of iterations is avoid and only the characteristics of data determine when the cycle must be stopped.

So this algorithm attempt to strike a balance between the equilibrating components and the limit components by delating those components which are outside the cut-off interval. It is immediatly clear that the choice of this interval is one of the most important and crucial element for the success of the algorithm, in fact it greatly influences the final spectrum, and therefore also the estimates of the different variables. Unluckly there is not yet a general method to fix the endpoints of this cut-off interval, and the best way is to test different values for β_{low} and β_{high} looking for the ones which give the lowest bias, the best distribution of parameters and precision, as well as the lowest number of iterations. After testing various combinations of these two values, we tried to find a possible method that could allow the endpoints to be fixed respecting the caracteristics of the PET data of each subject. We arrived at the formulation of one possible idea using the results of the traditional Cunningham SA and the definition of the probability density function. After fixing a specific beta grid, for each subject we applied the SA approach to all the regions of interest and represented through an istogram the state of the beta values corresponding to the equilibrating components. This showed some normal distributions (one or two peaks) and so starting from this observation, we decided to compute a probability density estimate of represented distribution, using the *ksdensity* function of Matlab. If the number of detected peaks was two or more, we chose the beta values corresponding to the highest ones and used them as endpoints for the cut-off interval, instead if only one peak was present in the probability density function we reported this beta value as β_{high} and for the β_{low} we chose one value among the first values of the fixed beta grid. This idea has to be improved and further tested, also using different PET data and fixed beta grids.

Lastly, we tested also another spectral analysis algorithm, which is a modification of the Cunningham method: it has two different input functions, one is the usually plasma concentration $C_p(t)$, instead the other is given by the total plasma concentration, i.e the plasma with the metabolites $C_{tp}(t)$. This is different from the total blood $C_b(t)$, because $C_{tp}(t)$ is corrected for the haematocrit.
We tried this double input algorithm with the purpose of inquiring into the influence of metabolites, looking if some lines of the spectrum were due to these ones

since their presence was considerable. So we have now two different convolutions even if the esponential term is the same, the estimated parameters are the blood term V_b for $\beta \to \infty$, α values connected to the plasma input funcion and η values proportional to the total plasma input. Also in this case, the values found in corrispondence to $\beta = 0$ represent the presence of an irreversible process.
The total activity in the ROI $C_{tiss}(t)$ can be written as:

$$\begin{aligned} C_{tiss}(t) =& \sum_{j=1}^{M} \alpha_j \cdot C_p(t) \otimes e^{-\beta_j t} + \sum_{j=1}^{M} \eta_j \cdot C_{tp}(t) \otimes e^{-\beta_j t} + V_b C_b(t) \\ =& \alpha_0 \cdot \int_0^t C_p(\tau) d\tau + \sum_{j=2}^{M} \alpha_j \cdot \int_0^t C_p(\tau) e^{-\beta_j (t-\tau)} d\tau + \\ & \eta_0 \cdot \int_0^t C_{tp}(\tau) d\tau + \sum_{j=2}^{M} \eta_j \cdot \int_0^t C_{tp}(\tau) e^{-\beta_j (t-\tau)} d\tau + V_b C_b(t) \end{aligned} \tag{5.10}$$

with $\beta_1 = 0$.

5.2 Compartmental Models for [^{11}C]SCH442416

Spectral Analysis, that we have seen in the first part of the chapter and used as first method for the analysis of our [^{11}C]SCH442416 data, is an important example of a noncompartmental modeling approach that has been widely applied in PET studies. Starting from results obtained with this I/O model, that suggests the minimum number of compartments to be used to describe the kinetic of the tracer, we then considered the tradional approach for the modeling PET tracer wich is based on compartmental models and tried to choose the best representation for our data. These compartmental models requires an arterial blood or plasma input function, wich is known and considered without errors, and make a series of general assumptions, e.g. that there is instantaneous mixing within the individual compartments, that the concentration of tracer is small enough so that it does not perturb the system under study, that tissue is homogeneus. Under these conditions the system is described by a set of first order linear differential equations and parameter estimates may be obtained by the weighted least squares fitting of these models to measured PET data, as we will see in the following sections.

5.2.1 Traditional Compartmental Models

Most quantitative PET studies of radioligand binding to neuroreceptors in brain are analysed using models derived from the three-tissue compartment model formulated by Mintun et al. in 1984. The three-tissue compartments account for the radioligand in terms of free ($C_f(t)$), non-specifically bound ($C_{ns}(t)$) and specifically bound ($C_s(t)$) pools, while $C_p(t)$ is the plasma concentration corrected for the presence of metabolites. Parameters K_1 [ml ml^{-1} min^{-1}] and k_2 [min^{-1}] represent rate constant of ligand transfer from plasma to tissue and viceversa, k_3 [min^{-1}] represents the transfer of tracer to the specific compartment from the free one and k_4 [min^{-1}] is the return, while k_5 [min^{-1}] is the transfer of the tracer from the free to the non specific pool and k_6 [min^{-1}] is the return (Figure 5.3) [19].

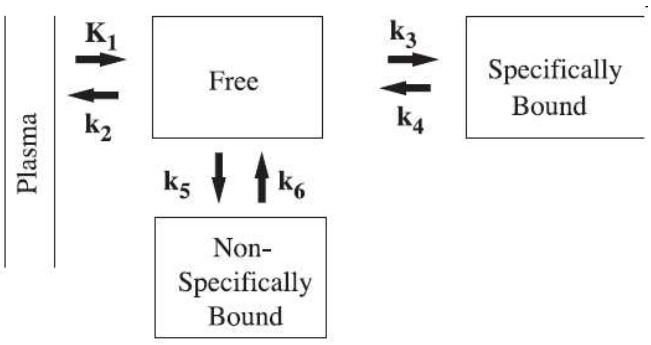

Figure 5.3: Three-tissue six-rate costant compartmental model normally used for neuroreceptors syudies

In practice, because of the noise in typical PET data, it is not possible to identify the full model within individual regions, unless additional constraints are applied or supplementary data are available and so usually it is used the lower order two-tissue compartment configuration which is based on the assumption that the free and non specific tracer kinetics are indistinguishable ($C_f(t)$ and $C_{ns}(t)$). The **two-tissue four-rate constant compartmental model** (4K model) was the first representation that we used to describe the tracer radioactivity in the brain, even if it was soon rejected since the results of the I/O model (as we will see in Chapter 6) showed the presence of an irreversible trapping of the tracer, component that was significant for almost all the 6 subjects. In this model the

exchange rates k_5 and k_6 are sufficiently rapid in comparison to the other rates of the model and so there is the simplification $C_{f+ns}(t) = C_f(t) + C_{ns}(t)$ i.e the free and non specific binding tracer concentration are considered together, as a unique pool (Figure 5.4).

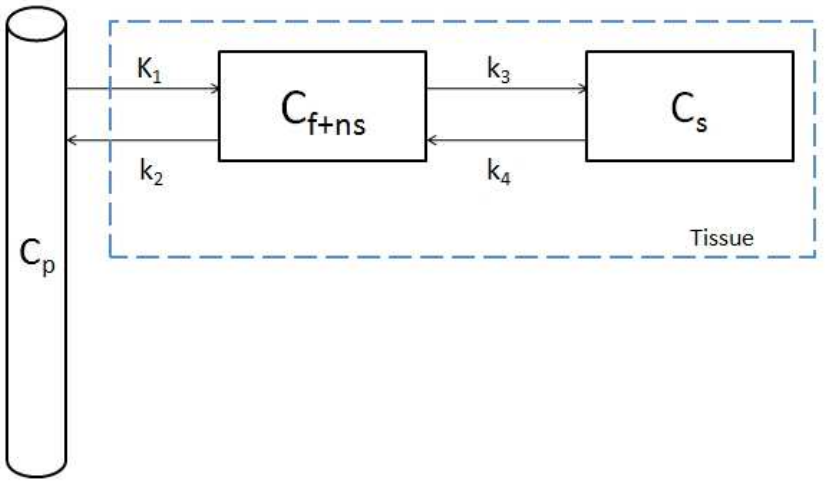

Figure 5.4: 4K model

The model equations are:

$$\begin{aligned} \frac{dC_{f+ns}(t)}{dt} &= K_1 C_p(t) + k_4 C_s(t) - (k_2 + k_3) C_{f+ns}(t) \\ \frac{dC_s(t)}{dt} &= k_3 C_{f+ns}(t) - k_4 C_s(t) \end{aligned} \tag{5.11}$$

with initial conditions $C_{f+ns}(0) = C_s(0) = 0$.
The PET scanner measure is given by

$$C(t) = (1 - V_b)[C_{f+ns}(t) + C_s(t)] + V_b C_b(t) \tag{5.12}$$

where $C(t)$ is the total activity in the ROI, $C_b(t)$ is the whole blood tracer concentration and V_b [unitless], as seen previously for the SA, is the fraction of total volume occupied by blood. All five model parameters, K_1, k_2, k_3, k_4 and V_b are a priori uniquely identifiable. The 4K model was tested to have a whole view, but we focused more our attention on other two irreversible models deriving from this one: the 3K and the 5K models.
The **two-tissue three-rate constant compartmental model** (3K model) was

first proposed by Sokoloff et al. (1977) to describe the [^{18}F]FDG kinetic in human and it main caracteristic is that it assumes the tracer is trapped in the tissue during the experiment (Figure 5.5).

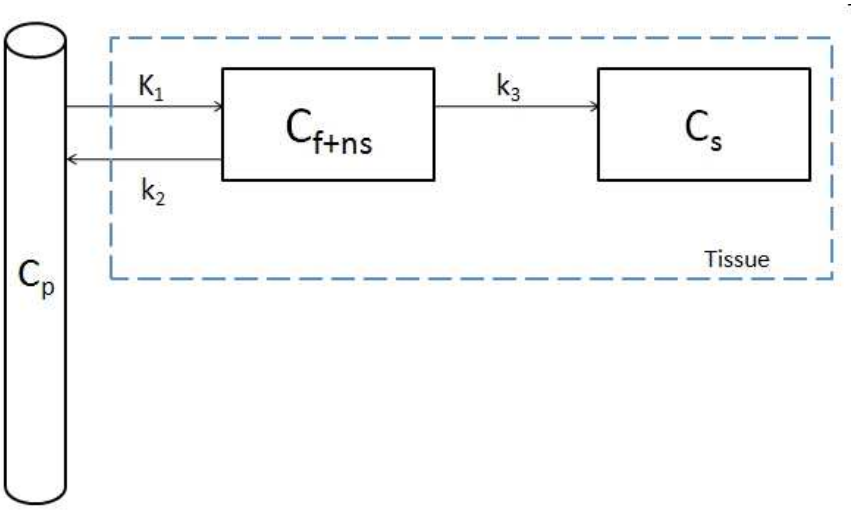

Figure 5.5: 3K compartmental model

With some renumbering the equations of the model are

$$\begin{aligned} \frac{dC_{f+ns}(t)}{dt} &= K_1 C_p(t) - (k_2 + k_3) C_{f+ns}(t) \\ \frac{dC_s(t)}{dt} &= k_3 C_{f+ns}(t) \end{aligned} \tag{5.13}$$

with initial conditions $C_{f+ns}(0) = C_s(0) = 0$, while the PET measure is the same of the Equation 5.12, given by

$$C(t) = (1 - V_b)[C_{f+ns}(t) + C_s(t)] + V_b C_b(t) \tag{5.14}$$

For this case it is interesting to see the correlation between the compartmental and the I/O model, also to better understand how it is possible to interpretate the numerical SA results and to find the different rate costants knowing the structure of the system. In this situation the spectrum given by the SA tecnique consists of three components: a trapping component (irreversible compartment), an equilibrating component (reversible compartment) and a blood term V_b, for $\beta \to \infty$, accounting for the vasculature in the ROI.
The associated SA equation is

$$C(t) = \alpha_0 \int_0^t C_p(\tau) d\tau + \alpha_1 \int_0^t C_p(\tau) \cdot e^{-\beta_1 (t-\tau)} d\tau + V_b C_b(t) \tag{5.15}$$

while the measurement equation derived from the 3K model after the solution of the differential system (Equation 5.13) is

$$C(t) = \frac{K_1 k_3}{k_2 + k_3} \int_0^t C_p(\tau) d\tau + \frac{K_1 k_2}{k_2 + k_3} \int_0^t C_p(\tau) \cdot e^{-(k_2+k_3)(t-\tau)} d\tau + V_b C_b(t) \quad (5.16)$$

So the correlation is immediatly clear and given by:

$$\begin{cases} \frac{K_1 k_3}{k_2+k_3} & = \alpha_0 \\ \frac{K_1 k_2}{k_2+k_3} & = \alpha_1 \\ k_2 + k_3 & = \beta_1 \end{cases} \quad (5.17)$$

The same procedure can be done also for the other models in order to clearly identify the relationship between the α and β values of the spectrum and the rate costants of the specific structure. The 3K model is a priori uniquely identifiable and its parameters are estimate using a weighted non-linear least squares method, as we will explain in details in Section 5.2.3.

The **three-tissue five-rate costant compartmental model** (5K model) can be viewed as an extension of the model proposed by Sokoloff: the difference with this one lies in its explicit accounting of a non-specifically bound pool. The rate costant k_5 $[min^{-1}]$ describes the exchange between this compartement and the free one, while k_6 $[min^{-1}]$ represents the return; moreover, like in the 3K model, it is supposed there is an irreversible trapping of the tracer in the specifically bound pool (Figure 5.6).

This model is described by the following equations:

$$\begin{aligned} \frac{dC_f(t)}{dt} &= K_1 C_p(t) + k_6 C_{ns}(t) - (k_2 + k_3 + k_5) C_f(t) \\ \frac{dC_{ns}(t)}{dt} &= k_5 C_f(t) - k_6 C_{ns}(t) \\ \frac{dC_s(t)}{dt} &= k_3 C_f(t) \end{aligned} \quad (5.18)$$

with initial conditions $C_f(0) = C_{ns}(0) = C_s(0) = 0$.

The measurement equation is defined as

$$C(t) = (1 - V_b)[C_f(t) + C_{ns}(t) + C_s(t)] + V_b C_b(t) \quad (5.19)$$

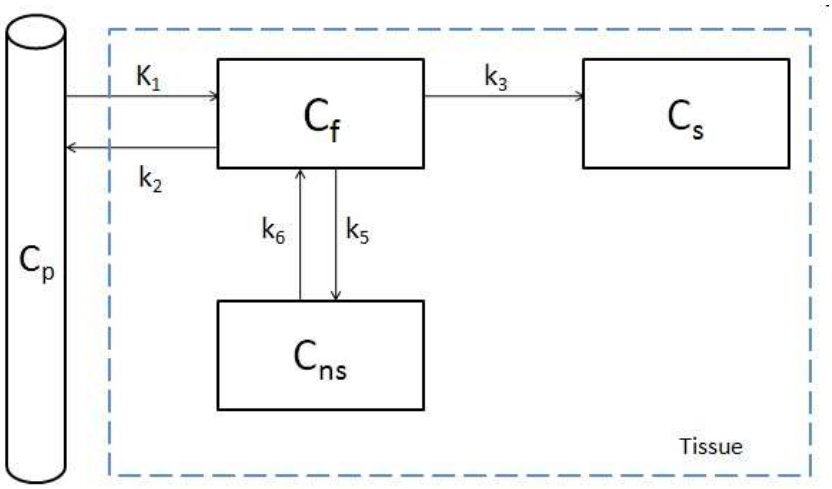

Figure 5.6: 5K compartmental model

Also this model with some adjustments is a priori uniquely identifiable: we have to underline that the parameter K_1, that we find in all these three model and represents the exchange between plasma and tissue (plasma clearance), is instead a composite parameter (a sort of macroparameter) which can be written as

$$K_1 = k_1 \cdot \frac{V_{plasma}}{V_{tissue}} \tag{5.20}$$

where k_1 is the real rate costant, V_{plasma} ans V_{tissue} are respectively the volume of plasma and tissue, which are all unknown. This is the reason why K_1 has a different unit of measure in comparison with the other rate costant parameters, i.e $ml_{plasma} \cdot ml_{tissue}^{-1} \cdot min^{-1}$. We make this combination in order to have an a priori uniquely identifiable model, since if we don't reunite we have too many parameters that can not be identified with the equation in our hand.

For each of the three tested models, after the estimation of the different microparameters, we calculated some more robust macroparameters, in fact sometimes it is more useful to employ combinations of the single parameters to represent the observed data. These macroparameters provide several information such as the behavior of target molecule and physiological function.
In particular we calculated:

- Distribution Volume $V_d[ml_{plasma}/ml_{tissue}]$: it is usually defined for reversible systems and it is described as the ratio of the tracer concentration in tissue

to that in plasma in steady state;

- Net Uptake Rate Constant (fractional uptake) $K[ml_{plasma}/ml_{tissue}/min]$: it is usually defined when there is an irreversible process and it is the amount of accumulated tracer in relation to the amount of tracer that has been available in plasma, i.e the fractional rate costant of irreversible binding of tracer to the specific receptors.

For each model, we have a different formulation of these two macroparameters. For the 4K model they are given by:

$$V_d = \left.\frac{C_{f+ns} + C_s}{C_p}\right|_{ss} = \frac{K_1}{k_2}\left(1 + \frac{k_3}{k_4}\right) \tag{5.21a}$$

$$K = \frac{K_1 k_3}{(k_2 + k_3)} \tag{5.21b}$$

For the 3K model they are given by:

$$V_d = \left.\frac{C_{f+ns}}{C_p}\right|_{ss} = \frac{K_1}{(k_2 + k_3)} \tag{5.22a}$$

$$K = \frac{K_1 k_3}{(k_2 + k_3)} \tag{5.22b}$$

Lastly, for the 5K model:

$$V_d = \left.\frac{C_f + C_{ns}}{C_p}\right|_{ss} = \frac{K_1}{(k_2 + k_3)}\left(1 + \frac{k_5}{k_6}\right) \tag{5.23a}$$

$$K = \frac{K_1 k_3}{(k_2 + k_3)} \tag{5.23b}$$

These two macroparameters, together with the plasma clearance K_1, are the same that we can evaluate also with the SA approach, as we have seen before.

5.2.2 New Compartmental Models

After a more detailed observation of the summed PET images (from 0 to 90 mins, but also other intervals were tested), in all subjects we found a significant amount of blood especially in the occipital lobe area: as we will explain and discuss in the next chapter, we performed a quantitative analysis of this area, and starting from these results we proposed some new and particular compartmental models to describe the kinetic behavior of [^{11}C]SCH442416.
We are undergoing to present four different models, they all account for the high presence of blood, in which there are many A_{2A} receptors that are the target subtype of our tracer and that are both connected to the blood vessels and human platelets.

The **first model** that we propose (*Model 1*) is a four-compartment five-rate costant model, in particular one compartment accounts for plasma tracer concentration ($C_p(t)$), one is for the tissue concentration ($C_3(t)$), the other two compartments are also connected to blood and not to tissue as previously ($C_1(t)$ and $C_2(t)$) and this is the innovation in comparison with the tradional compartmental models used for neuroreceptor binding studies (Figure 5.7). Moreover, in accordance with the main result of SA tecnique, we suppose the presence of an irreversible process of the tracer, but the trapping is in the vascular part (so it represents a non-specific binding): it is described by the rate costant $k_3[min^{-1}]$. The other rate costants k_1 $[min^{-1}]$ and k_2 $[min^{-1}]$ describe the exchanges inside the blood vessels, while K_5 $[ml_{plasma} \cdot ml^{-1}_{tissue} \cdot min^{-1}]$ and k_6 $[min^{-1}]$ represent the exchange through the blood-brain barrier BBB from plasma to tissue.

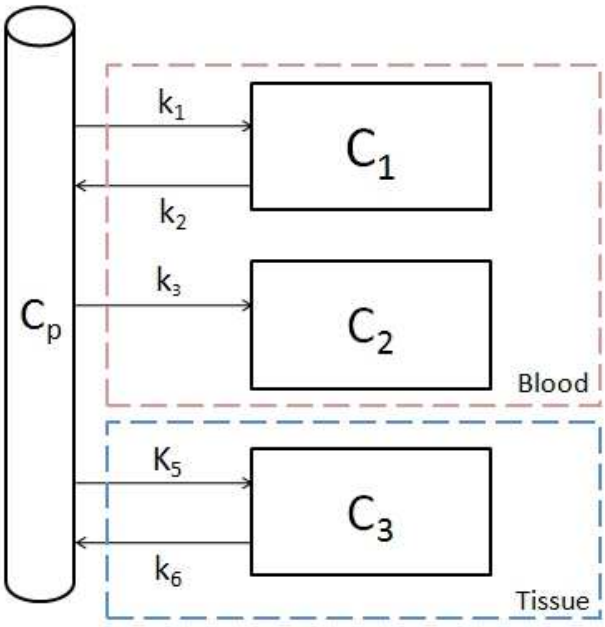

Figure 5.7: Model 1

The equations that describe the model are:

$$\begin{aligned} \frac{dC_1(t)}{dt} &= k_1 C_p(t) - k_2 C_1(t) \\ \frac{dC_2(t)}{dt} &= k_3 C_p(t) \\ \frac{dC_3(t)}{dt} &= K_5 C_p(t) - k_6 C_3(t) \end{aligned} \tag{5.24}$$

with initial conditions $C_1(0) = C_2(0) = C_3(0) = 0$.
The new PET scanner measure is given by

$$C(t) = (1 - V_b)C_3(t) + V_b[C_1(t) + C_2(t)] + V_b C_b(t) \tag{5.25}$$

This structure is a homogenous kinetic model and so there is not the problem of identifiability, in fact it is a priori uniquely identifiable (for all details see Appendix A). The parameters of interest that we are looking for in this case are defined as

$$\text{Fractional Uptake} = K = k_3 \tag{5.26a}$$

$$\text{Distribution Volume} = V_d = \frac{K_5}{k_6} \tag{5.26b}$$

while the unidirectional clearance of tracer from blood to tissue is now given by the macroparameter K_5.

Starting from this configuration, we tried a **second model** (*Model 2*) with the same number of costant rates and compartments but connected each other in a different way: the tissue is described by a two-tissue four-rate costant structure, while the irreversible trapping is still due to blood presence and it is in the vascular part (Figure 5.8). The rate costants K_1 $[ml_{plasma} \cdot ml_{tissue}^{-1} \cdot min^{-1}]$ and k_2 $[min^{-1}]$ describe the transport through the BBB from plasma to the free-nonspecifically bound pool ($C_1(t) = C_{f+ns}(t)$) and back, k_3 $[min^{-1}]$ and k_4 $[min^{-1}]$ describe the exchange between this late pool and the specifically bound compartment and return ($C_2(t) = C_s(t)$), lastly k_5 $[min^{-1}]$ describes the irreversible process inside blood ($C_3(t)$).

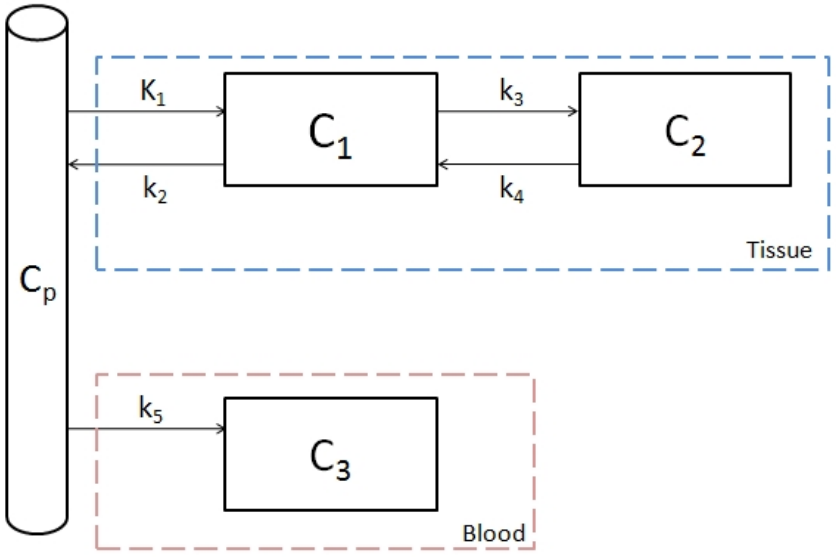

Figure 5.8: Model 2

The model is described by the following system of equations:

$$\begin{aligned} \frac{dC_1(t)}{dt} &= K_1 C_p(t) + k_4 C_2(t) - (k_2 + k_3) C_1(t) \\ \frac{dC_2(t)}{dt} &= k_3 C_1(t) - k_4 C_2(t) \\ \frac{dC_3(t)}{dt} &= k_5 C_p(t) \end{aligned} \tag{5.27}$$

The initial conditions are the same $C_1(0) = C_2(0) = C_3(0) = 0$, while the mea-

surament equation is given by

$$C_(t) = (1 - V_b)[C_1(t) + C_2(t)] + V_b C_3(t) + V_b C_b(t) \tag{5.28}$$

Also this compartmental model is uniquely identifiable and the macroparameters that we can calculate are defined as

$$K = k_3 \tag{5.29a}$$

$$V_d = \frac{K_1}{k_2}\left(1 + \frac{k_3}{k_4}\right) \tag{5.29b}$$

and, as previously, the unidirectional clearance is given by K_1.

After the analysis of the time course of the unmetabolized fraction of plasma and the results of spectral analysis with two input functions (described in the previous section), we proposed other two compartmental configurations, that still account for the significant presence of blood.

So the **third new model** (*Model 3*) has two different plasma input functions, i.e the plasma tracer concentration, corrected for haematocrit and for the presence of metabolites ($C_p(t)$, parent plasma) and the total plasma tracer concentration, uncorrected for metabolites ($C_{tp}(t)$, total plasma). We suppose that the irreversible trapping is due total blood, so connected to the presence of metabolites, and described by the rate costant k_3, while a tissue and a blood compartment exchanges with parent plasma input: K_5 and k_6 describe the transport from plasma to tissue and back, k_1 and k_2 represent the exchange inside blood part (Figure 5.9).

K_5, with measurement unit$[ml_{plasma} \cdot ml^{-1}_{tissue} \cdot min^{-1}]$, represents the plasma clearance of tracer from blood to tissue, while the other rate costants are expressed as $[min^{-1}]$.

The equations that describe the new model are:

$$\begin{aligned} \frac{dC_1(t)}{dt} &= k_1 C_p(t) - k_2 C_1(t) \\ \frac{dC_2(t)}{dt} &= k_3 C_{tp}(t) \\ \frac{dC_3(t)}{dt} &= K_5 C_p(t) - k_6 C_3(t) \end{aligned} \tag{5.30}$$

with initial conditions $C_1(0) = C_2(0) = C_3(0) = 0$ and PET misure given by

$$C_(t) = (1 - V_b)C_3(t) + V_b[C_1(t) + C_2(t)] + V_b C_b(t) \tag{5.31}$$

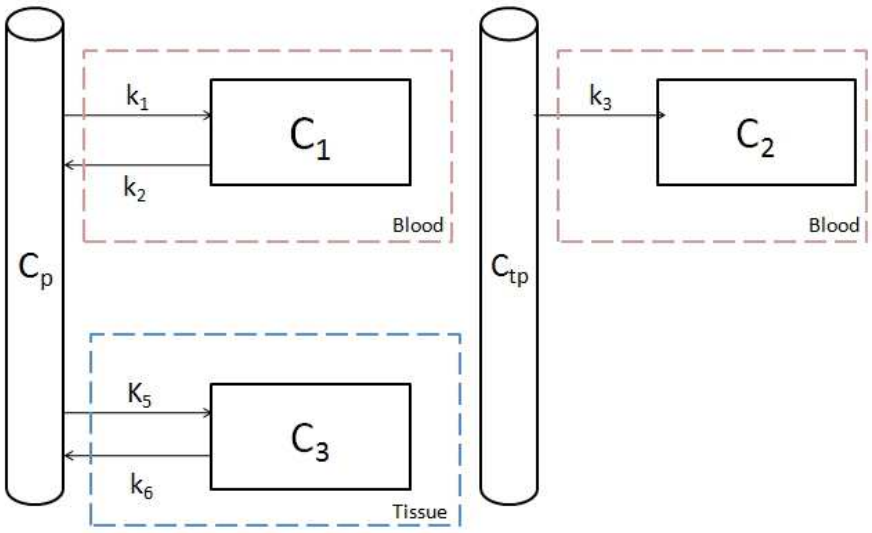

Figure 5.9: Model 3

The two combined parameters of interest are the same of Equation 5.26, in fact they are defined as:

$$K = k_3 \tag{5.32a}$$

$$V_d = \frac{K_5}{k_6} \tag{5.32b}$$

Finally, we propose a **fourth model** (*Model 4*) which as the same input functions, the same type of comparments and rate costants of Model 3, but now the irreversible process is connected to plasma concentration and not to metabolites (Figure 5.10). This comparmental model is described by

$$\begin{aligned} \frac{dC_1(t)}{dt} &= k_3 C_p(t) \\ \frac{dC_2(t)}{dt} &= k_1 C_{tp}(t) - k_2 C_2(t) \\ \frac{dC_3(t)}{dt} &= K_5 C_p(t) - k_6 C_3(t) \end{aligned} \tag{5.33}$$

with initial conditions $C_1(0) = C_2(0) = C_3(0) = 0$.
The PET scanner measure and the definition of macroparameters are the same of Equation 4.31 and Equation 4.32 respectively.

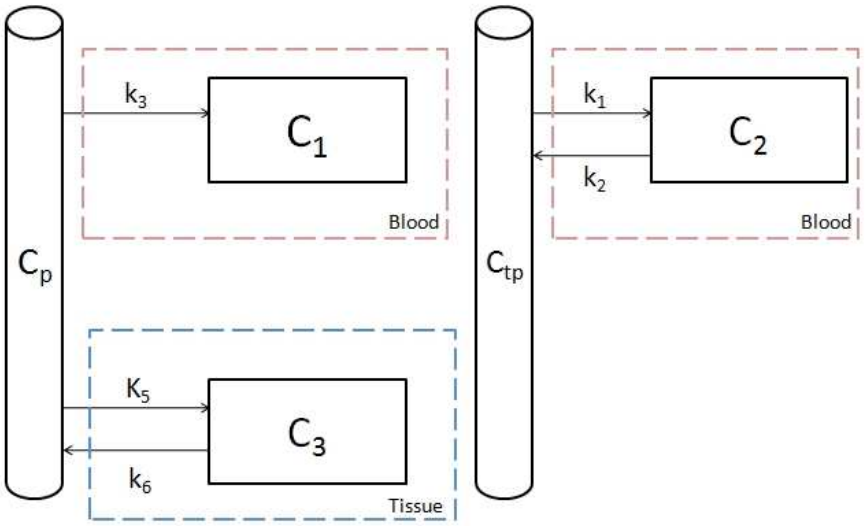

Figure 5.10: Model 4

5.3 Parameter Estimation

The kinetic components of the I/O model were estimated via nonnegative linear weigthed least squares, as described in section 5.1.1. Instead, all compartmental models require nonlinear identification and in this study all unknown parameters were estimated by weighted nonlinear least squares (WNLLS), first they were implemented in SAAM II and in a second moment in Matlab.
Tissue activity curves are described by

$$C_i^{obs}(t_j) = C_i(t_j) + e(t_j) \tag{5.34}$$

where $j = 1, 2, \cdots, N$ and N is the number of time points (number of data), t_j is the midscan time, C_i is the measured radioactivity concentration at time t_j and e is the measurement error at time t_j. Error is assumed to be additive, uncorrelated, Gaussian, zero mean and with a variance given by

$$\sigma^2(t_j) = \gamma \frac{C_i^{obs}(t_j)}{\Delta t_j} \tag{5.35}$$

where Δt_j is the length of the scanning interval relative to $C_i^{obs}(t_j)$ and γ is the unknown proportionality costant that has to be estimated a posteriori as:

$$\gamma = \frac{WRSS(\hat{p})}{N - P} \tag{5.36}$$

WRSS($\hat{p}$) is the weighted residual sum of squares evaluated in corrispondence of the vector of estimated model parameters (the dimension of this vector is P): it is given by

$$WRSS(\hat{p}) = \sum_{j=1}^{N} w_j \left[C_i^{obs}(t_j) - C_i(\hat{p}, t_j)\right] \tag{5.37}$$

where wj is the weight of the jth datum.

In our work, weigths were chosen as the inverse of the variance, i.e

$$w_j = \frac{\Delta t_j}{C_j^{obs}(t_j)} \tag{5.38}$$

and since we observed for some ROIs high weights in correspondence to the first PET data, we decided to use a threshold taking the maximum value of the last four weights: this threshold represents the maximum value that the weights can reach. So the highest weights correspond to the data at the beginning, when there is the arrival of the tracer, and in the final part of the tracer activity, in this way we weight these two part with the same accurancy.

Parameter precision was evaluated from the inverse of the Fisher information matrix M:

$$COV(\hat{p}) = \gamma M^{-1} \tag{5.39}$$

both for the α values of the I/O model and the single microparameter of the compartmental models, using then the formula for the calculation of the coefficient of variation CV[1]. Instead for the estimate of the precision of macroparameters V_d and K, if they are expressed as a combination of multiple microparameters, we started from the variance-covariance matrix COV and used the propagation of error. We calculated also the residuals and weighted residuals at time t_j, which are defined as:

$$res(t_j) = C^{obs}(t_j) - C(\hat{p}, t_j) \tag{5.40a}$$

$$wres(t_j) = \frac{C^{obs}(t_j) - C(\hat{p}, t_j)}{\sigma(t_j)} \tag{5.40b}$$

Residuals must reflect, if the model is correct, the assumptions on the measurement error, i.e., to be a zero mean and independent process.

[1]The coefficient of variation is given by: $CV(\hat{p}) = \frac{SD(\hat{p})}{\hat{p}} \cdot 100$

Finally, we evaluated also the Akaike Information Criterion, to compare the different models and it is defined as:

$$AIC = Nln(WRSS(\hat{p})) + 2P \tag{5.41}$$

Chapter 6

Results

In this chapter we are going to present the main results that we found in our [^{11}C]SCH442416 data, using the different types of models presented in the previous chapter. In particular we will focus on the results obtained with the I/O model proposed by Cunningham and on the results found with the new four compartmental models that we proposed to describe the kinetic of this tracer in the brain.

6.1 General Considerations on [^{11}C]SCH442416 Data

As already explained in Chapter 4, all arterial signals were corrected for the delay between the tracer arrival time in the brain and the arterial sampling site, and were decay corrected to the time of injection.

While in a previous study on rats it was found that tracer preferentially distributed in plasma since its plasma-to-blood ratio was always > 1 during the experimental time, here for all the subjects we find a ratio that starts from a value > 1 but rapidly decreases for the first 30 mins of the experiment, then there is a steady state till the end of the experiment. This time course is consistent with the presence of radiolabelled metabolites in blood. In humans, differently from rats and monkeys, we can observe a rapid metabolism especially in the first part and after 30 mins the unmetabolized fraction accounts for less than 30% of total

plasma activity (see Figure 4.1, Chapter 4).
The PET data were corrected for the decay and the analysis of summed PET images shows a rapid uptake in all brain regions, even if the tracer accumulation in the brain is not so high and fairly homogeneous, except for the Striatum (Caudate Nucleus + Putamen)- Globus Pallidus areas, where the tracer highly accumulates, in agreement with the selective distribution of A_{2A} receptors within the brain. As we can see from the tissue-time activity curves quoted for each subject at the end of Chapter 4, the highest activity are found in Caudate and Putamen, while other regions like Cerebellum, Anterior Cingulate Gyrus, Thalamus and Brainstem present a rapid uptake, with a time course similar to the plasmatic curve, probably because in these regions there is a small amount of adenosine A_{2A} subtype. Peak value is reached at about $1 \div 2$ mins after the tracer injection and values of concentration are similar between different subjects, except for subject 1804 who presents lower values, especially for the peak. There is a considerable inter-subject variability, in particular after 30 min from the beginning of the scan, the curves present very different courses:

- in subjects 2300, 1711 and 2241 there is a nearly constant concentration till the end of the experiment for all the ROIs;

- in subjects 1814, 1804 and 1866 there is a more remarked irreversibly bound activity, in fact the curve start to raise again.

From a more detail analysis of summed PET images we noticed the presence of large vascular areas, even if usually blood influence is less significant in this type of images and this is the observation that, during the quantitative analysis, has helped us to formulate new comportmental models, very different from the traditional ones (Figure 6.1).
Lastly, we have to underline that two of the six subjects involved in this study presented some problems during the experiment, in particular they are subject number 2300 (healthy control), who was discovered to have a brain injury, and number 1804 (PD): so in this chapter we will present also the results concerning these subjects, but the different considerations are esentially based on the other four patients.

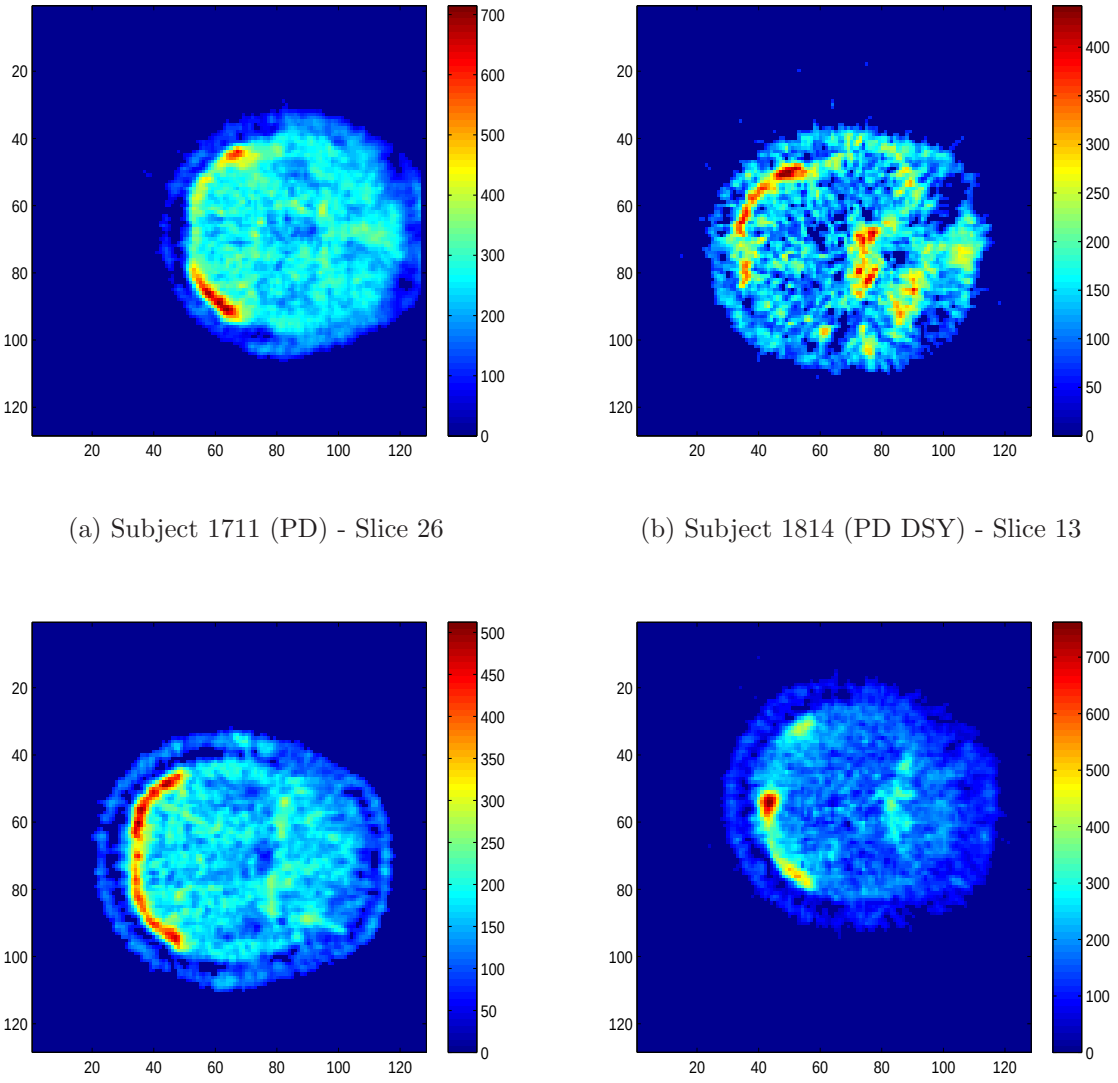

(a) Subject 1711 (PD) - Slice 26

(b) Subject 1814 (PD DSY) - Slice 13

(c) Subject 2241 (PD DSY) - Slice 24

(d) Subject 1866 (PD DSY) - Slice 25

Figure 6.1: Different slices of summed PET images (from 0 to 90 mins), which show the significant amount of vasculature in the brain connected to the [^{11}C]SCH442416 tracer, especially in the occipital gyrus

6.2 I/O model results

6.2.1 Traditional Spectral Analysis

The traditional SA approach by Cunningham was the first noncompartmental approach that we applied in order to determine the number of necessary components to describe the kinetic of the tracer into the brain. It provided us important information that guided the selection of the most appropriate compartmental structure; moreover we applied this tecnique to compare our results with ones already present in literature.

This first step to implement SA is the choice of the beta grid, as explained in Section 5.1.2 (see Table 5.1). The DiStefano distribution (first beta grid), which is usually used in SA, presented some problems with our PET data, in fact the SA approach with this grid was not able to detect the different spectral lines and the α components that it found had very low precision. The result was an underestimation of the number of spectral lines and a bad fit of the data for all subjects. To overcome these problems we used linear grids: the second beta grid identified the different α values with a good precision and good fit for all the ROIs of the six subjects, even if when it detected two adjacent lines, the coefficient of variation CV of these αs became very high.

Starting from these results, observing that subjects 1711 and 2241 had slow kinetics and for many ROIs the line connected to the first nonzero beta of the grid was identified, we decided to thicken the first part of the grid (slow components) in order to characterize better the distribution of betasand the potential presence of the trapping (third beta grid).

The model estimated curves with this grid fitted well the data and the low-frequency components were better detected, but identifing a larger number of components, the precision of some alphas decreased.

To complete the possibilities, we also tried another fix grid, starting from the distribution of βs suggested by DiStefano and changing the value of the esponent (from $\frac{1}{M-1}$ to $\frac{1}{1-M}$): in this way we did not find problems, e.g with the fit of the data, and also the precisions were similar to the ones found with the other two grids. In conclusion for all these reasons we decided to use the *third beta grid* as

optimal grid for all the subjects and for all the different SA approaches.
Each subject presents a particular behoviour, but a similar pattern can be found between some of them: for the most part of the ROIs a component in corrispondence to $\beta = 0$ was found, which indicates an irreversible trapping of the tracer, even if, especially for subject 1711 and 2241 (who present a very similar pattern in comparison with the others), this component has been shifted in the first positions of the grid, probably due to noise in the data.
The obtained spectrum is fragmented since we have a discrete grid and the presence of double components in consecutive positions is present for all the subjects, in fact frequently the algorithm splits the real value in two parts placed in the closest possible positions of the best-fitting value. Taking account of this problem of "double lines", we decided to consider as a unique component two adjacent values, both for the intermediate lines and for the ones in the first positions of the beta grid, near to $\beta = 0$ (we consider them as still irreversible trapping). Instead, the lines detected in corrispondence of the last points of grid were considered vascular noise and so connected to the blood volume component.
The number of detected lines on average and after this assumption is reported in Table 6.1.

Subject	**Number of Spectral Lines**
1814	1 component for $\beta_j = 0$ 1 intermediate component 1 component for $\beta_j \to \infty$
1711	1 component for $\beta_j = 0$ or very close 2 intermediate components* 1 component for $\beta_j \to \infty$
2241	1 component for $\beta_j = 0$ or very close 2 intermediate components* 1 component for $\beta_j \to \infty$
1804	1 component for $\beta_j = 0$ 1 intermediate component 1 component for $\beta_j \to \infty$

1866	1 component for $\beta_j = 0$ 1 intermediate component 1 component for $\beta_j \to \infty$
2300	1 component for $\beta_j = 0$ or very close 2 intermediate components 1 component for $\beta_j \to \infty$

Table 6.1: Number of spectral lines for each subject with the third beta grid.
$*$ number of lines after the assumption regarding the doubling effect (originally we found for these two subjects 4 spectral lines)

The microparameter V_b was estimated with high precision and the average value was $0.04 \div 0.05$ [*unitless*] in agreement with values present in literature, except for subject 2241 who presented a V_b two times higher. It does not belong properly to the spectrum but can be confused with high-frequency components. Remembering that the number of lines in the spectrum represents the optimal number of compartments to be included in the structure model (low-frequency component $\rightarrow$ irreversible compartment; intermediate frequency component $\rightarrow$ reversible compartment), we can lastly summerize the behaviour of each subject Table 6.2.

Subject	**Components**
1814	1 irreversible 1 reversible (0.58±0.18) blood content (V_b = 0.03±0.01)
1711	1 irreversible 1 reversible (0.03±0.02) 1 reversible (0.3±0.08) blood content (V_b = 0.04±0.01)
2241	1 irreversible 1 reversible (0.01±0.01) 1 reversible (0.19±0.04) blood content (V_b = 0.10±0.02)

1804	1 irreversible 1 reversible (0.67±0.19) blood content (V_b = 0.03 ±0.01)
1866	1 irreversible 1 reversible (0.4±0.18) blood content (V_b = 0.04 ±0.01)
2300	1 irreversible 1 reversible (0.01±0.03) 1 reversible (0.33±0.3) blood content (V_b = 0.05 ±0.01)

Table 6.2: Average components found for each subject after analysing the results in the light of the explained problems of SA approach (mean±sd)

The macroparameters of interest, i.e distribution volume V_d, unidirectional clearance of tracer from blood to tissue K_1 and the net uptake rate costant K for the trapping of the tracer, were estimated with a good precision, and so presented low CVs. However, for V_d values we found a great variability between the ROIs of subjects 1711, 2241 and 2300, due to the presence of low components near 0: probably for the estimation of this parameter it would have been better if we had trascured these values.
In the next tables we report for each subject the values found with the SA approach using the optimal grid. In particular in Tables 5.3-5.8 we show the α values without any assumptions in view of the future compartmental model, i.e they are the values given by the lsqnonneg function as optimal ones. The most important ROIs for our study are showed, considered separately in their left and right side.

Table 6.3: Subject 1814, α values without any model assumptions. $\alpha[mlml^{-1}min^{-1}]$, $\beta[min^{-1}]$,$V_b[unitless]$

ROI	α	β	α	β	α	β	α	β	$\mathbf{V}_b$
Cerebellum$_r$	0.0120	0	0.0283	0.8238	0.0113	1.6	-	-	0.0252
Cerebellum$_l$	0.0119	0	0.0160	0.7058	0.0148	0.7176	0.0050	1.6	0.0249
G cing ant$_l$	0.0121	0	0.0135	0.6822	0.0136	0.6940	-	-	0.0412
G cing ant$_r$	0.0113	0	0.0175	0.7176	-	-	-	-	0.0312
CaudateNucl$_l$	0.0122	0	0.0134	0.5169	0.0121	0.5288	0.0143	1.6	0.0172
CaudateNucl$_r$	0.0116	0	0.0119	0.4343	0.0203	0.4461	0.0000	1.6	0.0177
NuclAccumb$_l$	0.0120	0	0.0032	0.3045	0.0114	0.3163	-	-	0.0226
NuclAccumb$_r$	0.0126	0	0.0016	0.3517	0.0241	0.3635	-	-	0.0249
Putamen$_l$	0.0136	0	0.0044	0.3635	0.0350	0.3753	-	-	0.0273
Putamen$_r$	0.0141	0	0.0158	0.3635	0.0209	0.3753	0.0061	1.6	0.0261
Thalamus$_l$	0.0131	0	0.0214	0.8120	0.0197	1.6	-	-	0.0229
Thalamus$_r$	0.0123	0	0.0009	0.6468	0.0189	0.6586	0.0126	1.6	0.0232
Pallidum$_l$	0.0094	0	0.0109	0.2337	0.0039	1.6	-	-	0.0308
Pallidum$_r$	0.0100	0	0.0160	0.1275	0.0147	1.6	-	-	0.0224

Table 6.4: Subject 1711, α values without any model assumptions. $\alpha[mlml^{-1}min^{-1}]$, $\beta[min^{-1}]$,$V_b[unitless]$

ROI	α	β	α	β	α	β	α	β	α	β	α	β	$\mathbf{V}_b$
Cerebellum$_r$	0.0095	0	0.0059	0.022	0.0071	0.033	0.0283	0.305	0.033	0.316	0.0175	1.6	0.0417
Cerebellum$_l$	0.01	0	0.0018	0.0210	0.0119	0.033	0.0409	0.331	0.02599	0.3517	0.00327	1.6	0.0417
G cing ant$_l$	0.0094	0	0.0011	0.0331	0.0187	0.04491	0.0104	0.3281	0.0392	0.3399	-	-	0.0603
G cing ant$_r$	0.0101	0	0.0003	0.0449	0.0222	0.05671	0.0493	0.3753	-	-	-	-	0.0601
CaudateNucl$_l$	0.0117	0	0.0188	0.0567	0.0055	0.0685	0.0397	0.2691	0.0291	0.2809	-	-	0.0354
CaudateNucl$_r$	0	0	0.0108	0.0094	0.0097	0.0095	0.0690	0.2219	-	-	-	-	0.0289
NuclAccumb$_l$	0.0103	0	0.0202	0.0331	0.0347	0.2573	0.0284	0.2691	-	-	-	-	0.0333
NuclAccumb$_r$	0	0	0.0159	0.0095	0.0033	0.0213	0.0604	0.2101	0.0031	0.2219	-	-	0.0354
Putamen$_l$	0.0103	0	0.0101	0.0331	0.0105	0.045	0.03070	0.2219	0.0504	0.2337	-	-	0.0441
Putamen$_r$	0	0	0.01466	0.0087	0.0047	0.0088	0.0274	0.1039	0.0192	0.2691	0.0478	0.2809	0.0322
Thalamus$_l$	0	0	0.009404	0.0077	0.0108	0.00770	0.0069	0.2573	0.062323	0.2691	3.69E-05	1.6	0.0502
Thalamus$_r$	0	0	0.0132	0.00300	0.0015	0.00305	0.008	0.0331	0.007	0.2927	0.0666	0.3045	0.0479
Pallidum$_l$	0.0088	0	0.0041	0.0331	0.03	0.0449	0.0434	0.1865	0.0173	1.60000	-	-	0.0184
Pallidum$_r$	0	0	0.0065	0.0095	0.0213	0.02131	0.0399	0.1393	0.0358	1.60000	-	-	0.0199

Table 6.5: Subject 2241, α values without any model assumptions. $\alpha[mlml^{-1}min^{-1}]$, $\beta[min^{-1}]$,$V_b[unitless]$

ROI	α	β	α	β	α	β	α	β	α	β	$\mathbf{V}_b$
Cerebellum$_r$	0	0	0.0162	0.0078	0.0007	0.0078	0.0223	0.2337	0.0076	0.2455	0.0952
Cerebellum$_l$	0	0	0.0065	0.0067	0.0103	0.0068	0.0230	0.2219	0.0090	0.2337	0.0972
G cing ant$_l$	0	0	0.0104	0.0062	0.0054	0.0062	0.0006	0.1865	0.0245	0.1983	0.0859
G cing ant$_r$	0.0053	0	0.0083	0.0095	0.0036	0.0213	0.0142	0.1393	0.0028	0.1511	0.1309
CaudateNucl$_l$	0	0	0.0099	0.0048	0.0049	0.0048	0.0107	0.2101	0.0419	0.2219	0.0822
CaudateNucl$_r$	0	0	0.0122	0.0052	0.0016	0.0052	0.0181	0.2101	0.0393	0.2219	0.0574
NuclAccumb$_l$	0.0132	0	0.0112	0.0921	0.0185	0.1039	-	-	-	-	0.1218
NuclAccumb$_r$	0.0112	0	0.0014	0.1039	0.0247	0.1157	-	-	-	-	0.1023
Putamen$_l$	0	0	0.0170	0.0078	0.0013	0.0078	0.0200	0.1983	0.0503	0.2101	0.0971
Putamen$_r$	0.0095	0	0.0126	0.0449	0.0006	0.1865	0.0463	0.1983	-	-	0.1092
Thalamus$_l$	0	0	0.0008	0.0066	0.0173	0.0067	0.0345	0.3045	-	-	0.1176
Thalamus$_r$	0	0	0.0130	0.0049	0.0038	0.0050	0.0059	0.2337	0.0355	0.2455	0.0841
Pallidum$_l$	0.0125	0	0.0059	0.1275	0.0413	0.1393	-	-	-	-	0.1078
Pallidum$_r$	0	0	0.0009	0.0036	0.0139	0.0037	0.0212	0.1747	0.0301	0.1865	0.0905

Table 6.6: Subject 1866, α values without any model assumptions. $\alpha[mlml^{-1}min^{-1}]$, $\beta[min^{-1}]$,$V_b[unitless]$

ROI	α	β	α	β	α	β	α	β	α	β	$\mathbf{V}_b$
Cerebellum$_r$	0.0137	0	0.0319	0.5760	0.0131	0.5878	0.0124	1.6	-	-	0.0399
Cerebellum$_l$	0.0136	0	0.0256	0.5406	0.0146	0.5524	0.0195	1.6	-	-	0.0392
G cing ant$_r$	0.0137	0	0.0285	0.4343	0.0160	1.6000	-	-	-	-	0.0603
G cing ant$_l$	0.0146	0	0.0107	0.4933	0.0247	0.5051	-	-	-	-	0.0421
CaudateNucl$_l$	0.0159	0	0.0248	0.2219	0.0300	0.2337	-	-	-	-	0.0266
CaudateNucl$_r$	-	-	0.0061	0.0001	0.0088	0.0001	0.0458	0.2337	0.0205	1.6	0.0217
NuclAccumb$_l$	-	-	0.0012	0.0022	0.0143	0.0023	0.0318	0.2691	-	-	0.0508
NuclAccumb$_r$	0.0140	0	0.0088	0.1511	0.0001	0.1629	0.0358	1.1778	0.0368	1.6	0.0030
Putamen$_l$	0.0153	0	0.0503	0.1983	0.0008	0.2101	0.0068	1.6	-	-	0.0373
Putamen$_r$	0.0159	0	0.0307	0.1865	0.0182	0.1983	-	-	-	-	0.0376
Thalamus$_l$	0.0127	0	0.0136	0.4107	0.0272	0.4225	-	-	-	-	0.0334
Thalamus$_r$	0.0139	0	0.0150	0.4343	0.0198	0.4461	0.0112	1.6	-	-	0.0425
Pallidum$_l$	0.0118	0	0.0103	0.1039	0.0040	0.1157	0.0055	1.6	-	-	0.0129
Pallidum$_r$	0.0138	0	0.0358	0.1747	-	-	-	-	-	-	0.0209

The precision of the trapping component and of V_b is good for all the subjects, instead the alpha values have very high CVs. We also examined the fit of the data, that was good for all subjects except for subject 1804, in fact the description provided by the I/O model was not able to explain the data, expecially in the first part where the peak was not well described, even if we know from theory that the fit obtained with this type of model is the best we can reach([15],[16]). However 1804 is one of the two subjects who presented some problems during the experiment, in particular they are relative to the blood sampling, and so the data are not so beliavable.

We also examined the weighted residuals, which were obtained from the multiplication of the residuals with the data weights: if the estimation is good, the difference between the model-estimated curve and the measured data should be a representation of a white noise process[1], that means that weighted residuls should be random, zero mean and in the range [-1;1]. The results seem to be consistent with the expected trends and so this is a further verification of the good estimation obtained with the I/O model.

In Figure 6.2 we show some fits and trends of weighted residuals, for a ROI with a high number of receptors and for one of the poorest region.

[1]White noise is a random signal (or process) with a flat power spectral density.

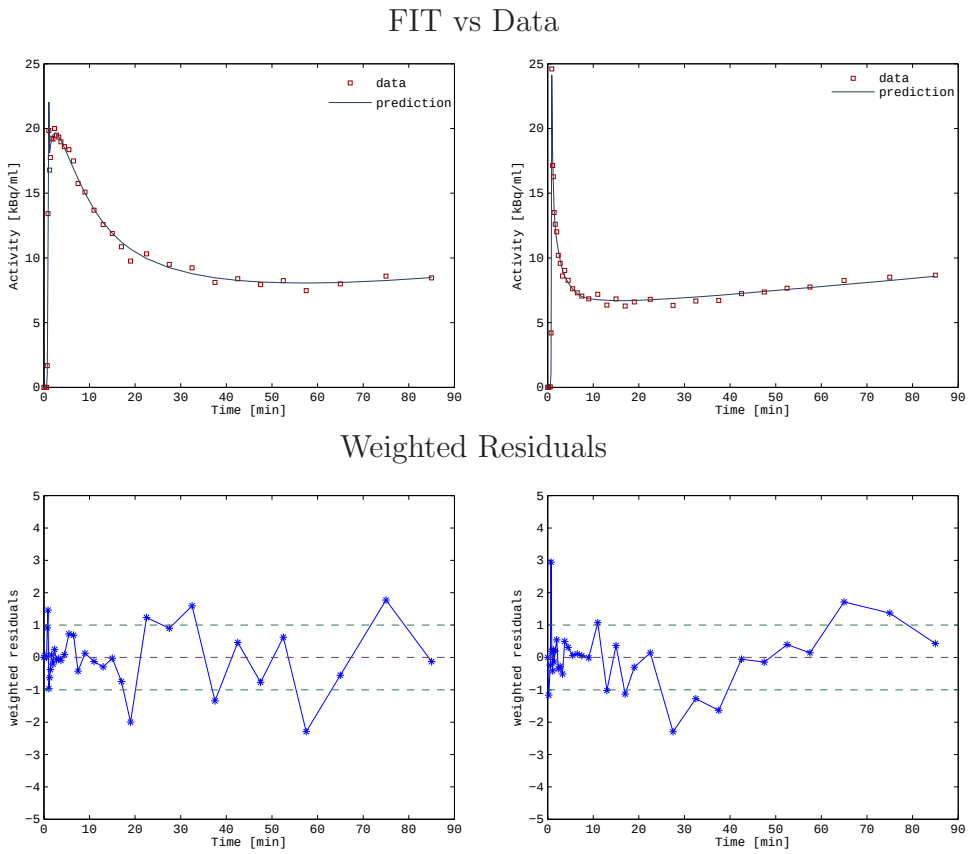

Figure 6.2: Model estimated curves with SA and weighted residuals for left Caudate Nucleus and Anterior Cingulate Gyrus, for subjects 1711 and 1866, respectively

6.2.2 Alternative SA Algorithms

The second approach that we used for the quantification of the kinetic components and variables of interest was the Spectral Analysis Iterative Filter (SAIF): since we had for some subjects a high number of spectral lines in the intermediate part and the trapping was sometimes not well identified, we decided to try this algorithm with the purpose of estimating with a better precision the different lines, also in the light of a possible compartmental model, and providing a good quality estimates of the variables.

We used the same beta grid (third grid) already used for the traditional SA and we tested different values for both bounds of the cut-off interval: the choice of these values is crucial for the application, because through this interval we decide which are the lines of interest, containing the important information, and which are due to noise. Moreover the cut-off interval influences the estimation of the limit components, i.e the trapping and V_b. We tried to use for each subjects the values altready present in literature, $\beta_{low} = 0.03$ $\beta_{high} = 0.3$, but it was immediatly clear that we could not apply to all subjects the same filter, since as seen in the previous section, they had different pattern and kinetics and with this choice, especially for subject 1814 and 1866, many components remained out of this interval. So after trying different combinations for the cut-off values in order to decide the best solution, we decided to use a more data-driven method, specific for each subject, which we already explained in Section 5.1.3. It is connected to the results of Cunningham SA and the estimation of a probability density function through *ksdensity.m* of Matlab.

We tested this method only for three of the four reliable subjects (1814,1711 and 2241): we show in Figure 6.3 the results that we obtained for the cut-off values, also in terms of spectral lines detected inside this interval. With this alternative SA approach, we are able to overcome the problems of the traditional one, like the double components, the fragmented spectrum and the shift of the low and high-frequency components due to noise.

Subject	β_{low}	β_{high}	number of spectral lines
1814	0.02	0.628	1
1711	0.0332	0.2744	2
2241	0.0193	0.1965	2

Figure 6.3: Possible values for the endpoints of the passaband filter using the SAIF; the number of lines is refeared to those detected inside the interval. $\beta[min^{-1}]$

In fact for each of these subjects we estimated with low bias and good precision the irreversible trapping, the V_b term and $1 \div 2$ intermediate components; the fit of data was good and the weighted residuals were in agreement with the expected trend.

However for many ROIs the maximum number of filter iteration was reached and often the intermediate lines were placed in corrispondence of the β_{high} value, index that probably the cut-off interval was not the optimal one. Further tests are required to verify the reliable of this idea in order to define a data-driven choice of the interval.

We also found that small changes in the value of the endpoints produced a high decrease of the precision of the estimates. For all these reasons the SAIF approach is a good algorithm, which provides us a good estimate of the parameters of interest and helps us to define the best compartmental structure, but requires the definition of a sturdy criterion to fix the cut-off values, since the bias and the accuracy depend on this choice. So we set apart this method since it was not applicable to our data to find a unique and interesting solution.

Lastly, after observing that the amount of metabolites in the total plasma concentration was significant and they rapidly appeared after the start of the study, we tested the traditional SA but with a double input function: in this case the unknown parameters, that we estimated through *lsqnonneg.m* of Matlab, were α_j correlated to the parent plasma concentration $C_p(t)$ and η_j proportional to the total plasma tracer activity $C_{tp}(t)$. In this way we wanted to detect if some lines of the spectrum were due to the presence of metabolites and in which part they were collocated. We found a high inter-subject variability, in particular for subjects 1711 and 2241 for the most part of the ROIs the line of trapping is connected to metabolites, while for subjects 1814 and 1866 an opposite behaviour was found, i.e the component for $\beta = 0$ was due to the tradional plasma input function. Moreover a too high variability was detected also inside the same subject, probably because this tecnique is very sensitive to the presence of noise and errors into the input function signals. We can summerize the results found, focusing on the trapping and low-frequency components, in the following way, which underlines the different pattern between the four subjects:

* Subject 1814 $\rightarrow$ for 39 ROIs the line of irreversible trapping is connected to $C_p(t)$; for 37 ROIs the line due to metabolites is detected in position $\beta = 0.0095$, while 3 ROIs have also other lines more than this one; for 2 ROIs the α components are not detected;

* Subject 1711 $\rightarrow$ for 24 ROIs the line of irreversible trapping is connected to $C_{tp}(t)$, and 22 of these present also other $\eta \neq 0$; 10 ROIs don't have $\eta \neq 0$ for $\beta = 0$ but present η values in corrispondence of low βs; 5 ROIs do not present the irreversible trapping; for 9 ROIs there isn't the spectral line due to metabolites; 15 ROIs present an α value for $\beta = 0.0095$ or in the adjacent positions;

* Subject 2241 $\rightarrow$ for 7 ROIs the line of irreversible trapping is connected to $C_{tp}(t)$ and for 21 ROIs low-frequency components near $beta = 0$ due to $C_p(t)$ are found; for 15 ROIs the line for $\beta = 0$ is not found; for 14 ROIs the components due to metabolites is not present in the final spectrum; for 21 ROIs $\eta \neq 0$ are found in corrispondence of $\beta = 0.0095$ or 0.0213;

* Subject 1866 → for 28 ROIs the line of irreversible trapping is connected to $C_{tp}(t)$ and for 14 ROIs it is due to $C_p(t)$; for 14 ROIs a η value for $\beta = 0.0095$ is detected.

A part from the high variability, the model-estimated curves obtained with this I/O model are able to follow and describe the data, even if the quality seems the same of previous fit with the traditional SA and also the trends of weighted residuals are very similar. The following tables 6.7-10 show the values found for the α and η values with the double input function; they are reported without any model assumptions, i.e as given by the lsqnonneg of Matlab.

Table 6.7: Values for subject 1814 without any model assumptions. $\alpha, \eta[mlml^{-1}min^{-1}]$, $\beta[min^{-1}]$,$V_b[unitless]$

ROI	$\mathbf{C_p(t)}$								$\mathbf{C_{tp}(t)}$										V_b
	alpha	beta	alpha	beta	alpha	beta	alpha	beta	eta	beta	eta	beta	eta	beta	eta	beta	eta	beta	
$Cerebellum_r$	0.0006	0.0033	0.0017	0.3753	0.020	0.3871	0.0206	1.6	0.0076	0.0095	0	0	0	0	0	0	0	0	0.0267
$Cerebellum_l$	0.0014	0.0032	0.0114	0.3753	0.012	0.3871	0.0152	1.6	0.0071	0.0095	0	0	0	0	0	0	0	0	0.0258
G cing ant_l	0.004	0.0029	0.0033	0.4579	0.022	0.4697	0	0	0.0058	0.0095	0	0	0	0	0	0	0	0	0.0431
G cing ant_r	0.002	0.0032	0.009	0.3399	0.005	0.3517	0.0034	1.6	0.0063	0.0095	0	0	0	0	0	0	0	0	0.0326
$CaudateNucl_l$	0.0021	0.0027	0.0208	0.2927	0.024	1.6	0	0	0.0068	0.0095	0	0	0	0	0	0	0	0	0.0174
$CaudateNucl_r$	0.0023	0.0029	0.0302	0.3163	0.004	1.6	0	0	0.0063	0.0095	0	0	0	0	0	0	0	0	0.0181
$NuclAccumb_l$	0.0053	0.003	0.0165	0.2691	0	0	0	0	0.0049	0.0095	0	0	0	0	0	0	0	0	0.0223
$NuclAccumb_r$	0	0	0	0	0	0	0	0	0.0009	0.000	0.0034	0.0002	0.0178	0.1393	0.0004	0.1511	0.0125	0.6114	0.0258
$Putamen_l$	0.0009	0.0032	0.0072	0.2337	0.0277	0.2455	0.0102	1.6	0.0083	0.0095	0	0	0	0	0	0	0	0	0.0276
$Putamen_r$	0.0035	0.2337	0.029	0.2455	0.0174	1.6	0	0	0.0021	0	0.0023	0.0095	0.0058	0.0213	0	0	0	0	0.0258
$Thalamus_l$	0.0022	0.0033	0.0057	0.3871	0.0125	0.3989	0.0231	1.6	0.0074	0.0095	0	0	0	0	0	0	0	0	0.0244
$Thalamus_r$	0.0051	0.2455	0.0108	0.2573	0	0	0	0	0.007	0.0080	0.0006	0.0081	0.0188	1.6	0	0	0	0	0.0242
$Pallidum_l$	0.0164	0.1275	0	0	0	0	0	0	0.0043	0	0	0	0	0	0	0	0	0	0.0303
$Pallidum_r$	0.0026	0.0022	0.0152	0.1039	0.0025	0.1157	0.015	1.6	0.0048	0.0095	0	0	0	0	0	0	0	0	0.0225

Table 6.8: Values for subject 1711 without any model assumptions. $\alpha, \eta[mlml^{-1}min^{-1}]$, $\beta[min^{-1}]$, $V_b[unitless]$

ROI	$\mathbf{C_p(t)}$										$\mathbf{C_{tp}(t)}$								V_b
	alpha	beta	alpha	beta	alpha	beta	alpha	beta	alpha	beta	eta	beta	eta	beta	eta	beta	eta	beta	
$Cerebellum_r$	0.0068	0	0.0225	0.2691	0.0412	0.280931	0.0211	1.6	0	0	0.0002	0	0.0002	0.0331	0.0088	0.0449	0	0	0.2875
$Cerebellum_l$	0.0577	0.2691	0.0103	0.4697	0.0061	1.6	0	0	0	0	0.0019	0	0.0016	0.0331	0.0101	0.0449	0.0036	0.5051	0.2882
G cing ant_l	0.0054	0.0449	0.0253	0.2809	0.0316	0.2927	0	0	0	0	0.002	0	0.0124	0.0567	0	0	0	0	0.4208
G cing ant_r	0.0077	0.0567	0.0486	0.3163	0.0058	0.3281	0	0	0	0	0.0023	0	0.0131	0.0685	0	0	0	0	0.4202
$CaudateNucl_l$	0.0275	0.0449	0.032	0.2573	0.0404	0.2691	0	0	0	0	0.0035	0	0.0006	0.0567	0	0	0	0	0.2451
$CaudateNucl_r$	0.0185	0.0095	0.0164	0.2101	0.0533	0.2219	0	0	0	0	0.001	0.0213	0	0	0	0	0	0	0.2007
$NuclAccumb_l$	0.0304	0.2219	0.041	0.2337	0	0	0	0	0	0	0.002	0	0.0149	0.0449	0.0008	0.056	0	0	0.2326
$NuclAccumb_r$	0.0159	0.0095	0.0033	0.0213	0.0604	0.2101	0.003	0.2219	0	0	0	0	0	0	0	0	0	0	0.2458
$Putamen_l$	0.0103	0	0.0101	0.0331	0.0105	0.0449	0.0307	0.2219	0.0504	0.2337	0	0	0	0	0	0	0	0	0.3062
$Putamen_r$	0.0147	0.0088	0.0047	0.0088	0.0274	0.1039	0.0192	0.2691	0.0478	0.2809	0	0	0	0	0	0	0	0	0.2236
$Thalamus_l$	0.0195	0.0081	0.0184	0.2573	0.0508	0.2691	0.0004	1.6	0	0	0.0004	0.0095	0	0	0	0	0	0	0.3486
$Thalamus_r$	0.0003	0.0036	0.0138	0.0036	0.0754	0.2927	0	0	0	0	0.0054	0.0567	0	0	0	0	0	0	0.3333
$Pallidum_l$	0.0226	0.0331	0.0134	0.0449	0.0174	0.1747	0.0288	0.1865	0	0	0.0025	0	0.0146	1.6	0	0	0	0	0.1278
$Pallidum_r$	0.0066	0.0095	0.0213	0.0213	0.0398	0.1393	0.0358	1.6	0	0	0	0	0	0	0	0	0	0	0.1382

Table 6.9: Values for subject 2241 without any model assumptions. $\alpha, \eta[mlml^{-1}min^{-1}]$, $\beta[min^{-1}]$, $V_b[unitless]$

ROI	$\mathbf{C}_p(\mathbf{t})$								$\mathbf{C}_{tp}(\mathbf{t})$										Vb
	alpha	beta	alpha	beta	alpha	beta	alpha	beta	eta	beta	eta	beta	eta	beta	eta	beta	eta	beta	
Cerebellum$_r$	0.0157	0.0083	0.0289	0.2337	0.0011	0.2455		0	0.0008	0.0213	0	0	0	0	0	0	0	0	0.6618
Cerebellum$_l$	0.0115	0.0095	0.0083	0.2101	0.0249	0.2219		0	0.0036	0.0213	0	0	0	0	0	0	0	0	0.6757
G cing ant$_l$	0.0104	0.0062	0.0054	0.0062	0.0006	0.1865	0.0245	0.1983	0	0	0	0	0	0	0	0	0	0	0.5965
G cing ant$_r$	0.0031	0.0213	0.0205	0.1393	0	0	0	0	0.0037	0.0213	0.0058	0.0331	0	0	0	0	0	0	0.9063
CaudateNucl$_l$	0.01	0.0049	0.0053	0.00107	0.0117	0.0419	0.0117		0	0	0	0	0	0	0	0	0	0	0.5708
CaudateNucl$_r$	0.0068	0.0083	0.0582	0.2101	0.0004	0.2219		0	0.0045	0.0213	0	0	0	0	0	0	0	0	0.4021
NuclAccumb$_l$	0.0071	0.0567	0.028	0.0685	0	0	0	0	0.004	0	0	0	0	0	0	0	0	0	0.8868
NuclAccumb$_r$	0	0	0	0	0	0	0	0	0.0013	0	0.00001	0.0095	0.0017	0.0213	0.0049	0.1393	0.0247	0.1511	0.7132
Putamen$_l$	0.017	0.0078	0.0013	0.0078	0.02	0.1983	0.0504	0.2101	0	0	0	0	0	0	0	0	0	0	0.6743
Putamen$_r$	0.0059	0.0331	0.0516	0.1865	0	0	0	0	0.0013	0	0.0085	0.0449	0	0	0	0	0	0	0.7597
Thalamus$_l$	0.0122	0.0095	0.0009	0.2809	0.0349	0.2927		0	0.004	0.0213	0	0	0	0	0	0	0	0	0.8160
Thalamus$_r$	0.0166	0.0051	0.0081	0.2337	0.0333	0.2455		0	0.0002	0.0095	0	0	0	0	0	0	0	0	0.5840
Pallidum$_l$	0.0084	0.1393	0	0	0	0	0	0	0.0019	0	0.0419	0.1629	0	0	0	0	0	0	0.7667
Pallidum$_r$	0.0123	0.0058	0.0359	0.1747	0.0159	0.1865		0	0.0016	0.0095	0	0	0	0	0	0	0	0	0.6313

Table 6.10: Values for subject 1866 without any model assumptions. $\alpha, \eta[mlml^{-1}min^{-1}]$, $\beta[min^{-1}]$, $V_b[unitless]$

ROI	$C_p(t)$								$C_{tp}(t)$						V_b
	alpha	beta	alpha	beta	alpha	beta	alpha	beta	eta	beta	eta	beta	eta	beta	
$Cerebellum_r$	0.0052	0.2809	0.0222	0.2927	0.0307	1.1778	0.0016	1.6	0.0059	0.0073	0.0031	0.0073	0	0	0.043
$Cerebellum_l$	0.0263	0.2691	0.0107	0.953585	0.0207	1.6	0	0	0.0001	0.0067	0.0087	0.0067	0	0	0.042
G cing ant_l	0.0229	0.2927	0.0037	0.3045	0.0054	1.0008	0.0054	1.0126	0.0095	0.0092	0.0009	0.0092	0	0	0.0442
G cing ant_r	0.0157	0.1865	0.0023	0.8356	0.0195	0.8474	0	0	0.0027	0.0081	0.0065	0.0081	0.0067	1.0952	0.0626
$CaudateNucl_l$	0.0563	0.1983	0	0	0	0	0	0	0.0028	0.0095	0.0085	0.0095	0	0	0.0278
$CaudateNucl_r$	0.0033	0.0050	0.0269	0.2101	0.0199	0.2219	0.0221	1.6	0.0087	0.0095	0	0	0	0	0.0216
$NuclAccumb_l$	0.0099	0.0048	0.0092	0.2455	0.023	0.2573	0	0	0.0043	0.0095	0	0	0	0	0.0511
$NuclAccumb_r$	0.0101	0.0567	0.0046	0.0685	0.040	1.1778	0.0331	1.6	0.0063	0	0	0	0	0	0.0034
$Putamen_l$	0.0007	0.0046	0.0502	0.1747	0.0019	0.1865	0.0106	1.6	0.0105	0.0095	0	0	0	0	0.0372
$Putamen_r$	0.0325	0.1511	0.0177	0.1629	0	0	0	0	0.0103	0.0076	0.0001	0.0076	0.0038	1.6	0.0382
$Thalamus_l$	0.0254	0.2573	0..0075	0.2691	0.0075	1.0244	0.003	1.0362	0.0057	0.0070	0.0029	0.0070	0	0	0.0356
$Thalamus_r$	0.0305	0.2809	0.0193	1.6	0	0	0	0	0.0055	0.0082	0.0043	0.0082	0	0	0.0444
$Pallidum_l$	0.0161	0.0685	0.004	0.0803	0	0	0	0	0.0053	0	0.0039	1.6	0	0	0.0133
$Pallidum_r$	0.0397	0.1275	0	0	0	0	0	0	0.0032	0.0023	0.0041	0.0023	0	0	0.0224

6.2.3 Spectral Analysis and ROI blood

As explained in the first section of this chapter, the amount of blood in summed PET images is significant: since these areas were well localizated, we decided to draw them and to consider these ones as new ROIs, called "ROIs blood". So for each subject we have a new ROI, which contains in prevalence blood, since, drawing these regions, we tried to maximize the vascular presence.
It is an additional ROI and so, as for the others, we applied the traditional SA approach, with the purpose to identify if some spectral lines were due to the blood presence. In this case we will understand which lines contain the blood information. As expected, the time-activity curve for this kind of ROI had a course which was similar to the total blood curve $C_b(t)$, with a reduced peak value, as we can see in Figure 6.4.

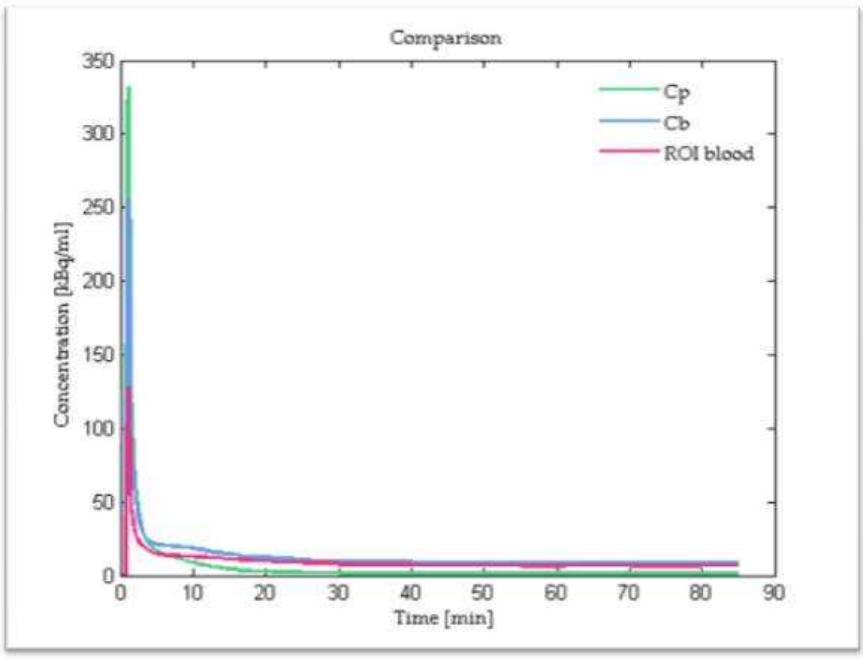

Figure 6.4: Comparison between the total blood concentration $C_b(t)$, the parent plasma concentration $C_p(t)$ and the signal extracted from ROI blood. Data are related to subject (Healthy control)

Except for subject 1711, who, as we have already seen, has a large number of spectral lines for each ROI and is enriched in information in comparison with the other ones, we found a similar pattern in all subjects and the results of this

tecnique can be summerized in the following way:

Subject	**Number of Spectral Lines**
1814	1 irreversible component for $\beta = 0$ 1 reversible component for $\beta = 0.08$ (very low amplitude) blood content $V_b = 0.22$
1711	1 irreversible component for $\beta = 0$ 1 reversible component for $\beta = 0.03$ 1 reversible component for $\beta = 0.3$ blood content $V_b = 0.5$
2241	1 irreversible component for $\beta = 0$ (very low amplitude) 1 reversible component for $\beta = 0.02$ blood content $V_b = 0.63$
1804	1 irreversible component for $\beta = 0$ 1 reversible component for $\beta = 0.1$ (low amplitude) blood content $V_b = 0.41$
1866	1 irreversible component for $\beta = 0$ 1 reversible component for $\beta = 0.17$ blood content $V_b = 0.4$
2300	1 irreversible component for $\beta = 0$ 1 reversible component for $\beta = 0.07$ blood content $V_b = 0.37$

Table 6.11: Results of SA approach for ROIs blood

From the analysis of these results, it is immediatly clear that the low-frequency components, i.e for $\beta = 0$ or very close, are connected to the presence of blood inside the different ROIs. They reflect the tracer activity in blood and not in the tissue as previously thought. So only one line describes and reflects the activity of the tracer inside the tissue. This can be clearly show in Figure 6.5.

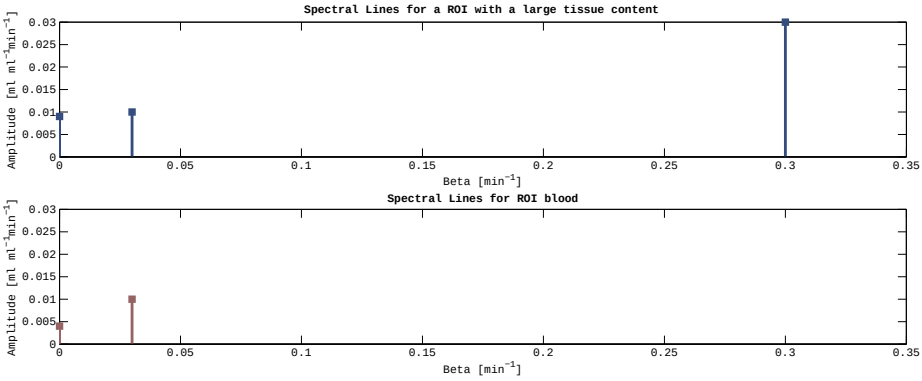

Figure 6.5: Comparison between the spectral lines found for the ROI blood (bottom) and the lines found for the left Caudate Nucleus (top), for subject 1711. The difference between the two images is given by the intermediate component, which is so the only one connected to the activity of the tracer within the tissue

Probably the intermediate component present in the ROI blood of subjects 1711 and 1866, in corrispondence of respectively $\beta = 0.3$ and $\beta = 0.17$, is due to the presence within the ROI of a part of tissue and not only blood. In Figure 6.6 we show the spectral lines relative to the ROI blood of subject 2241 together with the lines of one of the 43 ROIs (Hippocampus right), with the purpose of highlighting that only the intermediate component, in this case in position $\beta = 0.22$, reflects the behaviour of the tracer within the tissue. For blood, the low-frequency reversible component (for $\beta = 0.02$) has a higher value than the irreversible one and its α value is detected with a good precision rather than the α value for $\beta = 0$, which is very low and with a high degree of inaccuracy. This is probably the reason why this subject, as we have seen in section 6.2.1, does not present the trapping in the majority of ROIs, but present spectral lines in corrispondence of very low beta values (0.007 ± 0.001), that we have considered, in first approximation, as a shift of the irreversible component due to noise.

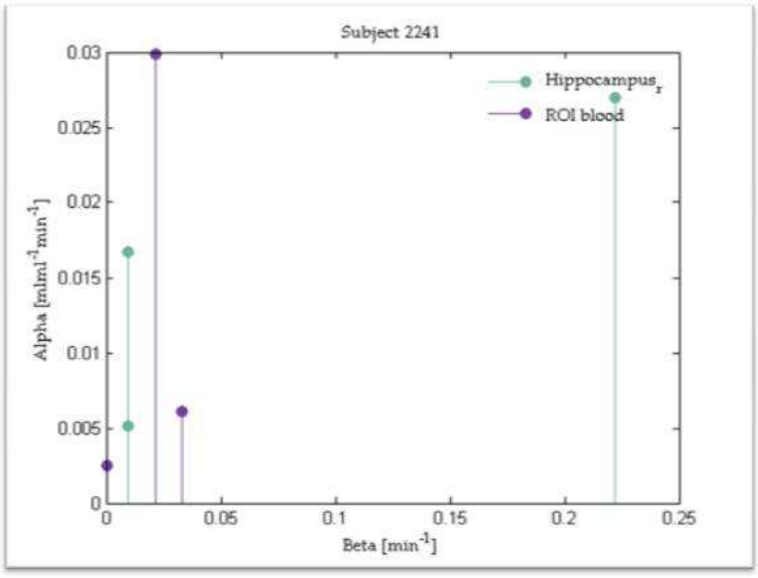

Figure 6.6: Comparison between the spectral lines of ROI blood and the ones of right Hippocampus

That being so, the results that we have found applying the SA approach to all the ROIs of each subject can be interpreted in this way: the irreversible process is due to the trapping of the tracer inside the blood vessels (where we know from physiology there is a large number of adenosine A_{2A} receptors) and also the low component, which is present for some subjects, as 1711 and 2241, are connected to blood; instead the intermediate line describes the activity of the tracer within the tissue.

These new results revealed themselves as important discoveries and they helped us to formulate the alternative compartmental models, whose numerical results will be present in the next sections.

6.3 Compartmental Models

6.3.1 Traditional Models for [^{11}C]SCH442416

We know that most quantitative PET studies of radioligand binding to neuroreceptor sites are analysed using models derived from the three-tissue six-rate costant compartment model, but because of factors such as the signal to noise ratio, condensed models with a reduced number of compartments are often used. So first of all we applied to our data the 4K model, which was able to describe the kinetics of subject 2241, who did not present totally the irreversible uptake of the tracer, instead for the others the rate costant k_4 was too small to be identified, in accordance with the SA approaches that have found a remarked trapping.
Starting from the results of the tradional SA and SAIF, to describe the irreversible binding present in the majority of subjects we applied the 3K model which revealed to be good for the patients with a low number of spectral lines, but on the contrary it was too poor to be used for the ones with a high informative content, i.e 1711, 2241 and 2300. In these cases, each parameter was estimated with accuracy, but the model estimated curve was not able to describe the data, especially in the first part after the tracer injection, where the peak and the following decrease were completely understimated. To overcome this problem, we tried to apply also the 5K model: as expected it was suitable for subjects with slow kinetics and a large number of lines in the spectrum, instead for the others it was too complex to describe their data, in particular the exchange of the radioligand between the free pool and the non-specifically bound pool was rapid so that the rate costants k_5 and k_6 were not estimated and we recovered the 3K model. Using the Akaike Information Criterion we provided for each subject a comparison between the three models, 3K, 4K and 5K, in order to find the best and parsimonious solution. We have that for subjects 1814, 1804 and 1866 it is given by the 3K compartmental model, 1711 and 2300 are well described by the 5K model, lastly for 2241 the 4K model is the most suitable.
However, even if these models provide good estimates and fits of the measured data, with realistic trends of residuals, we are not able to find a correlation between these compartmental structures and the physiological information in hand,

e.g we can not give an explanation of the irreversible trapping of the tracer. Moreover the macroparameter V_d presents a too high variability, both inter and intra subject, which is not justifiable, as we can see in Figure 6.7, where we represent the boxplot[2] of these values for four subjects.

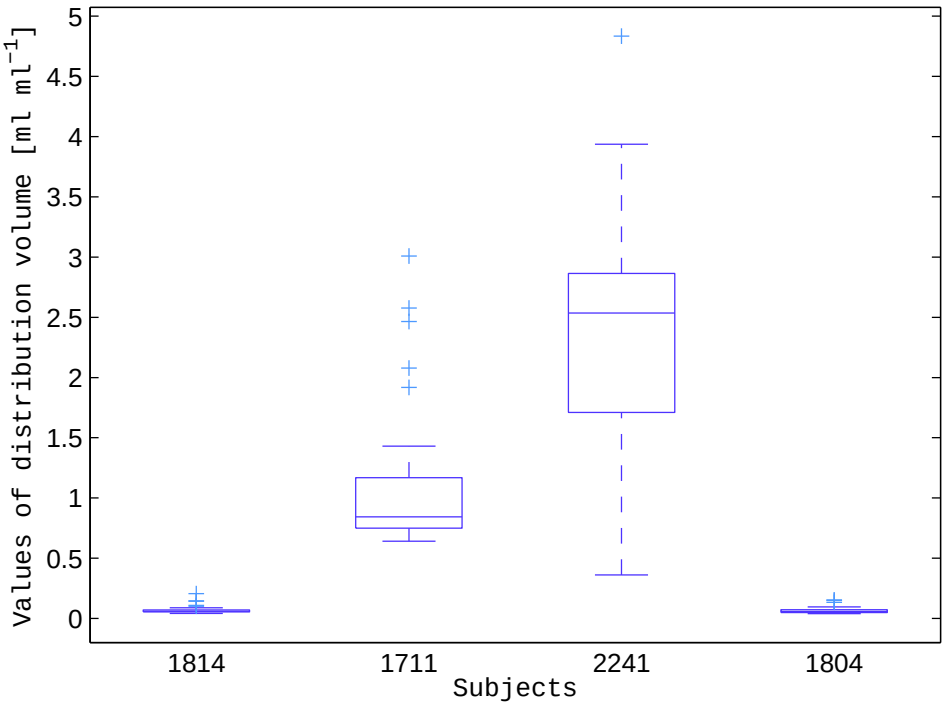

Figure 6.7: Representation through boxplots of the macroparameter V_d: the line inside the box is the median while the + represent the outliers. It is immediatly clear the high variability between the subjects

So after these results and thanks to the discovery of the significant blood presence, we set apart these three traditional models and focused our attention on the development of new compartmental structures.

[2]A boxplot is a simple way of graphically depicting groups of numerical data through their five-number summaries: the smallest observation (minimum sample), lower quartile (Q_1), median (Q_2), upper quartile (Q_3), and largest observation (maximum sample). It may also indicate which observations might be considered outliers.

6.3.2 Innovative Models for [^{11}C]SCH442416

The problems that we noticed using the tradional models and the high amount of blood in summed PET images lead us to the formulation of specific compartmental models for this tracer. In particular the results of SA applied to the ROI blood of each subject, suggest that the tracer concentration within the tissue can be described by a simple one-tissue compartment model, while an irreversible and a reversible compartment are necessary to depict its activity inside blood. This type of structure, with compartments releated to the blood presence and a compartment that represents the tissue, has a physiological validation, since we know that the adenosine A_{2A} receptors, which are the target subtype of our tracer, are selectively expressed not only in brain areas, but also in human endothelial cells and platelet membranes. In all the four tested compartmental models the irreversible trapping is in the vascular part, in agreement with the spectral lines we have found for each ROI blood, and so it represents a non-specific binding of the tracer.

Model 1

It is the first compartmental model that we evaluated with our PET data: it is a parallel structure, with an irreversible and a slow reversible compartment, that describe the vascular kinetics of the tracer, and one reversible tissue compartment, faster than the other one. We applied this model to all six subjects; looking the different results (that we show in the Table 5.17-5.20) it is immediatly clear that the "full" structure is able to describe the data of subjects 1711 and 2300; in subject 2241 the nonspecific trapping is not detected in the majority of ROIs, as previously found with the I/O models. Lastly for subjects 1814, 1804 and 1866 the rate costants k_1 and k_2 are very small and so they are not estimated by the algorithm, therefore for these ones the reversible compartment of vascular origin is not present, in agreement with the SA results, which in these cases does not detect slow reversible components.

Considering the reversible tissue compartment and in particular the rate costant k_6, which describes the exchange from tissue to plasma, it can be noticed that it assume low values in the brain areas with a large number of receptors, index that

here there is a specific binding of the tracer, instead for Cerebellum or Occipital Lobe the tracer rapidly returns to plasma since this receptor subtype is not present in high concentrations in these areas. As a consequence, the distribution volume of the tracer ($\frac{K_5}{k_6}$) within the tissue reaches the highest values in Caudate Nucleus, Putamen, Nucleus Accumbens and Globus Pallidus, while in the other areas the values are lower and fairly homogeneus. So this parameter is of great interest in our study since it correlates in a good way with the physiological information about the distribution of the A_{2A} receptors within the brain, while the irreversible trapping, being connected to the vascular part, does not reflect their characteristic localization in tissues. In fact, the microparameter k_3, which also represents the fractional uptake K, is only a rate costant and so its value does not depend on the number of receptors; moreover, reflecting the irreversible process inside blood vessels, we don't expect significant changes between the different ROIs of each subject. We show in Figure 6.8 the values of this microparameter for three of the four reliable subjects (2241 is not represents since the majority of ROIs don't present k_3): we have a quite homogeneus distribution for subject 1814 while 1711 presents some regions with 0 value (in concordance with the I/O result for the same ROIs). It is immediatly clear that this parameter is not influenced by the number of receptors and moreover it is not correlated with the blood volume term, i.e we don't find a high k_3 value in regions wih a large amount of blood, these because it only gives an idea of the velocity of trapping.

So V_d for the tissue is the macroparameter of our interesting: for each subject we sorted the values and divided them into 3 groups, with low-medium-high values of V_d, even if between the first two divisions there are not very remarked differences. In this way we wanted to know if it really correlated with the expected regional A_{2A} distribution in each subject and if there was a shared trend. We show these divisions in Figure 6.9, where we underline the position of the interesting ROIs: Cerebellum and Anterior Cingulate Gyrus are always in the first two groups, even if Cerebellum is not in the first positions as expected, index that here there is a specific binding of the tracer, and so probably can not be considered the reference region as in the previous works. Instead the rich regions are in practice in the last group and this is particularly evident for subject 2241,

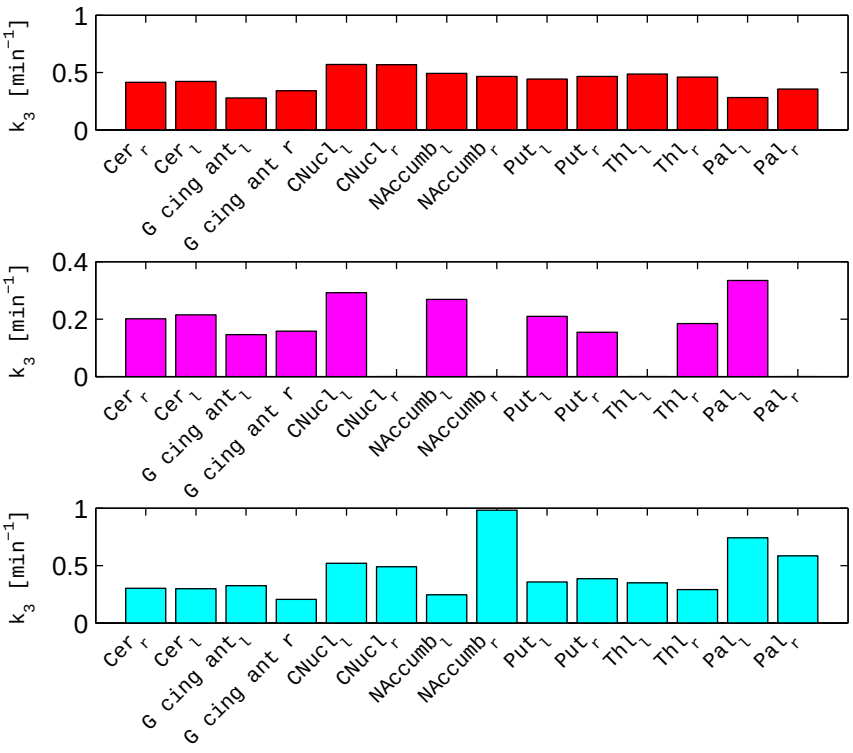

Figure 6.8: Representation of k_3 values for the most important ROIs. Top: 1814; Center: 1711; Bottom: 1866

who is also the one with the higher intra variability for this parameter.
We evaluated also the fit of the data, which was good for all the subjects (except for 1804 who has probably problems in the input function), and the trends of weighted residuals, which reflect the assumptions on the measurement error. Except for some small ROIs, as Nucleus Accumbens or Globus Pallidus, the CVs are good for all the subjects and for all the parameters, especially for k_5 and V_d (Table 6.12-15).

ROI	$K_5[ml ml^{-1} min^{-1}]$	*cv*	$k_6[min^{-1}]$	*cv*	Vd $[ml ml^{-1}]$	*cv*	$k_3[min^{-1}]$	*cv*	$V_b[unitless]$	*cv*
$Cerebellum_r$	0.0382	(37)	0.9039	(36)	0.0422	(17)	0.4140	(25)	0.0287	(24)
$Cerebellum_l$	0.0355	(29)	0.7482	(29)	0.0474	(14)	0.4229	(22)	0.0280	(21)
G cing ant_l	0.0283	(36)	0.6861	(36)	0.0413	(18)	0.2777	(18)	0.0436	(16)
G cing ant_r	0.0180	(58)	0.7175	(57)	0.0251	(30)	0.3407	(22)	0.0330	(21)
$CaudateNucl_l$	0.0346	(26)	0.5980	(27)	0.0579	(13)	0.5694	(27)	0.0213	(26)
$CaudateNucl_r$	0.0330	(23)	0.4452	(25)	0.0741	(13)	0.5688	(31)	0.0203	(30)
$NuclAccumb_l$	0.0146	(64)	0.3082	(72)	0.0474	(41)	0.4931	(53)	0.0243	(51)
$NuclAccumb_r$	0.0267	(49)	0.3682	(53)	0.0724	(28)	0.4664	(52)	0.0270	(50)
$Putamen_l$	0.0405	(16)	0.3720	(17)	0.1088	(9)	0.4425	(21)	0.0305	(20)
$Putamen_r$	0.0402	(17)	0.3822	(18)	0.1053	(10)	0.4660	(22)	0.0302	(21)
$Thalamus_l$	0.0382	(39)	0.9714	(38)	0.0393	(18)	0.4862	(26)	0.0268	(25)
$Thalamus_r$	0.0290	(48)	0.7585	(48)	0.0382	(24)	0.4610	(31)	0.0266	(30)
$Pallidum_l$	0.0120	(140)	0.2408	(168)	0.0499	(100)	0.2827	(95)	0.0331	(89)
$Pallidum_r$	0.0183	(44)	0.1353	(57)	0.1355	(37)	0.3550	(70)	0.0278	(66)

Table 6.12: Subject 1814-Model 1

ROI	$K_5[ml ml^{-1} min^{-1}]$	*cv*	$k_6[min^{-1}]$	*cv*	Vd $[ml ml^{-1}]$	*cv*	$k_3[min^{-1}]$	*cv*	$V_b[unitless]$	*cv*
$Cerebellum_r$	0.0546	(15)	0.6215	(15)	0.0878	(8)	0.3020	(14)	0.0451	(13)
$Cerebellum_l$	0.0536	(17)	0.6124	(16)	0.0875	(8)	0.2981	(15)	0.0454	(14)
G cing ant_l	0.0370	(20)	0.5003	(20)	0.0739	(11)	0.3239	(15)	0.0449	(14)
G cing ant_r	0.0385	(18)	0.4954	(17)	0.0778	(0)	0.2064	(10)	0.0660	(10)
$CaudateNucl_l$	0.0564	(8)	0.2282	(9)	0.2471	(5)	0.5200	(20)	0.0305	(20)
$CaudateNucl_r$	0.0528	(7)	0.2515	(8)	0.2101	(4)	0.4890	(15)	0.0303	(15)
$NuclAccumb_l$	0.0317	(28)	0.2070	(32)	0.1534	(18)	0.2446	(31)	0.0561	(29)
$NuclAccumb_r$	0.0546	(43)	0.6292	(43)	0.0868	(22)	0.9811	(91)	0.0144	(89)
$Putamen_l$	0.0550	(5)	0.2036	(6)	0.2699	(3)	0.3562	(10)	0.0429	(9)
$Putamen_r$	0.0511	(7)	0.1917	(8)	0.2665	(4)	0.3861	(15)	0.0412	(14)
$Thalamus_l$	0.0425	(16)	0.4211	(16)	0.1010	(8)	0.3489	(19)	0.0363	(18)
$Thalamus_r$	0.0416	(19)	0.4725	(19)	0.0880	(10)	0.2905	(16)	0.0475	(15)
$Pallidum_l$	0.0152	(27)	0.1112	(38)	0.1365	(26)	0.7412	(57)	0.0159	(55)
$Pallidum_r$	0.0368	(21)	0.1759	(26)	0.2090	(15)	0.5848	(55)	0.0236	(53)

Table 6.13: Subject 1866-Model 1

ROI	$K_5[ml ml^{-1} min^{-1}]$	*cv*	$k_6[min^{-1}]$	*cv*	Vd $[ml ml^{-1}]$	*cv*	$k_3[min^{-1}]$	*cv*	$k_1[min^{-1}]$	*cv*	$k_2[min^{-1}]$	*cv*	$V_b[unitless]$	*cv*
$Cerebellum_r$	0.0330	(2)	0.2372	(5)	0.1392	(3)	-		0.1717	(12)	0.0078	(9)	0.0983	(5)
$Cerebellum_l$	0.0356	(2)	0.2267	(6)	0.1571	(4)	-		0.1669	(11)	0.0068	(8)	0.1033	(5)
G cing ant_l	0.0274	(5)	0.1974	(15)	0.1386	(10)	-		0.1778	(26)	0.0062	(21)	0.0887	(11)
G cing ant_r	0.0195	(44)	0.1420	(207)	0.1375	(247)	0.0471	(157)	0.0818	(32)	0.0140	(57)	0.1331	(9)
$CaudateNucl_l$	0.0575	(13)	0.2198	(16)	0.2617	(10)	-		0.1700	(23)	0.0048	(28)	0.0866	(17)
$CaudateNucl_r$	0.0608	(11)	0.2172	(38)	0.2800	(28)	-		0.2192	(45)	0.0051	(20)	0.0624	(32)
$NuclAccumb_l$	0.0337	(30)	0.0991	(37)	0.3404	(24)	0.1056	(40)	-		-		0.1249	(31)
$NuclAccumb_r$	0.0290	(26)	0.1151	(32)	0.2522	(18)	0.1068	(35)	-		-		0.1048	(25)
$Putamen_l$	0.0781	(6)	0.2063	(13)	0.3787	(8)	-		0.1751	(18)	0.0078	(10)	0.1031	(12)
$Putamen_r$	0.0534	(19)	0.1937	(36)	0.2757	(48)	0.0819	(21)	0.1037	(91)	0.0429	(81)	0.1129	(13)
$Thalamus_l$	0.0393	(4)	0.3065	(10)	0.1281	(7)	-		0.1488	(27)	0.0067	(20)	0.1210	(9)
$Thalamus_r$	0.0453	(14)	0.2444	(17)	0.1852	(10)	-		0.1904	(17)	0.0049	(18)	0.0878	(14)
$Pallidum_l$	0.0530	(16)	0.1377	(17)	0.3848	(10)	0.1109	(30)	-		-		0.1117	(25)
$Pallidum_r$	0.0565	(19)	0.1816	(26)	0.3113	(17)	-		0.1548	(39)	0.0036	(69)	0.0947	(29)

Table 6.14: Subject 2241-Model 1

ROI	$K_5[ml ml^{-1} min^{-1}]$	cv	$k_6[min^{-1}]$	cv	Vd $[ml ml^{-1}]$	cv	$k_3[min^{-1}]$	cv	$k_1[min^{-1}]$	cv	$k_2[min^{-1}]$	cv	$V_b[unitless]$	cv
$Cerebellum_r$	0.0709	(5)	0.3384	(8)	0.2095	(7)	0.2015	(10)	0.2651	(11)	0.0292	(22)	0.0486	(6)
$Cerebellum_l$	0.0712	(4)	0.3476	(7)	0.2047	(6)	0.2150	(8)	0.2889	(9)	0.0312	(17)	0.0464	(5)
G cing ant_l	0.0530	(9)	0.3306	(19)	0.1603	(18)	0.1462	(11)	0.3010	(19)	0.0430	(20)	0.0639	(8)
G cing ant_r	0.0526	(19)	0.3713	(37)	0.1417	(35)	0.1576	(17)	0.3459	(35)	0.0560	(29)	0.0637	(14)
$CaudateNucl_l$	0.0711	(11)	0.2757	(21)	0.2578	(27)	0.2919	(15)	0.6085	(40)	0.0599	(27)	0.0401	(19)
$CaudateNucl_r$	0.0711	(6)	0.2224	(9)	0.3198	(6)	-		0.6184	(18)	0.0094	(10)	0.0329	(16)
$NuclAccumb_l$	0.0654	(20)	0.2582	(41)	0.2533	(43)	0.2688	(53)	0.5228	(58)	0.0319	(83)	0.0377	(35)
$NuclAccumb_r$	0.0660	(19)	0.2155	(29)	0.3063	(22)	-		0.4973	(50)	0.0113	(28)	0.0388	(43)
$Putamen_l$	0.0853	(8)	0.2276	(16)	0.3747	(19)	0.2093	(18)	0.4046	(33)	0.0381	(38)	0.0492	(12)
$Putamen_r$	0.0882	(6)	0.2129	(12)	0.4143	(13)	0.1543	(67)	0.4857	(19)	0.0207	(60)	0.0386	(15)
$Thalamus_l$	0.0728	(6)	0.2678	(8)	0.2719	(5)	-		0.3697	(11)	0.0076	(9)	0.0542	(9)
$Thalamus_r$	0.0776	(8)	0.2986	(15)	0.2599	(12)	0.1845	(40)	0.2326	(21)	0.0203	(77)	0.0523	(13)
$Pallidum_l$	0.0485	(28)	0.1992	(48)	0.2437	(69)	0.3345	(38)	1.2681	(58)	0.0427	(44)	0.0259	(30)
$Pallidum_r$	0.0473	(14)	0.1542	(29)	0.3066	(27)	-		0.8511	(38)	0.0173	(17)	0.0316	(31)

Table 6.15: Subject 1711-Model 1

Subject 1814		Subject 1711		Subject 2241		Subject 1866	
G cing ant_r	0.0251	Amygdala_l	0.1351	Ant TL med_r	0.0378	Hippocampus_l	0.0677
Pallidum_l	0.0293	G cing ant_r	0.1429	G paraH amb_r	0.0699	ParietalLob_l	0.0696
G paraH amb_r	0.0309	Hippocampus_r	0.143	G occtem la_r	0.0834	G sup temp_r	0.0706
Hippocampus_r	0.032	ParietalLob_l	0.1455	G paraH amb_l	0.0891	G paraH amb_l	0.072
G occtem la_l	0.0321	Hippocampus_l	0.15	FrontalLobe_r	0.0996	ParietalLob_r	0.0726
G paraH amb_l	0.0328	FrontalLobe_l	0.1504	Ant lat_r	0.1018	FrontalLobe_r	0.0729
G occtem la_r	0.0329	ParietalLob_r	0.1513	FrontalLobe_l	0.1054	G cing ant_l	0.0739
G cing post_r	0.034	FrontalLobe_r	0.154	ParietalLob_l	0.1059	FrontalLobe_l	0.0739
Insula_r	0.0353	G paraH amb_l	0.1576	Ant lat_l	0.1084	G occtem la_l	0.0741
FrontalLobe_l	0.036	G sup temp_r	0.1576	G occtem la_l	0.1085	G occtem la_r	0.0747
Ant TL med_l	0.036	G cing ant_l	0.16	OccipitLobe_l	0.1103	G sup temp_l	0.0755
FrontalLobe_r	0.0365	OccipitLobe_l	0.161	ParietalLob_r	0.117	G cing ant_r	0.0777
Amygdala_r	0.0378	OccipitLobe_r	0.1639	G tem midin_r	0.1193	Ant TL med_r	0.08
ParietalLob_l	0.038	PosteriorTL_l	0.1696	Hippocampus_r	0.1217	OccipitLobe_r	0.0815
Ant TL med_r	0.0381	Ant lat_l	0.1703	OccipitLobe_r	0.123	G tem midin_r	0.0838
Thalamus_r	0.0382	Ant TL med_l	0.172	G cing post_r	0.1274	Amygdala_r	0.0855
Hippocampus_l	0.0383	G tem midin_l	0.1743	Thalamus_l	0.1282	G tem midin_l	0.0858
G sup temp_l	0.0388	PosteriorTL_r	0.1748	G sup temp_r	0.1334	Ant lat_r	0.0861
Ant lat_r	0.039	G cing post_r	0.1751	G cing ant_r	0.1365	G paraH amb_r	0.0862
Thalamus_l	0.0391	G paraH amb_r	0.1759	G cing ant_l	0.1388	NuclAccumb_r	0.0867
G cing ant_l	0.0412	G sup temp_l	0.1772	Cerebellum_r	0.1391	Cerebellum_l	0.0874
ParietalLob_r	0.0417	Insula_l	0.1842	PosteriorTL_r	0.1396	Cerebellum_r	0.0878

(a) Low values

Cerebellum_r	0.0422	Ant TL med_r	0.1869	G sup temp_l	0.1475	PosteriorTL_r	0.0879
Amygdala_l	0.0429	G occtem la_r	0.1942	G tem midin_l	0.1499	Thalamus_r	0.0879
G tem midin_l	0.0433	G cing post_l	0.1945	G cing post_l	0.1562	G cing post_r	0.0881
Ant lat_l	0.0446	Ant lat_r	0.1946	Cerebellum_l	0.1572	G cing post_l	0.0882
G tem midin_r	0.0446	G tem midin_r	0.2028	PosteriorTL_l	0.1581	Amygdala_l	0.0893
OccipitLobe_l	0.0451	Cerebellum_l	0.2045	Ant TL med_l	0.1663	Insula_l	0.0899
G sup temp_r	0.0457	Cerebellum_r	0.2093	Hippocampus_l	0.1689	OccipitLobe_l	0.0904
Insula_l	0.0468	Amygdala_r	0.2381	Insula_r	0.1736	Hippocampus_r	0.0912
PosteriorTL_l	0.0472	Pallidum_l	0.2434	Amygdala_r	0.1775	PosteriorTL_l	0.0914
G cing post_l	0.0474	G occtem la_l	0.2449	Thalamus_r	0.1854	Ant lat_l	0.0962
Cerebellum_l	0.0474	NuclAccumb_l	0.2506	Insula_l	0.1939	Ant TL med_l	0.0997
NuclAccumb_l	0.0476	CaudateNucl_l	0.259	Amygdala_l	0.2159	Thalamus_l	0.1009
PosteriorTL_r	0.0498	Thalamus_r	0.2596	NuclAccumb_r	0.2523	Insula_r	0.1085
OccipitLobe_r	0.0553	Thalamus_l	0.2716	CaudateNucl_l	0.2618	NuclAccumb_l	0.1248
CaudateNucl_l	0.0578	Insula_r	0.2766	Putamen_r	0.2745	Pallidum_l	0.1365
NuclAccumb_r	0.0727	NuclAccumb_r	0.3059	CaudateNucl_r	0.2797	CaudateNucl_r	0.2085
CaudateNucl_r	0.0743	Pallidum_r	0.3065	Pallidum_r	0.3115	Pallidum_r	0.2089
Putamen_r	0.1052	CaudateNucl_r	0.3198	NuclAccumb_l	0.3407	CaudateNucl_l	0.2469
Putamen_l	0.1087	Putamen_l	0.3742	Putamen_l	0.3786	Putamen_r	0.2667
Pallidum_r	0.1345	Putamen_r	0.4126	Pallidum_l	0.3849	Putamen_l	0.2699

(b) Medium and high values

Figure 6.9: Distribution volume values for four subjects with Model 1

Model 2

Starting from the structure of Model 1 and noting that only for some subjects the blood reversible compartement was required, to have a full-view we tested another possible configuration with the same number of compartments and rate costants. In this case only the irreversible process is related to blood while the tracer activity in the tissue is described by two reversible compartments. Also for this model the net uptake rate costant is given by k_3 and it is not identifiable for subject 2241, as previously, and being connected to blood it does not give us relevant information.

The macroparameter V_d for the tissue is given by $\frac{K_1}{k_2}\left(1+\frac{k_3}{k_4}\right)$, but for subjects 1814, 1866 and 1804 the algorithm is not able to identify the rate costants k_3 and k_4 in many ROIs and so the V_d is given again by $\frac{K_1}{k_2}$. In this case this parameter does not correlate with the physiological information, in fact we find for some

subjects low values in corrispondence of ROIs with a large number of receptors, e.g Nucleus Accumbens and Putamen of subject 2241, and, on the contrary, higher values in areas like Cerebellum. In particular, this subject presents higher V_d, $2 \div 3$ $[ml ml^{-1}]$, also by comparison with subject 1711, who usually has a similar pattern. Moreover we find a more remarked variability than the values that we have found with Model 1, both intra (also between the left and the right part of the same ROI) and inter subject, as we can clearly see in Figure 6.10, where we consider only four subjects. Even if the model-estimated curves are able to describe the data and the CV of estimates are low, this high variability, which is not physiological, led us to reject this model configuration.

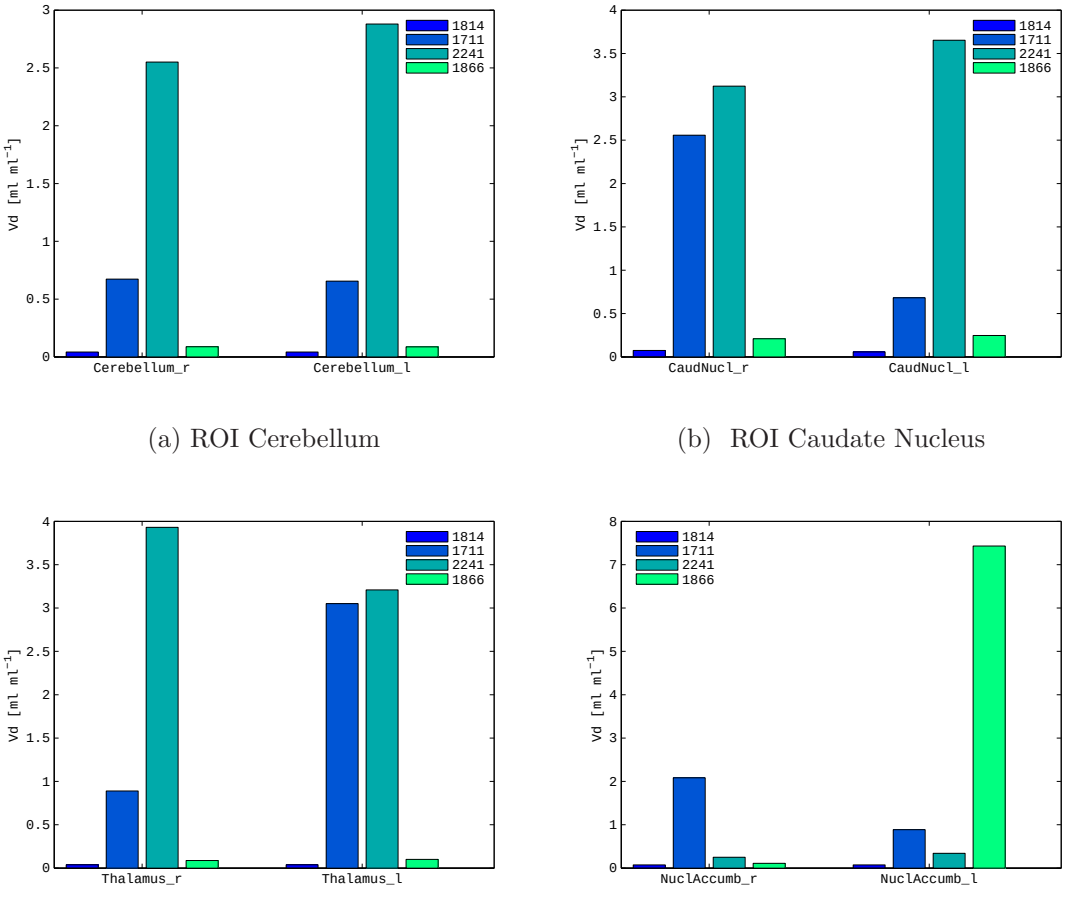

(a) ROI Cerebellum

(b) ROI Caudate Nucleus

(c) ROI Thalamus

(d) ROI Nucleus Accumbens

Figure 6.10: Distribution volume for tissue with Model 2. Particularly evident is the variability between subject 2241, who has high values, and the others

Model 3 and Model 4

As previously explained, the time course of parent compound shows the presence of a significant amount of metabolites (differently from rats and monkeys) and this observation suggested us to test both the I/O model with a double input function (see Section 6.2.2) and new compartmental models accounting for their presence. These new structures have two different arterial input functions: the parent plasma concentration $C_p(t)$, i.e corrected for metabolites, and the total plasma concentration $C_{tp}(t)$, i.e with also the metabolites. The results of the SA approach with the two inputs did not give an unique interpretation of the behaviour of the metabolites, in particular from the interpretation of the different spectra of each subject we were not able to clearly distinguish if the trapping or the low reversible component were due to the metabolites presence. For this reason we decided to test on four of the six subjects two possible configurations, first of all Model 3 which has the irreversible process connected to the metabolites. We can summerize the results that we have found as (Table 6.16-19):

- subject 1814 $\Rightarrow$ the rate costant k_2 is very small, ≈ 0, for all the ROIs and the irreversible trapping is split into two parts, in fact we have $k_1 = 0.27 \pm 0.08$ and $k_3 = 0.07 \pm 0.03$, which is significantly smaller than the component connected to $C_p(t)$ and it is due to metabolites; the values of k_6 are very different from the ones of Model 1 (Model 3: $k_6 = 0.33 \pm 0.15$; Model 1= $k_6 = 0.52 \pm 0.27$);

- subject 1711 $\Rightarrow$ the full model is able to describe the data of each ROI, only a few do not present the rate costant k_3; also in this case the values of k_3 are low (0.06±0.02); the values of the parameters connected to the tissue compartment are very similar to the one that we have found with Model 1 (Model 3: $K_5 = 0.07 \pm 0.01$ $k_6 = 0.26 \pm 0.06$; Model 1: $K_5 = 0.07 \pm 0.01$ $k_6 = 0.27 \pm 0.06$);

- subject 2241 $\Rightarrow$ almost all the ROIs have $k3 \approx 0$, the rate costant k_2 is very low (0.008±0.007) and also in this case the tissue values are quite similar to the same that we have found with Model 1 (Model 3: $K_5 = 0.05 \pm 0.02$ $k_6 = 0.18 \pm 0.07$; Model 1: $K_5 = 0.04 \pm 0.02$ $k_6 = 0.19 \pm 0.06$);

- subject 1866 $\Rightarrow$ is very similar to 1814; $k_2 \approx 0$ for all the ROIs and so also in this case the trapping is split, $k_1 = 0.29 \pm 0.18$ $k_3 = 0.08 \pm 0.1$; the values of k_6 are significantly different from the ones of Model 1.

Considering the different numerical results, it seems that the irreversible process requires a long time to be attuated, i.e the metabolites are slowly trapped and for the subjects with the splitted irreversible component the one connected to $C_p(t)$ is more remarked. About the distribution volume V_d in the tissue, the values for subjects 1711 and 2241 are almost equal to the ones we have calculated with Model 1 (since K_5 and k_6 are the same), instead for 1814 and 1866 V_d is a bit higher. Also in this case its values reflect and correlate with the adenosine A_{2A} receptor distribution within the brain and we report in Figure 6.11 the values for each subject, divided as previously in three groups. Areas like Striatum and Globus Pallidus with a large number of receptors are collocated in the last group, and this is the index that the $V_d s$ calculated with Model 3 are correlated to the physiological information too.

Subject 1814		Subject 1711		Subject 2241		Subject 1866	
G cing ant_r	0.0397	Hippocampus_r	0.1534	Ant TL med_r	0.0377	Hippocampus_l	0.0676
G occtem la_l	0.0445	Amygdala_l	0.154	G paraH amb_r	0.07	G occtem la_l	0.0767
FrontalLobe_l	0.0484	G cing ant_r	0.1579	G occtem la_r	0.0832	ParietalLob_l	0.0779
G occtem la_r	0.0493	ParietalLob_l	0.1579	G paraH amb_l	0.0892	ParietalLob_r	0.0839
Ant TL med_r	0.0493	FrontalLobe_l	0.1603	FrontalLobe_r	0.0996	G cing ant_l	0.0867
G cing post_r	0.0493	FrontalLobe_r	0.1625	Ant lat_r	0.1032	FrontalLobe_l	0.0883
FrontalLobe_r	0.0499	ParietalLob_r	0.163	FrontalLobe_l	0.1054	G sup temp_r	0.0888
ParietalLob_l	0.0506	Hippocampus_l	0.1646	ParietalLob_l	0.1059	FrontalLobe_r	0.0892
Amygdala_r	0.051	G sup temp_r	0.1647	G occtem la_l	0.1097	Ant TL med_r	0.0897
G cing ant_l	0.0523	G cing ant_l	0.1694	OccipitLobe_l	0.1105	G cing ant_r	0.0908
Ant TL med_l	0.0527	OccipitLobe_l	0.1726	Ant lat_l	0.1107	G paraH amb_l	0.0916
G paraH amb_l	0.0532	OccipitLobe_r	0.1747	ParietalLob_r	0.1169	G sup temp_l	0.0921
ParietalLob_r	0.0533	Ant lat_l	0.1754	Hippocampus_r	0.1212	OccipitLobe_r	0.0934
Thalamus_l	0.0535	Ant TL med_l	0.1802	OccipitLobe_r	0.1231	NuclAccumb_r	0.0943
G paraH amb_r	0.0536	G paraH amb_r	0.1824	G tem midin_r	0.1232	G cing post_l	0.0948
Ant lat_r	0.0537	G cing post_r	0.1825	Thalamus_l	0.1281	Hippocampus_r	0.0964
Hippocampus_r	0.0538	PosteriorTL_l	0.1825	G cing post_r	0.1312	OccipitLobe_l	0.0979
Amygdala_l	0.056	PosteriorTL_r	0.1853	G sup temp_r	0.1336	G cing post_r	0.1006
G sup temp_l	0.0562	G tem midin_l	0.1855	G cing ant_l	0.1386	G tem midin_l	0.1009
NuclAccumb_l	0.0576	G sup temp_l	0.1884	Cerebellum_r	0.139	Ant lat_l	0.1014
OccipitLobe_l	0.058	G paraH amb_l	0.1925	PosteriorTL_r	0.1396	PosteriorTL_r	0.1042

(a) Low values

G tem midin_l	0.058	Ant TL med_r	0.1928	G tem midin_l	0.1499	Ant TL med_l	0.1042
Insula_r	0.0582	G cing post_l	0.1979	G sup temp_l	0.152	Cerebellum_r	0.1056
Ant lat_l	0.0587	G occtem la_r	0.1993	G cing post_l	0.1562	Insula_l	0.1058
Hippocampus_l	0.0594	Insula_l	0.1997	Cerebellum_l	0.1571	Thalamus_r	0.1059
Cerebellum_r	0.0598	Ant lat_r	0.2021	PosteriorTL_l	0.1582	G paraH amb_r	0.1067
G tem midin_r	0.0609	Cerebellum_l	0.2133	G cing ant_r	0.1598	PosteriorTL_l	0.1069
G sup temp_r	0.0611	G tem midin_r	0.2143	Insula_r	0.1769	Cerebellum_l	0.1075
PosteriorTL_l	0.0633	Cerebellum_r	0.2186	Amygdala_r	0.1772	G tem midin_r	0.1085
OccipitLobe_r	0.0645	Amygdala_r	0.2383	Hippocampus_l	0.1809	Amygdala_l	0.1087
Cerebellum_l	0.0645	NuclAccumb_l	0.2555	Thalamus_r	0.1854	Ant lat_r	0.1146
Thalamus_r	0.0655	G occtem la_l	0.2566	Insula_l	0.1941	Thalamus_l	0.125
Insula_l	0.067	Pallidum_l	0.2601	Ant TL med_l	0.1967	G occtem la_r	0.1314
PosteriorTL_r	0.0673	Thalamus_r	0.268	Amygdala_l	0.2152	Insula_r	0.1471
G cing post_l	0.072	Thalamus_l	0.2716	CaudateNucl_l	0.2617	Amygdala_r	0.1488
CaudateNucl_l	0.0759	CaudateNucl_l	0.2859	CaudateNucl_r	0.28	NuclAccumb_l	0.1532
CaudateNucl_r	0.0936	Insula_r	0.2904	Putamen_r	0.2852	CaudateNucl_r	0.2101
Pallidum_l	0.1317	NuclAccumb_r	0.3045	Pallidum_r	0.3123	CaudateNucl_l	0.265
Putamen_r	0.1395	Pallidum_r	0.306	Putamen_l	0.3785	Putamen_l	0.2818
Putamen_l	0.142	CaudateNucl_r	0.3197	NuclAccumb_r	0.4823	Pallidum_l	0.2886
NuclAccumb_r	0.1425	Putamen_l	0.3953	Pallidum_l	0.5975	Putamen_r	0.3067
Pallidum_r	0.1596	Putamen_r	0.4291	NuclAccumb_l	0.6092	Pallidum_r	0.3188

(b) Medium and high values

Figure 6.11: Distribution Volume V_d with Model 3

ROI	$K_5[ml ml^{-1} min^{-1}]$	cv	$k_6[min^{-1}]$	cv	$V_d[ml ml^{-1}]$	cv	$k_3[min^{-1}]$	cv	$k_1[min^{-1}]$	cv	$k_2[min^{-1}]$	cv	$V_b[unitless]$	cv
$Cerebellum_r$	0.032	(12)	0.534	(13)	0.060	(7)	0.073	(13)	0.227	(13)	-	-	0.031	(10)
$Cerebellum_l$	0.031	(11)	0.486	(13)	0.065	(7)	0.066	(14)	0.255	(13)	-	-	0.030	(10)
G cing ant_l	0.027	(25)	0.510	(27)	0.052	(15)	0.029	(31)	0.208	(18)	-	-	0.045	(13)
G cing ant_r	0.016	(29)	0.405	(34)	0.040	(19)	0.048	(26)	0.224	(20)	-	-	0.035	(15)
$CaudateNucl_l$	0.031	(15)	0.409	(18)	0.076	(10)	0.078	(27)	0.365	(22)	-	-	0.023	(18)
$CaudateNucl_r$	0.032	(16)	0.341	(19)	0.094	(12)	0.078	(36)	0.377	(29)	-	-	0.021	(24)
$NuclAccumb_l$	0.016	(55)	0.274	(73)	0.058	(48)	0.033	(147)	0.427	(62)	-	-	0.024	(52)
$NuclAccumb_r$	0.024	(23)	0.167	(37)	0.143	(28)	0.132	(45)	0.120	(95)	-	-	0.031	(35)
$Putamen_l$	0.039	(8)	0.273	(10)	0.142	(6)	0.073	(18)	0.261	(16)	-	-	0.032	(12)
$Putamen_r$	0.038	(9)	0.274	(11)	0.139	(7)	0.077	(20)	0.275	(18)	-	-	0.032	(13)
$Thalamus_l$	0.031	(18)	0.586	(19)	0.054	(10)	0.068	(19)	0.303	(16)	-	-	0.029	(13)
$Thalamus_r$	0.023	(14)	0.358	(16)	0.065	(10)	0.097	(15)	0.211	(17)	-	-	0.029	(12)
$Pallidum_l$	0.017	(56)	0.129	(65)	0.132	(41)	0.138	(90)	-	-	-	-	0.031	(84)
$Pallidum_r$	0.019	(39)	0.121	(78)	0.160	(71)	0.032	(317)	0.281	(121)	-	-	0.028	(68)

Table 6.16: Subject 1814-Model 3

ROI	$K_5[ml ml^{-1} min^{-1}]$	cv	$k_6[min^{-1}]$	cv	$V_d[ml ml^{-1}]$	cv	$k_3[min^{-1}]$	cv	$k_1[min^{-1}]$	cv	$k_2[min^{-1}]$	cv	$V_b[unitless]$	cv
$Cerebellum_r$	0.071	(4)	0.327	(7)	0.219	(6)	0.054	(13)	0.377	(9)	0.024	(17)	0.049	(6)
$Cerebellum_l$	0.072	(4)	0.337	(6)	0.213	(5)	0.058	(10)	0.407	(7)	0.025	(13)	0.047	(5)
G cing ant_l	0.054	(8)	0.320	(10)	0.169	(8)	0.043	(10)	0.375	(9)	0.036	(11)	0.064	(7)
G cing ant_r	0.055	(17)	0.346	(31)	0.158	(28)	0.048	(18)	0.406	(26)	0.043	(22)	0.064	(14)
$CaudateNucl_l$	0.075	(8)	0.262	(16)	0.286	(18)	0.089	(16)	0.694	(26)	0.044	(19)	0.040	(13)
$CaudateNucl_r$	0.071	(6)	0.223	(9)	0.320	(6)	-		0.619	(18)	0.009	(10)	0.033	(16)
$NuclAccumb_l$	0.066	(19)	0.260	(38)	0.256	(37)	0.078	(56)	0.691	(51)	0.029	(59)	0.037	(35)
$NuclAccumb_r$	0.066	(22)	0.218	(37)	0.304	(35)	-	-	0.502	(55)	0.011	(61)	0.039	(33)
$Putamen_l$	0.087	(6)	0.221	(13)	0.395	(15)	0.058	(23)	0.497	(23)	0.030	(30)	0.049	(12)
$Putamen_r$	0.089	(5)	0.208	(11)	0.429	(10)	0.032	(101)	0.563	(19)	0.017	(55)	0.039	(14)
$Thalamus_l$	0.073	(6)	0.268	(8)	0.272	(5)	-		0.370	(11)	0.008	(9)	0.054	(9)
$Thalamus_r$	0.078	(8)	0.292	(13)	0.268	(11)	0.046	(52)	0.343	(17)	0.018	(57)	0.052	(13)
$Pallidum_l$	0.051	(16)	0.195	(18)	0.260	(27)	0.098	(22)	-	-	-	-	0.026	(21)
$Pallidum_r$	0.047	(15)	0.155	(29)	0.306	(28)	-	-	0.853	(38)	0.017	(17)	0.032	(31)

Table 6.17: Subject 1711-Model 3

ROI	$K_5[ml ml^{-1} min^{-1}]$	*cv*	$k_6[min^{-1}]$	*cv*	$V_d[ml ml^{-1}]$	*cv*	$k_3[min^{-1}]$	*cv*	$k_1[min^{-1}]$	*cv*	$k_2[min^{-1}]$	*cv*	$V_b[unitless]$	*cv*
$Cerebellum_r$	0.033	(8)	0.238	(9)	0.139	(6)	-	-	0.172	(7)	0.008	(5)	0.098	(5)
$Cerebellum_l$	0.036	(7)	0.227	(8)	0.157	(5)	-	-	0.167	(6)	0.007	(6)	0.100	(5)
G cing ant_l	0.027	(16)	0.197	(21)	0.139	(14)	-	-	0.178	(14)	0.006	(15)	0.089	(11)
G cing ant_r	0.021	(16)	0.129	(27)	0.160	(22)	-	-	0.119	(14)	0.006	(22)	0.134	(8)
$CaudateNucl_l$	0.058	(13)	0.220	(16)	0.262	(10)	-	-	0.170	(23)	0.005	(27)	0.087	(17)
$CaudateNucl_r$	0.061	(16)	0.217	(19)	0.280	(12)	-	-	0.219	(38)	0.005	(37)	0.062	(32)
$NuclAccumb_l$	0.040	(16)	0.066	(21)	0.609	(13)	0.031	(32)	-	-	-	-	0.130	(26)
$NuclAccumb_r$	0.031	(14)	0.064	(18)	0.482	(11)	0.028	(25)	-	-	-	-	0.116	(20)
$Putamen_l$	0.078	(7)	0.207	(9)	0.378	(6)	-	-	0.175	(16)	0.008	(13)	0.103	(12)
$Putamen_r$	0.055	(12)	0.194	(26)	0.285	(29)	0.020	(31)	0.152	(38)	0.028	(52)	0.114	(13)
$Thalamus_l$	0.039	(18)	0.307	(19)	0.128	(11)	-	-	0.149	(12)	0.007	(10)	0.121	(9)
$Thalamus_r$	0.045	(14)	0.244	(17)	0.185	(10)	-	-	0.190	(17)	0.005	(18)	0.088	(14)
$Pallidum_l$	0.050	(37)	0.139	(56)	0.356	(87)	0.029	(41)	0.093	(184)	0.029	(204)	0.110	(18)
$Pallidum_r$	0.056	(19)	0.180	(26)	0.312	(17)	-	-	0.154	(39)	0.004	(68)	0.095	(29)

Table 6.18: Subject 2241-Model 3

ROI	$K_5[ml ml^{-1} min^{-1}]$	cv	$k_6[min^{-1}]$	cv	$V_d[ml ml^{-1}]$	cv	$k_3[min^{-1}]$	cv	$k_1[min^{-1}]$	cv	$k_2[min^{-1}]$	cv	$V_b[unitless]$	cv
$Cerebellum_r$	0.048	(7)	0.456	(8)	0.106	(4)	0.047	(12)	0.176	(10)	-	-	0.050	(6)
$Cerebellum_l$	0.046	(7)	0.432	(8)	0.108	(4)	0.051	(12)	0.161	(11)	-	-	0.051	(6)
G cing ant_l	0.035	(16)	0.399	(18)	0.087	(11)	0.032	(37)	0.242	(18)	-	-	0.048	(12)
G cing ant_r	0.035	(14)	0.381	(16)	0.091	(9)	0.021	(32)	0.154	(14)	-	-	0.070	(8)
$CaudateNucl_l$	0.056	(7)	0.212	(11)	0.265	(7)	0.037	(80)	0.430	(26)	-	-	0.031	(19)
$CaudateNucl_r$	0.053	(7)	0.252	(8)	0.210	(4)	-	-	0.489	(16)	-	-	0.030	(15)
$NuclAccumb_l$	0.032	(29)	0.208	(32)	0.153	(19)	-	-	0.245	(31)	-	-	0.056	(29)
$NuclAccumb_r$	0.047	(42)	0.504	(47)	0.094	(25)	0.051	(206)	0.747	(87)	-	-	0.017	(77)
$Putamen_l$	0.055	(4)	0.194	(7)	0.282	(5)	0.016	(91)	0.319	(15)	-	-	0.043	(9)
$Putamen_r$	0.051	(5)	0.166	(9)	0.307	(7)	0.050	(41)	0.267	(22)	-	-	0.043	(12)
$Thalamus_l$	0.039	(10)	0.315	(12)	0.125	(7)	0.059	(24)	0.198	(20)	-	-	0.040	(12)
$Thalamus_r$	0.039	(14)	0.366	(17)	0.106	(10)	0.039	(32)	0.194	(20)	-	-	0.051	(12)
$Pallidum_l$	0.021	(13)	0.072	(20)	0.289	(14)	0.334	(51)	-	-	-	-	0.016	(49)
$Pallidum_r$	0.040	(13)	0.126	(27)	0.319	(25)	0.219	(63)	0.084	(294)	-	-	0.025	(45)

Table 6.19: Subject 1866-Model 3

Also in this case, the precision is good for all the subjects and in particular the CVs relative to the macroparameter V_d are lower than the ones calculated with Model 1.

Lastly, we decided to test on the same subjects also another structure, Model 4, which has the same number and type of compartments of Model 3, but in this case the irreversible process is connected to the plasma activity curve and not to metabolites. While previously with all SA approaches and compartmental models we have found the evident presence of an irreversible component (except for 2241), with this model also subjects 1814 and 1866 do not present in the majority of ROIs the trapping process ($k_3 = 0$), in disagreement with the previous information that showed a marked irreversible binding and so in this case the data of three of the four subjects could be described by a reversible structure. However the values of the rate costant k_2 are very low, e.g for subject 1814 $k_2 = 0.009 \pm 0.004$ and for 1866 $k_2 = 0.007 \pm 0.004$. For subjects 1711 and 2241 the parameters that describe the exchanges between plasma and tissue are similar to the one found with Model 1 (as we have seen also for Model 3) and so, consequently, also the V_d for the tissue is nearly equal. Instead for the other two subjects the values with Model 4 for the tissue, especially k_6, are very different, e.g for 1814 with Model 4 we have $k_6 = 0.3 \pm 0.13$ while with Model 1 $k_6 = 0.52 \pm 0.27$. On average, the values of CVs for the parameters calculated with this model are significantly higher than the others found with the previous model, in fact as we can see in the following tables (6.20-23) in some cases they are over 100 $\div$200 %, especially for subjects 1814 and 1866, while previously this happens very rarely.

Also for this compartmental model we show the $V_d s$ values, divided into the three groups and as previously these values reflect the distribution of the receptors in the brain (Figure 6.12): Cerebellum is in the first two groups while the rich areas are all in the last one. Moreover the fits are able to explain the data in a good way, in particular they show the same goodness of Model 3; also the weighted residuals are consistent with the expected trends and so agree with a good estimation.

ROI	$K_5[ml ml^{-1} min^{-1}]$	cv	$k_6[min^{-1}]$	cv	$V_d[ml ml^{-1}]$	cv	$k_3[min^{-1}]$	cv	$k_1[min^{-1}]$	cv	$k_2[min^{-1}]$	cv	$V_b[unitless]$	cv
$Cerebellum_r$	0.032	(10)	0.483	(11)	0.065	(6)	0	-	0.256	(9)	0.010	(6)	0.032	(8)
$Cerebellum_l$	0.031	(10)	0.443	(6)	0.071	(6)	0	-	0.274	(10)	0.011	(6)	0.030	(8)
G cing ant_l	0.027	(21)	0.454	(24)	0.059	(13)	0	-	0.198	(15)	0.013	(10)	0.045	(13)
G cing ant_r	0.016	(667)	0.358	(4)	0.046	(668)	0	-	0.232	(16)	0.012	(12)	0.035	(48)
$CaudateNucl_l$	0.031	(14)	0.373	(17)	0.083	(10)	0	-	0.374	(19)	0.012	(11)	0.023	(17)
$CaudateNucl_r$	0.033	(14)	0.324	(18)	0.101	(11)	0	-	0.387	(25)	0.012	(15)	0.021	(23)
$NuclAccumb_l$	0.017	(55)	0.28	(72)	0.057	(47)	0.43	(61)	0.032	(145)	-	-	0.024	(52)
$NuclAccumb_r$	0.025	(8)	0.161	(22)	0.152	(246)	0	-	0.221	(43)	0.004	(90)	0.031	(22)
$Putamen_l$	0.039	(62)	0.258	(2)	0.152	(62)	0	-	0.282	(13)	0.011	(10)	0.032	(10)
$Putamen_r$	0.038	(9)	0.273	(15)	0.140	(13)	0.27	(17)	0.076	(20)	-	-	0.032	(13)
$Thalamus_l$	0.031	(319)	0.517	(2)	0.059	(318)	0	-	0.315	(13)	0.012	(8)	0.030	(33)
$Thalamus_r$	0.024	(13)	0.323	(16)	0.073	(9)	0	-	0.264	(14)	0.009	(12)	0.030	(12)
$Pallidum_l$	0.017	(59)	0.128	(66)	0.132	(42)	0	-	0.138	(91)	0.000	-	0.032	(86)
$Pallidum_r$	0.020	(320)	0.116	(105)	0.175	(394)	0.1	(100)	0.183	(110)	0.011	(516)	0.028	(68)

Table 6.20: Subject 1814-Model 4

ROI	$K_5[mlml^{-1}min^{-1}]$	cv	$k_6[min^{-1}]$	cv	$V_d[mlml^{-1}]$	cv	$k_3[min^{-1}]$	cv	$k_1[min^{-1}]$	cv	$k_2[min^{-1}]$	cv	$V_b[unitless]$	cv
$Cerebellum_r$	0.074	(4)	0.309	(7)	0.238	(6)	0.161	(11)	0.184	(12)	0.049	(17)	0.049	(6)
$Cerebellum_l$	0.074	(3)	0.317	(6)	0.233	(5)	0.171	(9)	0.203	(10)	0.052	(14)	0.047	(5)
G cing ant_l	0.058	(8)	0.292	(16)	0.199	(17)	0.105	(13)	0.215	(23)	0.067	(22)	0.064	(8)
G cing ant_r	0.056	(18)	0.325	(35)	0.174	(40)	0.117	(17)	0.261	(50)	0.089	(39)	0.064	(14)
$CaudateNucl_l$	0.078	(12)	0.249	(20)	0.312	(28)	0.226	(15)	0.414	(58)	0.089	(41)	0.040	(14)
$CaudateNucl_r$	0.078	(5)	0.202	(8)	0.384	(6)	-	-	0.340	(19)	0.024	(9)	0.033	(16)
$NuclAccumb_l$	0.072	(16)	0.235	(35)	0.309	(37)	0.185	(69)	0.353	(62)	0.049	(73)	0.038	(34)
$NuclAccumb_r$	0.073	(15)	0.197	(26)	0.371	(19)	0.000	-	0.271	(54)	0.027	(28)	0.039	(43)
$Putamen_l$	0.093	(6)	0.213	(14)	0.436	(16)	0.151	(22)	0.264	(37)	0.056	(38)	0.049	(12)
$Putamen_r$	0.095	(5)	0.200	(12)	0.476	(12)	0.084	(103)	0.316	(22)	0.036	(40)	0.039	(15)
$Thalamus_l$	0.078	(6)	0.233	(12)	0.335	(12)	0.001	(128)	0.200	(28)	0.021	(36)	0.055	(9)
$Thalamus_r$	0.081	(8)	0.280	(14)	0.289	(12)	0.155	(36)	0.157	(22)	0.039	(45)	0.053	(13)
$Pallidum_l$	0.062	(20)	0.173	(38)	0.360	(53)	0.166	(52)	0.784	(71)	0.060	(55)	0.026	(30)
$Pallidum_r$	0.055	(13)	0.145	(35)	0.383	(37)	-	-	0.509	(54)	0.040	(32)	0.032	(33)

Table 6.21: Subject 1711-Model 4

ROI	$K_5[ml ml^{-1} min^{-1}]$	cv	$k_6[min^{-1}]$	cv	$V_d[ml ml^{-1}]$	cv	$k_3[min^{-1}]$	cv	$k_1[min^{-1}]$	cv	$k_2[min^{-1}]$	cv	$V_b[unitless]$	cv
$Cerebellum_r$	0.036	(8)	0.232	(12)	0.156	(8)	0	-	0.127	(10)	0.035	(5)	0.098	(6)
$Cerebellum_l$	0.039	(5)	0.221	(9)	0.177	(6)	0	-	0.121	(8)	0.033	(5)	0.100	(5)
G cing ant_l	0.031	(14)	0.185	(22)	0.167	(16)	0	-	0.122	(19)	0.030	(12)	0.089	(12)
G cing ant_r	0.024	(15)	0.140	(31)	0.174	(29)	0	-	0.087	(21)	0.032	(17)	0.133	(8)
$CaudateNucl_l$	0.060	(12)	0.205	(16)	0.295	(10)	0	-	0.111	(26)	0.026	(15)	0.088	(17)
$CaudateNucl_r$	0.064	(15)	0.207	(20)	0.308	(13)	0	-	0.145	(43)	0.027	(22)	0.063	(32)
$NuclAccumb_l$	0.040	(17)	0.066	(22)	0.611	(13)	0	-	0.031	(34)	0.000	-	0.131	(27)
$NuclAccumb_r$	0.033	(20)	0.101	(42)	0.328	(24)	0	-	0.056	(55)	0.012	(80)	0.106	(24)
$Putamen_l$	0.081	(8)	0.200	(12)	0.406	(9)	0	-	0.124	(21)	0.034	(12)	0.104	(13)
$Putamen_r$	0.058	(17)	0.187	(33)	0.307	(44)	0.0440	(40)	0.095	(83)	0.058	(83)	0.114	(1)
$Thalamus_l$	0.043	(16)	0.283	(19)	0.152	(12)	0	-	0.106	(14)	0.032	(7)	0.121	(39)
$Thalamus_r$	0.048	(12)	0.220	(17)	0.220	(11)	0	-	0.125	(19)	0.026	(11)	0.089	(13)
$Pallidum_l$	0.053	(10)	0.121	(13)	0.438	(7)	0.0740	(30)	0.000	-	0.000	-	0.116	(17)
$Pallidum_r$	0.061	(17)	0.172	(26)	0.352	(18)	0	-	0.099	(44)	0.023	(30)	0.095	(29)

Table 6.22: Subject 2241-Model 4

ROI	$K_5[ml ml^{-1} min^{-1}]$	cv	$k_6[min^{-1}]$	cv	$V_d[ml ml^{-1}]$	cv	$k_3[min^{-1}]$	cv	$k_1[min^{-1}]$	cv	$k_2[min^{-1}]$	cv	$V_b[unitless]$	cv
$Cerebellum_r$	0.047	(6)	0.396	(7)	0.118	(4)	0	-	0.176	(7)	0.008	(7)	0.052	(6)
$Cerebellum_l$	0.045	(7)	0.391	(11)	0.116	(9)	0.054	(246)	0.129	(77)	0.006	(65)	0.052	(6)
G cing ant_l	0.034	(13)	0.334	(15)	0.103	(9)	0	-	0.213	(12)	0.009	(11)	0.049	(11)
G cing ant_r	0.034	(14)	0.372	(22)	0.093	(17)	0.139	(88)	0.031	(286)	0.003	(694)	0.070	(8)
$CaudateNucl_l$	0.058	(7)	0.199	(10)	0.293	(6)	0	-	0.357	(20)	0.010	(16)	0.032	(19)
$CaudateNucl_r$	0.054	(6)	0.232	(9)	0.235	(6)	0	-	0.371	(16)	0.012	(10)	0.031	(15)
$NuclAccumb_l$	0.035	(30)	0.235	(41)	0.149	(28)	0	-	0.223	(37)	0.015	(27)	0.054	(31)
$NuclAccumb_r$	0.050	(43)	0.540	(47)	0.093	(26)	0.793	(92)	0.046	(235)	0.000	-	0.016	(83)
$Putamen_l$	0.057	(4)	0.182	(6)	0.312	(5)	0	-	0.253	(11)	0.010	(11)	0.044	(9)
$Putamen_r$	0.053	(5)	0.157	(8)	0.338	(6)	0	-	0.243	(15)	0.008	(18)	0.043	(12)
$Thalamus_l$	0.040	(9)	0.286	(11)	0.139	(6)	0	-	0.205	(13)	0.007	(15)	0.040	(12)
$Thalamus_r$	0.039	(12)	0.320	(15)	0.121	(9)	0	-	0.183	(14)	0.008	(14)	0.052	(12)
$Pallidum_l$	0.021	(13)	0.073	(20)	0.288	(14)	0	-	0.334	(52)	0.000	-	0.016	(51)
$Pallidum_r$	0.041	(14)	0.128	(24)	0.318	(18)	0	-	0.289	(55)	0.002	(189)	0.025	(47)

Table 6.23: Subject 1866-Model 4

Subject 1814		Subject 1711		Subject 2241		Subject 1866	
G cing ant_r	0.0458	ParietalLob_l	0.1718	Ant TL med_r	0.0444	Hippocampus_l	0.0839
FrontalLobe_l	0.0534	G cing ant_r	0.1737	G paraH amb_r	0.0708	2.64 ParietalLob_l	0.09
Ant TL med_r	0.0542	Amygdala_l	0.1767	G occtem la_r	0.0825	1.17 G paraH amb_l	0.0914
G cing post_r	0.0547	ParietalLob_r	0.1808	FrontalLobe_r	0.1115	2.9 G cing ant_r	0.0925
FrontalLobe_r	0.0553	FrontalLobe_l	0.1824	ParietalLob_l	0.1157	0.42 NuclAccumb_r	0.0927
ParietalLob_l	0.056	Hippocampus_r	0.1864	G paraH amb_l	0.1175	0.18 G sup temp_r	0.0934
G occtem la_r	0.0561	OccipitLobe_l	0.1871	OccipitLobe_l	0.1187	0.12 G occtem la_l	0.0944
G occtem la_l	0.0572	FrontalLobe_r	0.1889	FrontalLobe_l	0.1202	0.15 ParietalLob_r	0.0959
Amygdala_r	0.0573	Hippocampus_l	0.1905	ParietalLob_r	0.1293	0.91 FrontalLobe_l	0.1011
G cing ant_l	0.0587	OccipitLobe_r	0.1934	Ant lat_r	0.1309	0.16 FrontalLobe_r	0.1018
Ant TL med_l	0.0589	G sup temp_r	0.1961	Hippocampus_r	0.1314	0.05 G cing ant_l	0.1027
ParietalLob_r	0.0591	G cing ant_l	0.1988	OccipitLobe_r	0.1345	0.31 G sup temp_l	0.1041
Thalamus_l	0.0594	G paraH amb_l	0.1995	G cing post_r	0.1394	0.49 OccipitLobe_r	0.1051
Ant lat_r	0.0595	PosteriorTL_l	0.2032	G occtem la_l	0.1419	0.25 Ant TL med_r	0.1083
G paraH amb_l	0.0602	G cing post_r	0.2092	G sup temp_r	0.1476	0.57 G paraH amb_r	0.1084
G paraH amb_r	0.0611	G tem midin_l	0.2106	Thalamus_l	0.1517	0.41 G cing post_l	0.1094
Hippocampus_r	0.0619	PosteriorTL_r	0.211	Ant lat_l	0.154	0.23 OccipitLobe_l	0.1111
G sup temp_l	0.0623	G sup temp_l	0.2121	PosteriorTL_r	0.1542	0.02 G tem midin_r	0.1124
Amygdala_l	0.0631	Ant lat_l	0.2175	Cerebellum_r	0.1561	0.19 Ant lat_l	0.1143

(a) Low values

OccipitLobe_l	0.0638	Ant TL med_l	0.2229	G sup temp_l	0.165	0.89 G cing post_r	0.1155
G tem midin_l	0.0641	Insula_l	0.2294	G tem midin_l	0.1651	0.01 Ant lat_r	0.1158
Insula_r	0.0649	Cerebellum_l	0.2331	G cing ant_l	0.1668	0.17 Cerebellum_l	0.1159
Cerebellum_r	0.0653	Cerebellum_r	0.2382	G tem midin_r	0.1697	0.29 G tem midin_l	0.117
Ant lat_l	0.0654	Ant TL med_r	0.2418	G cing ant_r	0.1739	0.42 Hippocampus_r	0.1172
NuclAccumb_l	0.0656	G cing post_l	0.242	PosteriorTL_l	0.176	0.21 Cerebellum_r	0.1178
G tem midin_r	0.0662	G paraH amb_r	0.2481	Cerebellum_l	0.177	0.1 PosteriorTL_r	0.1186
Hippocampus_l	0.0662	Ant lat_r	0.2491	G cing post_l	0.1775	0.05 Thalamus_r	0.1208
G sup temp_r	0.0673	G tem midin_r	0.2497	Hippocampus_l	0.1922	1.47 PosteriorTL_l	0.1216
OccipitLobe_r	0.0687	G occtem la_r	0.2513	Ant TL med_l	0.2073	1.51 Insula_l	0.1242
PosteriorTL_l	0.07	Thalamus_r	0.2891	Insula_l	0.2082	0.09 Amygdala_l	0.1257
Cerebellum_l	0.0705	G occtem la_l	0.2919	Amygdala_r	0.2085	0.03 Ant TL med_l	0.1274
G cing post_l	0.0726	Amygdala_r	0.3061	Thalamus_r	0.2198	1.13 G occtem la_r	0.1314
Thalamus_r	0.0726	NuclAccumb_l	0.3085	Insula_r	0.2239	0.41 Thalamus_l	0.1387
PosteriorTL_r	0.0739	CaudateNucl_l	0.3124	Amygdala_l	0.2573	3.34 NuclAccumb_l	0.1485
Insula_l	0.0743	Thalamus_l	0.3346	CaudateNucl_l	0.2947	3.74 Amygdala_r	0.1587
CaudateNucl_l	0.0831	Insula_r	0.3371	Putamen_r	0.3073	1.26 Insula_r	0.1651
CaudateNucl_r	0.1008	Pallidum_l	0.3601	CaudateNucl_r	0.3083	0.1 CaudateNucl_r	0.2346
Pallidum_l	0.1321	NuclAccumb_r	0.3711	NuclAccumb_r	0.3275	1.92 Pallidum_l	0.2883
Putamen_r	0.1402	Pallidum_r	0.3833	Pallidum_r	0.3515	2.4 CaudateNucl_l	0.2925
NuclAccumb_r	0.1521	CaudateNucl_r	0.3843	Putamen_l	0.4061	5.46 Putamen_l	0.3124
Putamen_l	0.1522	Putamen_l	0.4358	Pallidum_l	0.4381	3.2 Pallidum_r	0.3184
Pallidum_r	0.1747	Putamen_r	0.4756	NuclAccumb_l	0.6107	17.26 Putamen_r	0.3376

(b) Medium and high values

Figure 6.12: Distribution Volume V_d with Model 4

Comparison between Model 1, Model 3 and Model 4

After having rejected Model 2, we have still three different compartmental models which are all able to describe our data. We can not use the Akaike Information Criterion to choose the most parsimonious model since all the structures have the same number of parameters. Moreover also the analysis of the differences between the measured data and the descriptions provided by the three models can not help our choice. Model 3 and 4 are able to describe better all the parts of the curves, as we can see in Figure 6.13, and this is verified especially for subjects 1814 and 1866. However considering also the other subjects, the variances are not so marked and significant and so we can not use the fit as a criterion to choose the best model.

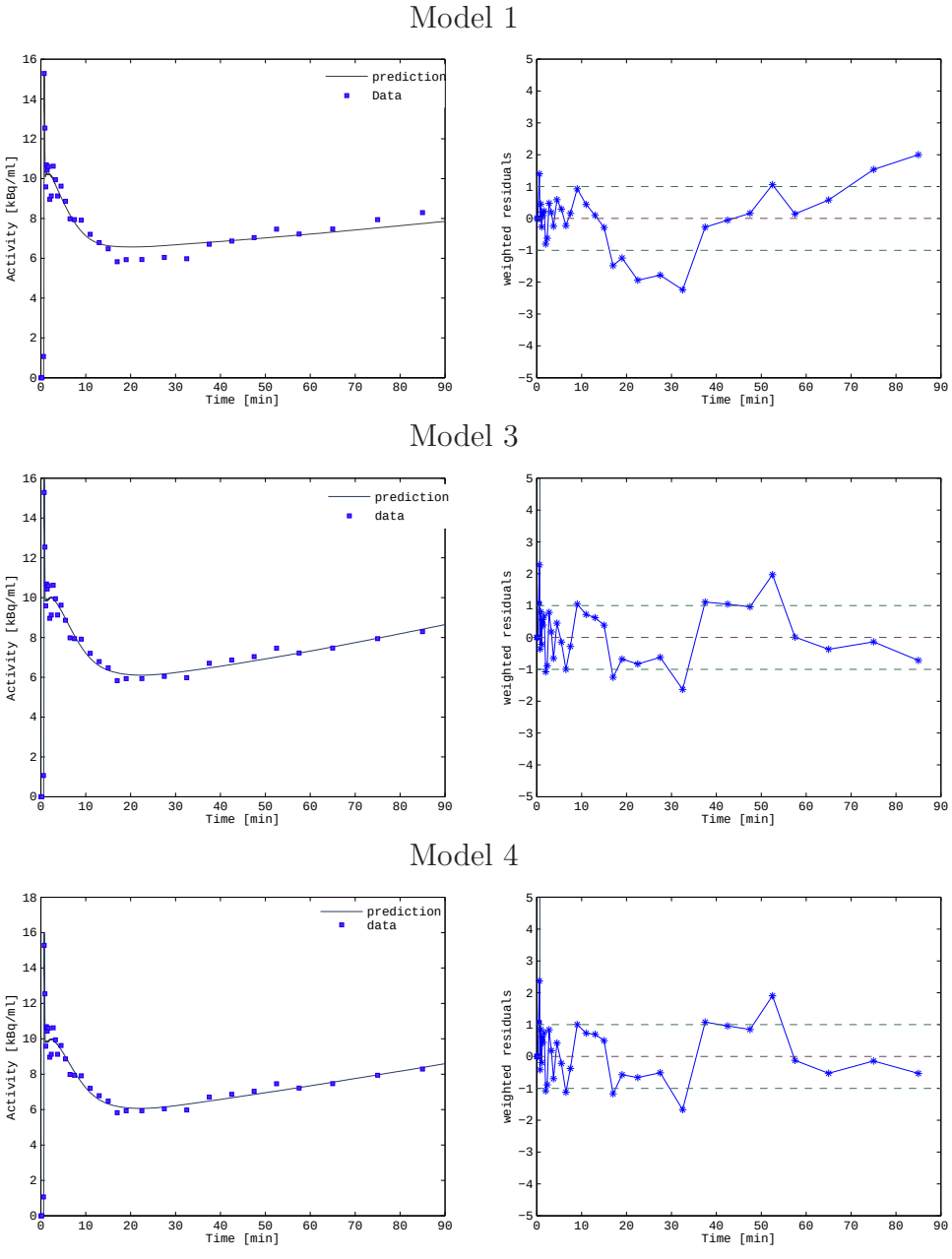

Figure 6.13: Fits and weighted residuals with the three models for subject 1814, ROI left Putamen

First of all, we decided to compare the values of the distribution volume obtained with the three models in each subject; from the observation of the previous tables it is clear that the precisions are good for all the estimated $V_d s$ and there are not important differences between the CVs. The values of $V_d s$ for subjects 1711 and 2241 are nearly equal through the models, while for 1814 and 1866 the

ones calculated with Model 1 are significantly lower than the others. However, as previously remarked, for all the three models the $V_d s$ correlate with the distribution of A_{2A} receptors within the brain: areas as Striatum or Globus Pallidus have always high values, as expected since they have a large number of receptors and so the tracer can distribute itself in the tissue. Instead the Anterior Cingulate Gyrus and Cerebellum have low $V_d s$, even if for the last one are not so low as expected; this is an index that here there are anyway some A_{2A} receptors and so the specific binding to the Cerebellum precludes its use as a reference region, in agreement with the results of Brooks and coworkers [14]. Since there are no evident differences between the $V_d s$ obtain with Model 1, 3 and 4 and they all correlate with the physiological information, we can not use this macroparameter as a criterion to choose the best one.

Lastly, we decided to compare for each subject the results of the compartmental model with its correspondent I/O model, in fact their numerical results have to be comparable and in agreement. We have to underline that the α and η values of the low components for the I/O models are given by the ratio between the estimates obtained via the nonnegative linear weighted least squares algorithm and the blood volume V_b, i.e interpreting the values in light of the model, which assumes that the components for $\beta = 0$ or $\beta \approx 0$ are due to the blood presence. The same assumption is made also for the alpha values of the traditional SA, i.e the low components are supposed due to blood and so divided for V_b and not for (1- V_b) as usual.

The first consideration that appears from the observation of the results of the SA approaches is that the I/O model with the double input function and accounting for the metabolites presence is characterised by a high intra-subject variability, e.g for subject 1814 there are regions like Nucleus Accumbens where all the spectral lines are due to the metabolic part, and others with only one or, in same cases, zero line connected to the $C_{tp}(t)$. Moreover there is a marked inter-subject variability, as previously seen, in fact for someone the component for $\beta \approx 0$ is due to metabolites (1711) while for others it is connected to parent plasma (1814) and all these variabilities are not physiologically acceptable. Also the comparison between the values of the parameters of Model 3 and 4 with this I/O model do

not give the wished results (we took subjects 1814 and 1711 as samples, Figure 6.14-15). For subject 1814, with Model 3 we have an acceptable agreement between the results of the tissue part, instead the values of k_3 do not correlate with the spectral lines due to metabolites and this mismatch is also present between k_1 and the α values connected to the $C_p(t)$. Also for subject 1711 there is a well correlation between the values relative to the tissue part, and in this case there is an acceptable agreement between the blood terms, even if the differences, e.g for Putamen, between k_3 and η values or the presence of $3 \div 4$ spectral lines due to metabolites (Cerebellum) are not physiological.

The same discrepancy is present also using Model 4, but in this case the results are worse since this compartmental structure do not identify the irreversible trapping of subjects 1814 and 1866, even if we know that this binding is present. For 1814 we have a good correlation between the results of the tissue part and the values concerning the metabolites, but in all the ROIs $k_3 = 0$ and so it is completely different from the α results of SA. Also for 1711 the comparison does not lead us to good results, in fact while the parameters of the compartmental models correlate well with α and β values for the tissue part, the values relative to blood are quite different (e.g this is particularly clear for Caudate Nucleus). Moreover for this subject the majority of the ROIs have the spectral line for $\beta = 0$ connected to the metabolites presence, while Model 4 supposes the trapping to be connected to the parent plasma.

In light of the significant inter/intra-subject variability for the SA approach with also metabolites and the mismatch between the results of the compartmental models and the I/O model we decide to reject Model 3 and Model 4, because, at present, these variations are not physiologically justifiable. In particular Model 4 has revealed to be worser than Model 3 for two of the four subjects, for its low precisions of the estimates for some subjects and its inability to detect the trapping component. Other studies are required to understand if and how the metabolites presence should be incorporeted in the structure of the compartmental model.

Finally, we compared the results of the traditional SA technique with the parameters provided by Model 1. In this case the comparisons are positive, since the

α and β values well correlate with the rate costants of the model, in fact as we can see in Figure 6.16 the values are quite similar and so there is an important agreement between these two complementary techniques. We also present in Figure 6.17-18, for subjects 1814 and 1866 as samples, the spectral lines detected with the traditional SA and the SA with double input function togheter with the values of the rate costants identified with these three models. This is a further graphical depict, it clearly shows that only Model 1 fulfills the expactations, while in the other two cases the model component are shifted or higher/lower in comparison with the values of the spectrum. We used one of the most important ROI (Putamen) and particularly evident is the absence of the irreversible component for Model 4 for this two subjects, that is one of the element that led us to reject this model.

For this reason and also for the good precision of the estimates, for the low differences between data and model estimated curves, for its agreement with the physiological information we decide to propose Model 1 as the most parsimonious compartmental model to describe the kinetics of [^{11}C]SCH442416 within the brain.

	Blood [*Cp(t)*]				Tissue				Blood [*Ctp(t)*]		
	alpha	beta	k_1	k_2	alpha	beta	K_5	k_6	eta	beta	k_3
Cerebellum_r	0.0210	0.0033	0.227	-	0.0017 0.0198 0.0206	0.3753 0.3871 1.6	0.032	0.534	0.286	0.0095	0.073
Cerebellum_l	0.0547	0.0032	0.255	-	0.0117 0.0121 0.0156	0.3753 0.3871 1.6	0.031	0.486	0.2743	0.0095	0.066
G_cing_ant_l	0.0911	0.0029	0.208	-	0.0033 0.0232	0.4579 0.4697	0.027	0.510	0.1342	0.0095	0.029
G_cing_ant_r	0.0651	0.0032	0.224	-	0.01 0.0049 0.0036	0.3399 0.3517 1.6	0.016	0.405	0.1916	0.0095	0.048
CaudateNucl_l	0.1191	0.0027	0.365	-	0.0212 0.0237	0.2927 1.6	0.031	0.409	0.3938	0.0095	0.078
CaudateNucl_r	0.1263	0.0029	0.377	-	0.0308 0.0045	0.3163 1.6	0.032	0.341	0.3482	0.0095	0.078
NuclAccumb_l	0.2365	0.0029	0.427	-	0.0169	0.2691	0.016	0.274	0.2207	0.0095	0.033
NuclAccumb_r	-	-	0.120	-	-	-	0.024	0.167	0.0362 0.1298 0.6889 0.0142 0.4856	0.0002 0.0002 0.1393 0.1511 0.6114	0.132
Putamen_l	0.0344	0.0032	0.261	-	0.0074 0.0285 0.0105	0.2337 0.2455 1.6	0.039	0.273	0.3026	0.0095	0.073
Putamen_r	-	-	0.275	-	0.0036 0.0294 0.0179	0.2337 0.2455 1.6	0.038	0.274	0.0819 0.0884 0.225	0 0.0095 0.0213	0.077
Thalamus_l	0.0915	0.0033	0.303	-	0.0059 0.0128 0.0236	0.3871 0.3989 1.6	0.031	0.586	0.3052	0.0095	0.068
Thalamus_r	-	-	0.211	-	0.0053 0.0111	0.2455 0.2573	0.023	0.358	0.2899 0.0237	0.008 0.008	0.097
Pallidum_l	-	-	-	-	0.0169	0.1275	0.017	0.129	0.1434	0	0.138
Pallidum_r	0.1160	0.0022	0.281	-	0.0156 0.0026 0.0154	0.1039 0.1157 1.6	0.019	0.121	0.2141	0.0095	0.032

(a) Subject 1814

	Blood [*Cp(t)*]				Tissue				Blood [*Ctp(t)*]		
	alpha	beta	k_1	k_2	alpha	beta	K_5	k_6	eta	beta	k_3
Cerebellum_r	0.1638	0.0000	0.377	0.024	0.0234 0.0429 0.022	0.2691 0.2809 1.6	0.071	0.327	0.0056 0.0058 0.2127	0 0.0331 0.0449	0.054
Cerebellum_l	-	-	0.407	0.025	0.0602 0.0108 0.0063	0.2691 0.4697 1.6	0.072	0.337	0.0467 0.0392 0.2428 0.0879	0 0.0331 0.0449 0.5051	0.058
G_cing_ant_l	0.0890	0.0449	0.375	0.036	0.025 0.0337	0.2809 0.2927	0.054	0.320	0.0331 0.2048	0 0.0567	0.043
G_cing_ant_r	0.1267 0.0062	0.0567	0.406	0.043	0.0518 0.0062	0.3163 0.328	0.055	0.346	0.0387 0.2167	0 0.0685	0.048
CaudateNucl_l	0.7775	0.0449	0.694	0.044	0.0331 0.0419	0.2573 0.2691	0.075	0.262	0.1 0.017	0 0.0567	0.089
CaudateNucl_r	0.6395	0.0095	0.619	0.009	0.0169 0.0548	0.2101 0.2219	0.071	0.223	0.036	0.0213	-
NuclAccumb_l	-	-	0.691	0.029	0.0315 0.0431	0.2219 0.2337	0.066	0.260	0.0532 0.4438 0.0253	0 0.0449 0.0567	0.078
NuclAccumb_r	0.4484 0.0926	0.0095 0.0213	0.502	0.011	0.0626 0.0031	0.2101 0.2219	0.066	0.218	-	-	-
Putamen_l	0.2334 0.2285 0.2374	0.0000 0.0331 0.0449	0.497	0.030	0.0321 0.0527	0.2219 0.2337	0.087	0.221	-	-	0.058
Putamen_r	0.4548 0.1469	0.0088 0.0088	0.563	0.017	0.0284 0.0198 0.0494	0.1039 0.2691 0.2809	0.089	0.208	-	-	0.032
Thalamus_l	0.3878	0.0081	0.370	0.008	0.0194 0.0535 0.0004	0.2573 0.2691 1.6	0.073	0.268	0.0083	0.0095	-
Thalamus_r	0.0061 0.2869	0.0036 0.0036	0.343	0.018	0.0792	0.2927	0.078	0.292	0.1115	0.0567	0.046
Pallidum_l	1.2300 0.7296	0.0331 0.0449	1.410	0.038	0.0178 0.0293	0.1747 0.1865	0.051	0.195	0.1337 0.7916	0 1.6	0.098
Pallidum_r	0.3293 1.0686	0.0095 0.0213	0.853	0.017	0.0406 0.0365	0.1393 1.6	0.047	0.155	-	-	-

(b) Subject 1711

Figure 6.14: Comparison between the numerical results of Model 3 and the I/O model with $C_p(t)$ and $C_{tp}(t)$

	Blood [*Cp(t)*]			Tissue				Blood [*Ctp(t)*]			
	alpha	beta	k_3	alpha	beta	K_5	k_6	eta	beta	k_1	k_2
Cerebellum_r	0.0210	0.0033	0	0.0017 0.0198 0.0206	0.3753 0.3871 1.6	0.0315	0.4825	0.286	0.0095	0.2564	0.0103
Cerebellum_l	0.0547	0.0032	0	0.0117 0.0121 0.0156	0.3753 0.3871 1.6	0.0312	0.4428	0.2743	0.0095	0.2739	0.0111
G_cing_ant_l	0.0911	0.0029	0	0.0033 0.0232	0.4579 0.4697	0.0266	0.4539	0.1342	0.0095	0.1984	0.0133
G_cing_ant_r	0.0651	0.0032	0	0.01 0.0049 0.0036	0.3399 0.3517 1.6	0.0164	0.3583	0.1916	0.0095	0.232	0.0119
CaudateNucl_l	0.1191	0.0027	0	0.0212 0.0237	0.2927 1.6	0.031	0.3728	0.3938	0.0095	0.3743	0.0118
CaudateNucl_r	0.1263	0.0029	0	0.0308 0.0045	0.3163 1.6	0.0326	0.3238	0.3482	0.0095	0.3869	0.0119
NuclAccumb_l	0.2365	0.0029	0	0.0169	0.2691	0.0171	0.2606	0.2207	0.0095	0.3137	0.0139
NuclAccumb_r	-	-	0	-	-	0.0245	0.1611	0.0362 0.1298 0.6889 0.0142 0.4856	0.0002 0.0002 0.1393 0.1511 0.6114	0.2209	0.0044
Putamen_l	0.0344	0.0032	0	0.0074 0.0285 0.0105	0.2337 0.2455 1.6	0.0393	0.258	0.3026	0.0095	0.2824	0.0105
Putamen_r	-	-	0	0.0036 0.0294 0.0179	0.2337 0.2455 1.6	0.0383	0.2729	0.0819 0.0884 0.225	0 0.0095 0.0213	0.085	0.001
Thalamus_l	0.0915	0.0033	0	0.0059 0.0128 0.0236	0.3871 0.3989 1.6	0.0307	0.5172	0.3052	0.0095	0.3152	0.0118
Thalamus_r	-	-	0	0.0053 0.0111	0.2455 0.2573	0.0235	0.323	0.2899 0.0237	0.008 0.008	0.2643	0.0085
Pallidum_l	-	-	0	0.0169	0.1275	0.0169	0.1281	0.1434	0	0.1376	0
Pallidum_r	0.1160	0.0022	0	0.0156 0.0026 0.0154	0.1039 0.1157 1.6	0.0202	0.1156	0.2141	0.0095	0.1825	0.0112

(a) Subject 1814

	Blood [*Cp(t)*]			Tissue				Blood [*Ctp(t)*]			
	alpha	beta	k_3	alpha	beta	K_5	k_6	eta	beta	k_1	k_2
Cerebellum_r	0.1638	0.0000	0.1613	0.0234 0.0429 0.022	0.2691 0.2809 1.6	0.0737	0.3092	0.0056 0.0058 0.2127	0 0.0331 0.0449	0.1842	0.049
Cerebellum_l	-	-	0.1713	0.0602 0.0108 0.0063	0.2691 0.4697 1.6	0.074	0.3174	0.0467 0.0392 0.2428 0.0879	0 0.0331 0.0449 0.5051	0.2025	0.0516
G_cing_ant_l	0.0890	0.0449	0.1054	0.025 0.0337	0.2809 0.2927	0.058	0.2916	0.0331 0.2048	0 0.0567	0.2146	0.0671
G_cing_ant_r	0.1267	0.0567	0.1169	0.0518 0.0062	0.3163 0.328	0.0564	0.3248	0.0387 0.2167	0 0.0685	0.2608	0.0893
CaudateNucl_l	0.7775	0.0449	0.2255	0.0331 0.0419	0.2573 0.2691	0.0779	0.2493	0.1 0.017	0 0.0567	0.4138	0.0894
CaudateNucl_r	0.6395	0.0095	0	0.0169 0.0548	0.2101 0.2219	0.0776	0.202	0.036	0.0213	0.3395	0.0241
NuclAccumb_l	-	-	0.1849	0.0315 0.0431	0.2219 0.2337	0.0724	0.2347	0.0532 0.4438 0.0253	0 0.0449 0.0567	0.3528	0.0489
NuclAccumb_r	0.4484 0.0926	0.0095 0.0213	0	0.0626 0.0031	0.2101 0.2219	0.073	0.1968	-	-	0.2706	0.0265
Putamen_l	0.2334 0.2285 0.2374	0.0000 0.0331 0.0449	0.1512	0.0321 0.0527	0.2219 0.2337	0.0926	0.2126	-	-	0.264	0.0562
Putamen_r	0.4548 0.1469	0.0088 0.0088	0.0837	0.0284 0.0198 0.0494	0.1039 0.2691 0.2809	0.095	0.1999	-	-	0.3155	0.0363
Thalamus_l	0.3878	0.0081	0.001	0.0194 0.0535 0.0004	0.2573 0.2691 1.6	0.078	0.2332	0.0083	0.0095	0.1996	0.0212
Thalamus_r	0.0061 0.2869	0.0036 0.0036	0.1548	0.0792	0.2927	0.0809	0.28	0.1115	0.0567	0.1572	0.0388
Pallidum_l	1.2300 0.7296	0.0331 0.0449	0.1655	0.0178 0.0293	0.1747 0.1865	0.0624	0.1734	0.1337 0.7916	0 1.6	0.7838	0.0596
Pallidum_r	0.3293 1.0686	0.0095 0.0213	0	0.0406 0.0365	0.1393 1.6	0.0554	0.1447	-	-	0.5091	0.04

(b) Subject 1711

Figure 6.15: Comparison between the numerical results of Model 4 and the I/O model with $C_p(t)$ and $C_{tp}(t)$

	Blood (Reversible)				Tissue (Reversible)				Blood (Irreversible)		
	alpha	beta	k_1	k_2	alpha	beta	K_5	k_6	alpha	beta	k_3
Cerebellum_r	-	-	-	-	0.0291 0.0116	0.8238 1.6	0.0382	0.9039	0.474	0	0.4140
Cerebellum_l	-	-	-	-	0.0164 0.0152 0.0051	0.7058 0.7176 1.6	0.0355	0.7482	0.4768	0	0.4229
G_cing_ant_l	-	-	-	-	0.0141 0.0142	0.6822 0.694	0.0283	0.6861	0.2947	0	0.2777
G_cing_ant_r	-	-	-	-	0.018	0.7176	0.0180	0.7175	0.3605	0	0.3407
CaudateNucl_l	-	-	-	-	0.0137 0.0123 0.0145	0.5169 0.5288 1.6	0.0346	0.5980	0.7081	0	0.5694
CaudateNucl_r	-	-	-	-	0.0121 0.0206	0.4343 0.4461	0.0330	0.4452	0.6535	0	0.5688
NuclAccumb_l	-	-	-	-	0.0032 0.0116	0.3045 0.3163	0.0146	0.3082	0.5325	0	0.4931
NuclAccumb_r	-	-	-	-	0.0016 0.0247	0.3517 0.3635	0.0267	0.3682	0.5081	0	0.4664
Putamen_l	-	-	-	-	0.0045 0.036	0.3635 0.3753	0.0405	0.3720	0.4966	0	0.4425
Putamen_r	-	-	-	-	0.0162 0.0214 0.0062	0.3635 0.3753 1.6	0.0402	0.3822	0.5424	0	0.4660
Thalamus_l	-	-	-	-	0.0219 0.0202	0.812 1.6	0.0382	0.9714	0.5714	0	0.4862
Thalamus_r	-	-	-	-	0.0009 0.0193 0.0129	0.6468 0.6586 1.6	0.0290	0.7585	0.5311	0	0.4610
Pallidum_l	-	-	-	-	0.0112 0.004	0.2337 1.6	0.0120	0.2408	0.3051	0	0.2827
Pallidum_r	-	-	-	-	0.0163 0.0151	0.1275 1.6	0.0183	0.1353	0.4438	0	0.3550

(a) Subject 1814

	Blood (Reversible)				Tissue (Reversible)				Blood (Irreversible)		
	alpha	beta	k_1	k_2	alpha	beta	K_5	k_6	alpha	beta	k_3
Cerebellum_r	0.1412 0.1713	0.0213 0.0331	0.2651	0.0292	0.0295 0.0345 0.0182	0.3045 0.3163 1.6	0.0709	0.3384	0.2286	0	0.2015
Cerebellum_l	0.0438 0.2850	0.0213 0.0331	0.2889	0.0312	0.0426 0.0271 0.0034	0.3399 0.3517 1.6	0.0712	0.3476	0.2392	0	0.2150
G_cing_ant_l	0.0186 0.3100	0.0331 0.0449	0.3010	0.0430	0.0111 0.0418	0.3281 0.3399	0.0530	0.3306	0.1565	0	0.1462
G_cing_ant_r	0.0049 0.3689	0.0449 0.0567	0.3459	0.0560	0.0525	0.3753	0.0526	0.3713	0.1683	0	0.1576
CaudateNucl_l	0.5319 0.1551	0.0567 0.0685	0.6085	0.0599	0.0411 0.0301	0.2691 0.2809	0.0711	0.2757	0.331	0	0.2919
CaudateNucl_r	0.3728 0.3366	0.0094 0.0095	0.6184	0.0094	0.0711	0.2219	0.0711	0.2224	-	-	-
NuclAccumb_l	0.6066	0.0331	0.5228	0.0319	0.0359 0.0293	0.2573 0.2691	0.0654	0.2582	0.3093	0	0.2688
NuclAccumb_r	0.4484 0.0926	0.0095 0.0213	0.4973	0.0113	0.0626 0.0031	0.2101 0.2219	0.0660	0.2155	-	-	-
Putamen_l	0.2285 0.2374	0.0331 0.0449	0.4046	0.0381	0.0321 0.0527	0.2219 0.2337	0.0853	0.2276	0.2334	0.0000	0.2093
Putamen_r	-	-	0.4857	0.0207	0.0284 0.0198 0.0494	0.1039 0.2691 0.2809	0.0882	0.2129	0.4548 0.1469	0.0088 0.0088	0.1543
Thalamus_l	-	-	0.3697	0.0076	0.0072 0.0656	0.2573 0.2691	0.0728	0.2678	0.1872 0.2152	0.0076 0.0077	-
Thalamus_r	0.1672	0.0331	0.2326	0.0203	0.0073 0.07	0.2927 0.3045	0.0776	0.2986	0.2754 0.0303	0.003 0.0031	0.1845
Pallidum_l	0.2217 1.5936	0.0331 0.0449	1.2681	0.0427	0.0442 0.0176	0.1865 1.6	0.0485	0.1992	0.4781	0	0.3345
Pallidum_r	0.3293 1.0686	0.0095 0.0213	0.8511	0.0173	0.0406 0.0365	0.1393 1.6	0.0473	0.1542	-	-	-

(b) Subject 1711

Figure 6.16: Comparison between the numerical results of Model 1 and the I/O model with $C_p(t)$ and $C_{tp}(t)$

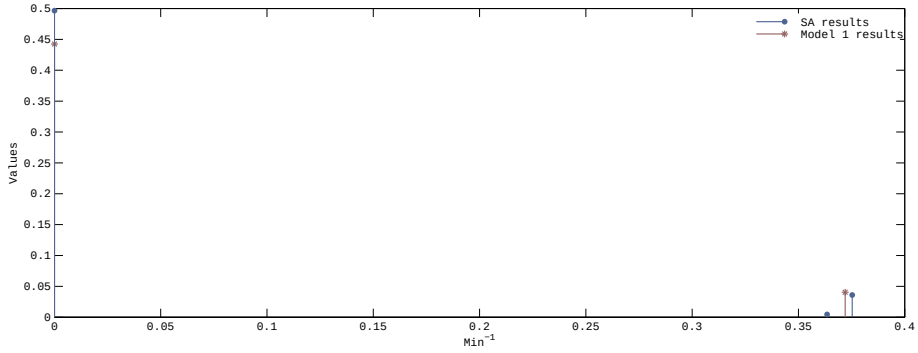

(a) Model 1

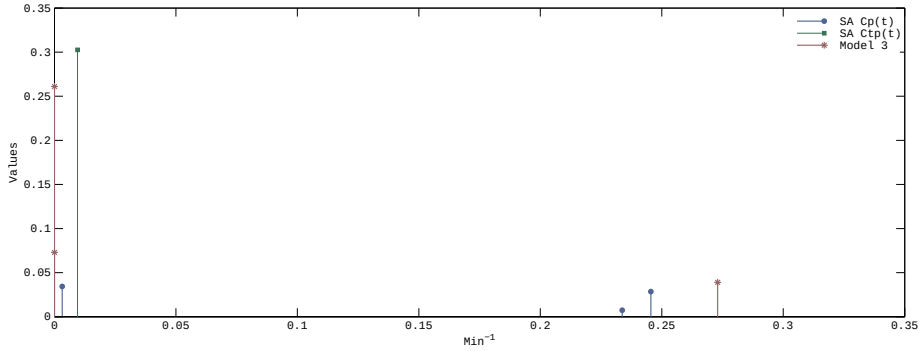

(b) Model 3

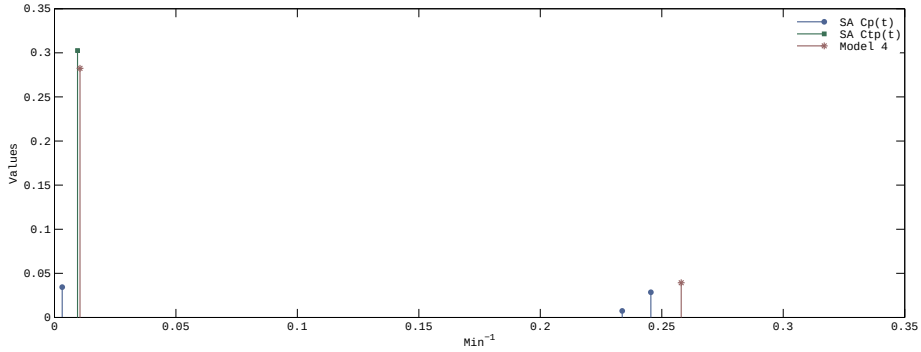

(c) Model 4

Figure 6.17: Comparison for subject 1814 between the spectral lines and the values of the compartmental model, relative to Putamen$_l$

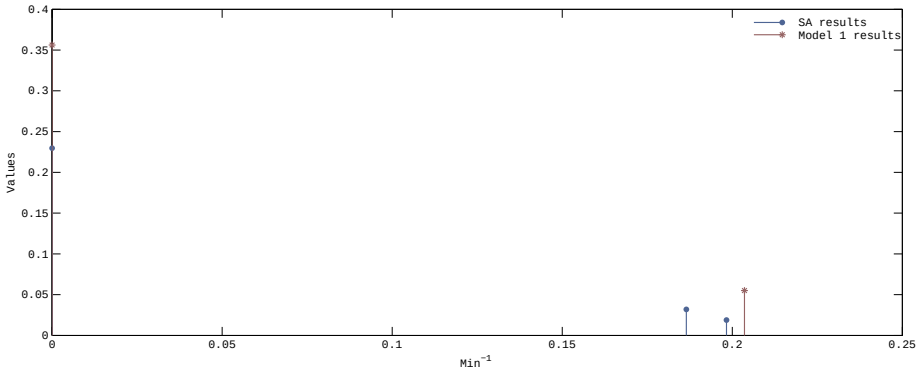

(a) Model 1

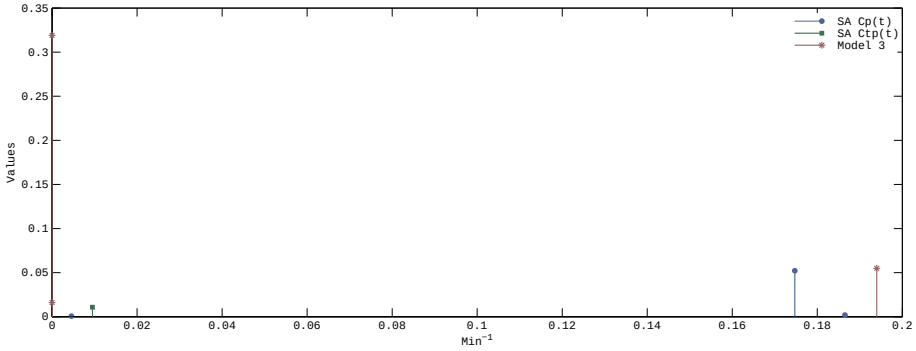

(b) Model 3

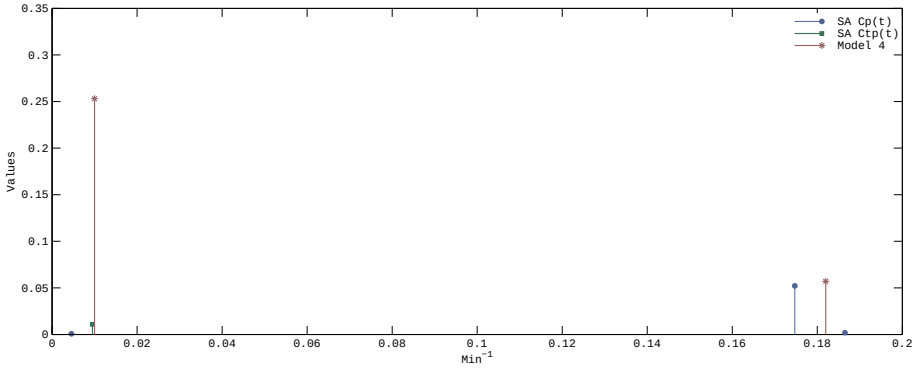

(c) Model 4

Figure 6.18: Comparison for subject 1866 between the spectral lines and the values of the compartmental model, relative to Putamen$_l$

Chapter 7

Discussion

In the previous chapter we have presented the results found with the I/O and compartmental models and, after the evaluation of the numerical values and of the main characteristics of each, we decided to propose Model 1 as the best one to describe the binding of [^{11}C]SCH442416 to neuroreceptor sites in the brain.
In fact the traditional compartmental models normally used in this type of studies are not able to well describe our data but in particular they are no physiologically justifiable. Among the innovative structures, Model 2 presents for the macroparameter V_d a too high inter/intra-subject variability which is not acceptable; moreover we can not accept Model 3 and 4, even if they give very good fits and trends of the residuals and their $V_d s$ are correlated with the physical distribution of the receptors in the brain areas, because, at present, their results are not in agreement with the corrispondent I/O model. In turn, this noncompartmental approach does not present a common trend but on the contrary we find a marked variability among the regions of a same subject, and this is one of the elements that leds us to reject the compartmental models 3 and 4.
So in this chapter we wish to analyze better the results obtained with Model 1, also to find potential correlations between the subjects.

Distribution Volume V_d in the tissue

In Figure 6.9 we have showed the different values found for four of the six subjects: it is of note that the V_d values obtained by using the parameters of the tissue pool are very low in comparison with other brain tracers, even if they are in line with

the ones found by Brooks and coworkers, which are in the range $0.3 \div 0.6$ $[ml ml^{-1}]$ (even if they consider healthy volunteers). In that figure, the values are divided into 3 groups and it is clear that they are correlated with the localization of the A_{2A} receptor subtype, in particular the Anterior Cingulate Gyrus has revealed to be particularly poor of receptors (in fact for all the subjects its V_d is in the first positions), while Putamen and Caudate Nucleus have confirmed to be the areas with the highest number of A_{2A} sites. To make the division into groups, we chose subject 2241, who presented a good range of values, and then we reported the same thresholds also for the other subjects. However, among the $V_d s$ of the first two groups, especially for subjects 1814 and 1866, there is not a marked variability and so probably we could divide all the values into only two groups, one with low-normal values and a second with the highest values. In Figure 7.2 we show all the sorted macroparameters V_d: it is evident the low differences, for the majority of subjects, between the first and the second group, while in the last part higher peaks are reached. In the x-axis we show only the increasing number of ROIs, but we report the correspondance between the number and the specific ROI name in the following table (Figure 7.1).

From the analysis of the numerical $V_d s$, subject 1711 seems to have the highest values, this is not completely true, in fact the starting point is higher in comparison with the other subjects (0.13 against 0.04) and so, consequently, all the values turn out to be increased. Instead, if we make for each subject a sort of normalization, i.e we divide every V_d value for the lowest one, we have more comparable values for the macroparameter and it appears that 1711 has lower values than the other three subjects. Moreover, it is particular evident with this normalization, especially for 1814, 1866 and 1711, the quite equal values among the majority of the ROIs, only from ROI number $37 \div 38$ there is a significant increase of the V_d, confirming that these receptors are selectively distributed and the values for the V_d calculated with Model 1 are correlated with these information. Finally, it is a further proof of the selectivity of [^{11}C]SCH442416, even if the low values for this macroparameter suggests a reduced distribution of the tracer through the BBB within the tissue.

n° ROI	Subject			
	1814	1711	2241	1866
1	G cing ant_r	Amygdala_l	Ant TL med_r	Hippocampus_l
2	Pallidum_l	G cing ant_r	G paraH amb_r	ParietalLob_l
3	G paraH amb_r	Hippocampus_r	G occtem la_r	G sup temp_r
4	Hippocampus_r	ParietalLob_l	G paraH amb_l	G paraH amb_l
5	G occtem la_l	Hippocampus_l	FrontalLobe_r	ParietalLob_r
6	G paraH amb_l	FrontalLobe_l	Ant lat_r	FrontalLobe_r
7	G occtem la_r	ParietalLob_r	FrontalLobe_l	G cing ant_l
8	G cing post_r	FrontalLobe_r	ParietalLob_l	FrontalLobe_l
9	Insula_r	G paraH amb_l	Ant lat_l	G occtem la_l
10	FrontalLobe_l	G sup temp_r	G occtem la_l	G occtem la_r
11	Ant TL med_l	G cing ant_l	OccipitLobe_l	G sup temp_l
12	FrontalLobe_r	OccipitLobe_l	ParietalLob_r	G cing ant_r
13	Amygdala_r	OccipitLobe_r	G tem midin_r	Ant TL med_r
14	ParietalLob_l	PosteriorTL_l	Hippocampus_r	OccipitLobe_r
15	Ant TL med_r	Ant lat_l	OccipitLobe_r	G tem midin_r
16	Thalamus_r	Ant TL med_l	G cing post_r	Amygdala_r
17	Hippocampus_l	G tem midin_l	Thalamus_l	G tem midin_l
18	G sup temp_l	PosteriorTL_r	G sup temp_r	Ant lat_r
19	Ant lat_r	G cing post_r	G cing ant_r	G paraH amb_r
20	Thalamus_l	G paraH amb_r	G cing ant_l	NuclAccumb_r
21	G cing ant_l	G sup temp_l	Cerebellum_r	Cerebellum_l
22	ParietalLob_r	Insula_l	PosteriorTL_r	Cerebellum_r
23	Cerebellum_r	Ant TL med_r	G sup temp_l	PosteriorTL_r
24	Amygdala_l	G occtem la_r	G tem midin_l	Thalamus_r
25	G tem midin_l	G cing post_l	G cing post_l	G cing post_r
26	Ant lat_l	Ant lat_r	Cerebellum_l	G cing post_l
27	G tem midin_r	G tem midin_r	PosteriorTL_l	Amygdala_l
28	OccipitLobe_l	Cerebellum_l	Ant TL med_l	Insula_l
29	G sup temp_r	Cerebellum_r	Hippocampus_l	OccipitLobe_l
30	Insula_l	Amygdala_r	Insula_r	Hippocampus_r
31	PosteriorTL_l	Pallidum_l	Amygdala_r	PosteriorTL_l
32	G cing post_l	G occtem la_l	Thalamus_r	Ant lat_l
33	Cerebellum_l	NuclAccumb_l	Insula_l	Ant TL med_l
34	NuclAccumb_l	CaudateNucl_l	Amygdala_l	Thalamus_l
35	PosteriorTL_r	Thalamus_r	NuclAccumb_r	Insula_r
36	OccipitLobe_r	Thalamus_l	CaudateNucl_l	NuclAccumb_l
37	CaudateNucl_l	Insula_r	Putamen_r	Pallidum_l
38	NuclAccumb_r	NuclAccumb_r	CaudateNucl_r	CaudateNucl_r
39	CaudateNucl_r	Pallidum_r	Pallidum_r	Pallidum_r
40	Putamen_r	CaudateNucl_r	NuclAccumb_l	CaudateNucl_l
41	Putamen_l	Putamen_l	Putamen_l	Putamen_r
42	Pallidum_r	Putamen_r	Pallidum_l	Putamen_l

Figure 7.1: Corrispondence between increasing number of x-axis and the name of the specific ROI

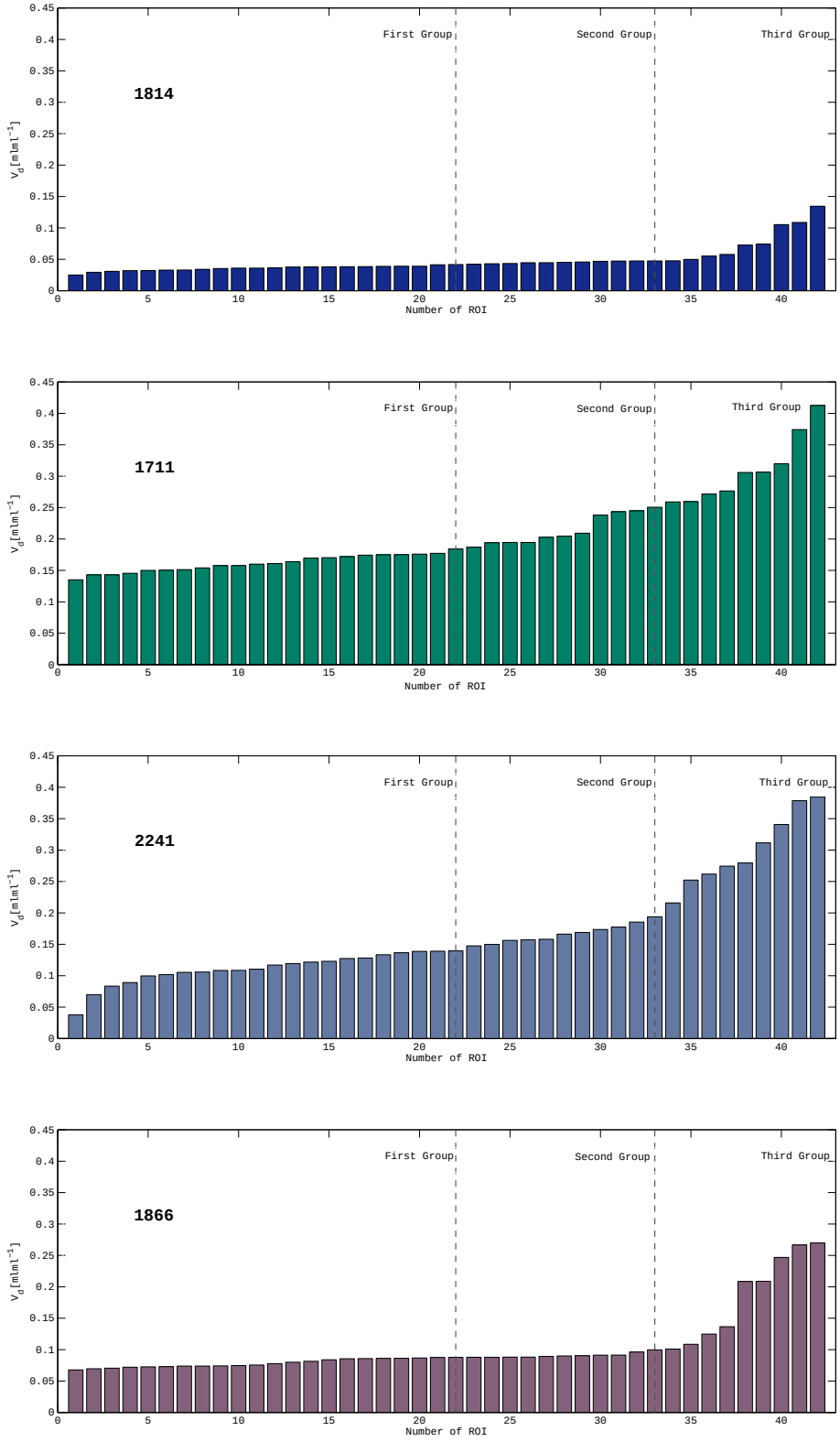

Figure 7.2: Sorted V_d values for each subject, obtained with Model 1 ($V_d = \frac{K_5}{k_6}$ $[ml ml^{-1}]$)

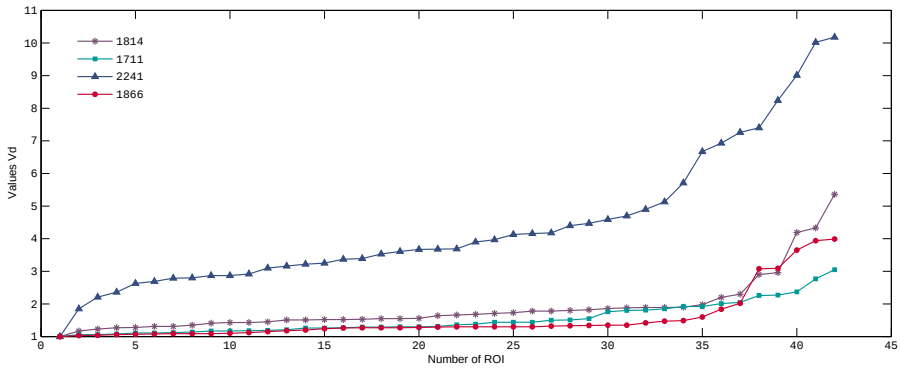

Figure 7.3: Sorted V_d values after the normalization

From the physiological information, we know that only low levels of A_{2A} receptors are present in Thalamus and in fact previous studies with other specific tracer for this subtype have demonstrated low binding in this cerebral area: so it is expected to have low V_d values. This consideration is followed by three subjects, 1814, 2241 and 1866 (all with Parkinson's desease and Dyskinesia), while 1711 presents values which are similar to the one found for the enriched areas like Caudate Nucleus and Nucleus Accumbens and, anyway, higher than the Vd calculated with Model 1 for the other three subjects. Thalamus is involved in the process of development of involuntary movements snd so it is interesting to understand if this result is reliable or less but, since we have only one Parkinson's desease subject and no healthy control, other studies, which involve a large number of patients, are required to find possible correlations regarding this motor area.

A recent study by Calon and his coworkers [20], involving a larger number of patients and another type of specific tracer for the same receptors, has demonstrated that the A_{2A} levels were increased in the Putamen of dyskinetic patients compared with both controls and non-dyskinetic patients. Also the Globus Pallidus revealed a higher specific binding in Parkinson's desease subjects compared with controls. We tried to notice if these observations were confirmed also for our tracer and patients, but since subjects 2300 (control) and 1804 (PD) were not reliable, we could not include them in the analysis and so we had only three dyskinetic and one no-dyskinetic patients, consequently the comparisons were

very limited. Taking this reducted number into account, if we use the numerical V_d values like so calculated with Model 1 and reported in Figure 6.9, we don't find the same consideration about the Putamen with our data. In fact, if there is a larger number of receptors in this area, a higher V_d is expected for dyskinetic subjects, while here 1711 seems to have the highest values. However, if we use the normalized values (as previously explained), we find that actually dyskinetic patients have higher values of V_d in the Putamen than the non-dyskinetic one.

Blood Parameters

In the previous chapter and in the first part of this one, we have considered for Model 1 the distribution volume V_d within the tissue, but it can be defined also for the vascular part. In particular, in relation to blood we have two different macroparameters, i.e

* Distribution Volume within the vasculature $V_{dblood} = \frac{k_1}{k_2}$: it describes the concentration of the tracer in the blood; this parameter can be defined only for the subjects who accept the reversible compartment in Model 1;

* Net Uptake Rate Costant $K = k_3$: it describes the rapidity of trapping of the tracer, present in the blood vessels, due to the receptors on the endothelial cells or platelets.

We decided to calculate these parameters for all the four subjects, in order to find possible connections between the dyskinetic and no-dyskinetic patients. We do not expect a too high intra-subject variability among the different ROIs, since the vasculature should be the same in all the regions and also the number of A_{2A} receptors, correlated to blood, should not change in relation to the particular region (contrarily to receptors within the tissue).

	K $[min^{-1}]$				$\mathbf{V}_{dblood}$ $[mlml^{-1}]$				**Vb** $[unitless]$			
	1814	1711	2241	1866	1814	1711	2241	1866	1814	1711	2241	1866
ROI Cerebellum$_r$	0.4140	0.2015	-	0.3020	-	9.0770	22.122	-	0.0287	0.0486	0.0983	0.0451
ROI Cerebellum$_l$	0.4229	0.215	-	0.2981	-	9.2732	24.727	-	0.0280	0.0464	0.1033	0.0454
ROI G cing ant$_l$	0.277	0.1462	-	0.3239	-	7.0007	28.905	-	0.0436	0.0639	0.0887	0.0449
ROI G cing ant$_r$	0.34	0.1576	0.0471	0.2064	-	6.1803	5.8282	-	0.03	0.0637	0.1331	0.0660
ROI CaudateNucl$_l$	0.5694	0.2919	-	0.5200	-	10.155	35.7873	-	0.0213	0.0401	0.0866	0.0305
ROI CaudateNucl$_r$	0.5688	-	-	0.4890	-	65.784	42.8982	-	0.0203	0.0329	0.0624	0.0303
ROI NuclAccumb$_l$	0.4931	0.2688	0.1056	0.2446	-	16.392	-	-	0.0243	0.0377	0.1249	0.0561
ROI NuclAccumb$_r$	0.4664	-	0.1068	0.9811	-	44.0434	-	-	0.0270	0.0388	0.1048	0.0144
ROI Putamen$_l$	0.4425	0.2093	-	0.3562	-	10.628	22.592	-	0.0305	0.0492	0.1031	0.0429
ROI Putamen$_r$	0.4660	0.1543	0.0819	0.3861	-	23.4969	2.4181	-	0.0302	0.0386	0.1129	0.0412
ROI Thalamus$_l$	0.4862	-	-	0.3489	-	48.4495	22.368	-	0.0268	0.0542	0.121	0.0363
ROI Thalamus$_r$	0.4610	0.1845	-	0.2905	-	11.439	38.865	-	0.0266	0.0523	0.0878	0.0475
ROI Pallidum$_l$	0.2827	0.3345	0.1109	0.7412	-	29.7331	-	-	0.0331	0.0259	0.1117	0.0159
ROI Pallidum$_r$	0.3550	-	-	0.5848	-	49.1965	42.650	-	0.0278	0.0316	0.0947	0.0236

Table 7.1: Values of the blood parameters with Model 1

From the analysis of the results reported in the previous table 7.1, it appears that 1814 and 1866, both dyskinetic patients, have a similar pattern, while 1711 and 2241, in turn, seem to have similar characteristics, even if they have a different diagnosis. About the blood volume V_b, as previously noticed, there is a fairly homogeneous distribution, without significant differences, and subject 2241 presents the higher values in comparison with the others. The distribution volume within blood V_{dblood} is defined only for subjects 1711 and 2241, since the others do not present the reversible blood compartment: this macroparameter, contrarily to the distribution volume within the tissue which is in the range $[0.2 \div 0.4 ml ml^{-1}]$, reaches high values. In particular, if we consider the average, Caudate Nucleus and Thalamus have the same results while for the other regions there are different behaviours , e.g in Nucleus Accumbens for subject 1711 we find $V_{dblood} = 30$ while for 2241 $V_{dblood} = 0$. Moreover V_{dblood} is not correlated with the blood volume term: we expect that ROIs with a relative high V_b value, that indicates the significant presence of blood, have also a high V_{dblood} but this is not verified in our subjects.

There is so a marked intra-subject variability in these ill patients, that we don't expect . Instead, for both patients, there is a correlation between V_{dblood} and K: when $k_3 = 0$, V_{dblood} is high and vice versa, in particular this is evident, also after making the average between the two parts, for subject 2241 whose ROIs with

$K = 0$ are Caudate Nucleus, Thalamus and Cerebellum. Instead for subjects 1711 there are marked differencies between the left and the right side and only some parts have $K = 0$, e.g the right parts of Caudate Nucleus and Nucleus Accumbens. Lastly, 1814 and 1866 have for all the regions $V_{dblood} = 0$: other studies are necessary to understand why the reversible component is not present in all the subjects and all the ROIs.

About the parameter K, from its definition it is clear that its values don't depend on the number of receptors present in a specific ROI and in fact, as we can see in the next figures, it is not correlated with the A_{2A} distribution within the brain. Subjects 1814 and 1866, as expected since they do not present the blood distribution volume, have the highest values while the others present significant lower Ks, especially 2241, who does not present in many ROIs the irreversible trapping, even if we can notice that Nucleus Accumbens has, in all the three dyskinetic patients, high values. Finally, it appears that, except for subject 1814 and contrary to our expectations, this parameter changes in a significant way among the ROIs of a same subject, as it already happened for V_{dblood} for subjects 1711 and 2241.

Other general considerations on Model 1

After having evaluated the micro/macro parameters relative to the tissue and blood compartment, we finally decided to compare some concentration curves. First of all, we considered for each subject some important ROIs, for example Cerebellum and Putamen, and we drew the single concentrations relative to each compartment, in order to find possible analogies among the different regions. We tried to draw the single concentrations without the correction term, but in this case the one relative to the irreversible trapping became overriding (arriving to $200 \div 300$ $[\frac{kBq}{ml}]$) and covered the others: so we multiplied the values of concentration for V_b, if they were relative to the blood compartment, or for $1 - V_b$, if they were refered to tissue. From the observation of the results, the concentration values relative to the tissue compartment (which is the most important one for our studies, since it represents the specific binding) confirm the previous result in regard to the ability of this model to correlate with the physiological information about the distribution of the receptors within the brain. In fact Putamen and Caudate Nucleus present higher values than Cerebellum or Anterior Cingulate Gyrus, and in particular for these regions the curves present a more rapid course, index of the low amount of binding sites. Moreover, the values found for the dyskinetic patients are lower than the ones of the unique non-dyskinetic subject 1711: other Parkinson's desease subjects are required to check on this result, since for Putamen we expect an opposite conclusion. About the blood reversible compartment, if present, we can notice that it is a predominant component for subject 2241, who presents higher values, an elevate area under the curve (AUC) and a slower decrease in comparison with 1711. Inside the same subject, Putamen and Cerebellum do not change significantly, as expected from the values of their relative V_{dblood}. Finally, the concentration curves relative to the irreversible compartment are similar among the three subjects who present the trapping process and they assume high values, as we can see in Figure 7.4, index that the non-specific binding inside the blood vessels is significant for this tracer. It appears clearly from the observation of this figure that the information obtained with this tracer is vascular and not relative to tissue, and this can be considered a negative characteristic of the tracer.

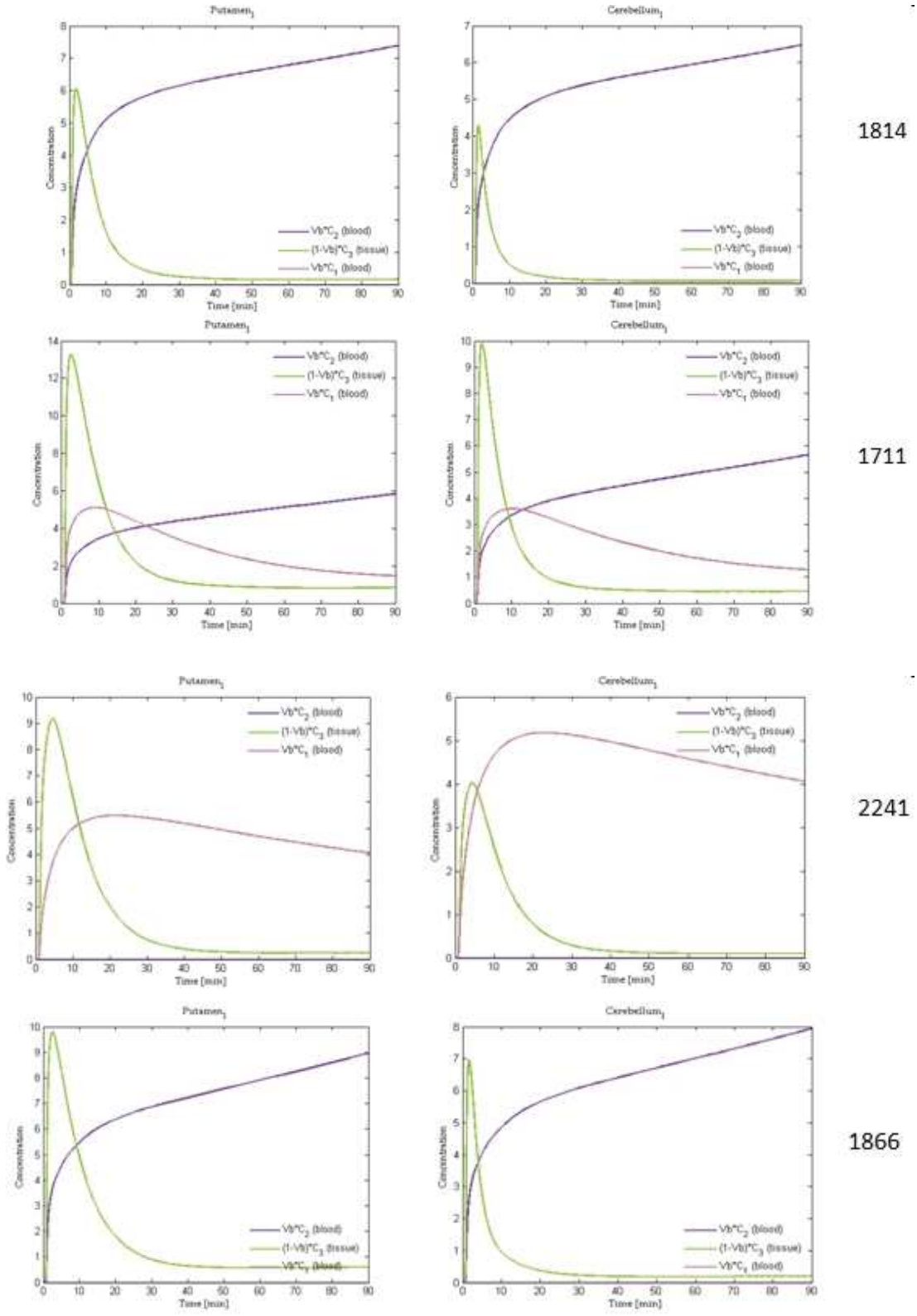

Figure 7.4: Concentration curves relative to two ROIs, Putamen$_l$ and Cerebellum$_l$, considering separately each compartment

For each subject, we also evaluated the striatum to cerebellum radioactivity concentration ratios, since, in previous studies [10], it was used as an index of in vivo binding of the tracer to A_{2A} receptors. As already seen in Chapter 3, studies on rats have found that at the time of the maximum uptake (between 5 and 15 mins after the injection) the ratio was 4.6 while the PET experiment on monkeys brain showed values two times lower than those measured in rats (the maximum value was 2.2). However they expected a higher ratio for the in vivo measurament in human brain, but in our analysis this expectation is not respected. In fact, using the single concentration curves relative to the tissue compartment, we calculated this ratio and we found that it was 2.2÷2.6 (between 10 and 15 mins after the tracer injection) for subjects 1814, 1711 and 2241, in line with the results on monkeys, only for 1866 it was 4.5. So these results, even if the number of subjects is limited and for one of the them the value is significantly different, suggest that this tracer also in human subjects presents a good kinetic profile but a low striatum to cerebellum ratios and this could be problematic for its use.

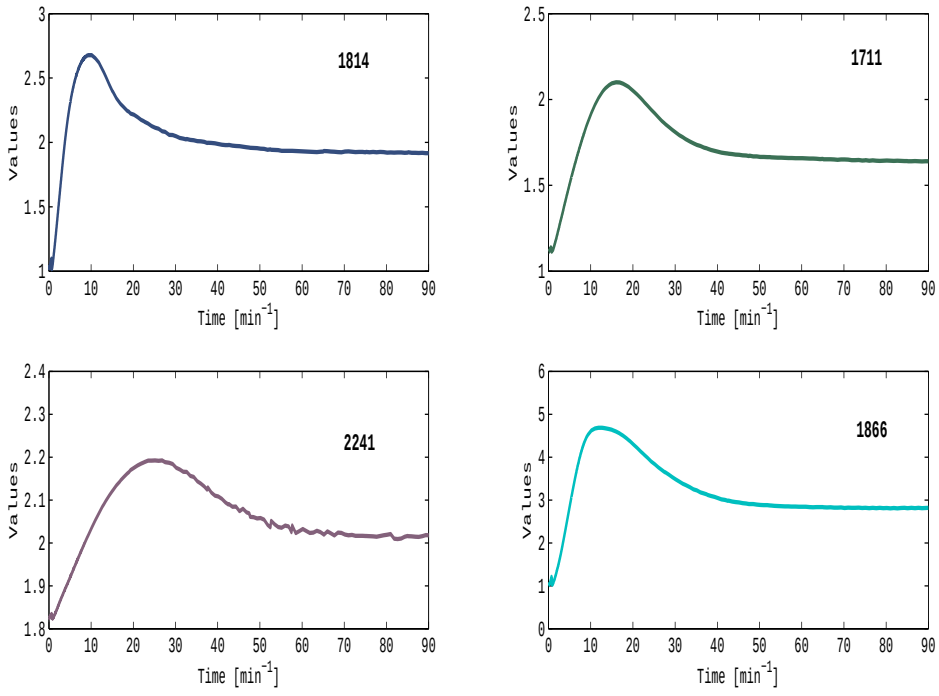

Figure 7.5: Striatum to Cerebellum ratios

Chapter 8

Conclusions

[^{11}C]SCH442416 is a PET tracer that is specific for the adenosine A_{2A} receptors, which are only locally expressed within the brain, and gave good results in the preclinical studies on rats and monkeys. To investigate its characteristics, distribution and activity we included in our work the data of six subjects (3 dyskinetic Parkinson's disease subjects, 2 Parkinson's disease subjects and 1 healthy control), even if, after a first qualitative analysis, we discovered that two of them (the healthy volunteer and one non-dyskinetic patients) had problems during the execution of the study and so their data were not reliable and useful to make the different comparisons.

We performed the analysis of the tracer at region of interest level and, to extract the useful information from the data, different approaches were used. An input-output technique, usually refered to as Spectral Analysis, was first used, both to quantify some variables of interest and, especially, to define the most appropriate compartment model to describe our set of data. In fact, starting from the interpretation of the obtained spectrum, this approach is suitable to find the minimum number of compartments needed to explain the kinetics of the tracer in the brain, even if it can not say anything about their connections. The traditional SA approach gives on our data good results and, despite some different behaviours among the subjects, it detects the reversible components and the presence of a significant irreversible process within the system. Also the fit and the precision of the variables of interest are good, even if the use of a discrete fixed beta grid

and the presence of noise create some problems, like the phantom components, the double lines close to the real value, the shift of the irreversible line (i.e the one for $\beta = 0$) and a split spectrum.

To overcome some of these problems, e.g the great number of intermediate components for some subjects, we decided to apply a new SA technique, called SAIF: it uses prior information concerning irreversibility of trapping of the tracer as well as components that cannot be distinguished from blood (in fact, the values for $\beta \to \infty$ or very close are considered vascular components and they are reasumed in the blood volume term Vb). This information determinates the value of a cut-off interval that the SAIF uses to select the range of the equilibrating components distinguishable in the data to be analyzed. This method applied to our dataset gives as previously good results and fits, and in this case the number of detected components is reduced, since it is able to eliminate the problem of double lines. Moreover the precisions of the α values, and not only of the estimated macroparameters, are good (while with the traditional SA they were detected with very low precisions). Following the guidelines dictated by the SA approach, we tried to define the most suitable compartmental model, in order to describe the kinetics of our PET tracer data: the traditional models present in literature, as 3K or 5K model, were not suitable in our case and in particular they had not a physiological explanation. After the discovery, on summed PET images, of large vascular areas and of a large amount of rapid metabolites, we decided to propose some innovative compartmental structures for this tracer. In particular we focused our attention on three models (Model 1, Model 3 and Model 4), two of whom with a double arterial plasma input function, and through the comparison of their results we tried to choose the best one. Even if Models 3 and 4 provided good fits of the data and their distribution volume macroparameter was correlated with the physiological information about the selective distribution of A_{2A} sites within the brain, we decided to reject them, because of their high intra-subject variability and the marked disagreement between the results of these compartmental structures and their correspondent I/O model. Moreover, for Model 3 the irreversible process due to the metabolites seemed to be very slow, while Model 4 was not able to estimate the trapping for some subjects, even if the traditional SA on the

same ones detected a marked irreversible component. Other studies are required to understand how it is possible to formulate new compartmental models for this tracer taking into account the metabolites presence.

Instead Model 1 presented a precise concordance with the results of SA, as well as the previous characteristics quoted for the other two models, even if, in this case, for some subjects the model estimated curves under/overstimated the data in some parts. Moreover this structure is in agreement with a previous model present in literature to describe the kinetics of [^{11}C]SCH442416 and proposed by Brooks and coworkers, in fact their compartmental model presents a fast, specific, reversible compartment and a slow, irreversible, non-specific one. Even if we have for some subjects the presence of another reversible compartment, also in our structure we suppose that the trapping is relative to blood and so it represents a non-specific binding of the tracer. So despite the low number of subjects that we involved in our study, the results and the performance of the various techniques that we applied lead us to propose Model 1 as the most parsimonious compartmental model to describe the kinetics of the tracer in brain areas.

Further studies, involving a large number of dyskinetic, non-dyskinetic and healthy patients, are required to confirm the reliability of this model, to investigate the role of the second reversible blood compartment present for some subjects and to find possible correlations between the different pathologies of these subjects. Finally, they are also necessary to demonstrate the effective potentialities of [^{11}C]SCH442416 for the invivo imaging of A_{2A} receptors and to analyze if it is possible to use adenosine receptor antagonists, like this one, as new powerful treatments for Parkinson's disease.

Appendix A

While the traditional compartmental models, like the 3K, 4K and 5K models, have been at lenght investigated [21], Model 1 is a new and innovative structure: in this section we will derive its equations and study its identifiability.
To derive Model 1 in terms of concentration, we start by formulating the model in terms of mass: the mass representation is shown in Figure 8.1.

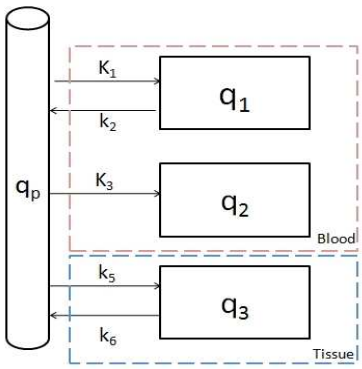

Figure 8.1: Model 1 in term of mass, q_p, q_1, q_2, q_3

The mass balance equations are

$$\begin{aligned} \frac{dq_1(t)}{dt} &= K_1 q_p(t) - k_2 q_1(t) & q_1(0) &= 0 \\ \frac{dq_2(t)}{dt} &= K_3 q_p(t) & q_2(0) &= 0 \\ \frac{dq_3(t)}{dt} &= k_5 q_p(t) - k_6 q_3(t) & q_3(0) &= 0 \end{aligned} \tag{8.1}$$

where q_p, q_1 and q_2 represent the amount of tracer in plasma and blood space, while q_3 is the amount in tissue. Defining $q(t) = C(t)V$ and supposing that the plasma concentration has a V_p volume, that the two compartments relative to blood have a V_{blood} volume and the tissue compartment has a generic V_T volume,

the system 8.1 can be written as:

$$\begin{aligned}
&\frac{dC_1(t)}{dt} \cdot V_{blood} = K_1 C_p(t) V_p - k_2 C_1(t) V_{blood} && V_{blood} C_1(0) = 0 \\
&\frac{dC_2(t)}{dt} \cdot V_{blood} = K_3 C_p(t) V_p && V_{blood} C_2(0) = 0 \\
&\frac{dC_3(t)}{dt} \cdot V_T = k_5 C_p(t) V_p - k_6 C_3(t) V_T && V_T C_3(0) = 0
\end{aligned} \tag{8.2}$$

Remembering that

$$\begin{aligned}
V_{blood} &= V_p + V_{RC} \\
H &= \frac{V_{RC}}{V_{blood}}
\end{aligned} \tag{8.3}$$

where H is the haematocrit, i.e the proportion of blood volume occupied by red blood cells, we have that $V_p = (1 - H)V_{blood}$. Dividing the equations 8.2 for the volume term, the new system is:

$$\begin{aligned}
\frac{dC_1(t)}{dt} &= K_1(1 - H)C_p(t) - k_2 C_1(t) \\
\frac{dC_2(t)}{dt} &= K_3(1 - H)C_p(t) \\
\frac{dC_3(t)}{dt} &= k_5 C_p(t)\frac{V_p}{V_T} - k_6 C_3(t)
\end{aligned} \tag{8.4}$$

Defining $K_5 = k_5 \frac{V_p}{V_T}$, which is the reason why K_5 as a different unit of measurement, $\frac{ml_{plasma}}{ml_{tissue}} \cdot min^{-1}$, and including the (1-H) term inside the rate costants k_1 and k_3, we finally obtain the equation 5.24 of Chapter 5, i.e:

$$\begin{aligned}
&\frac{dC_1(t)}{dt} = k_1 C_p(t) - k_2 C_1(t) && C_1(0) = 0 \\
&\frac{dC_2(t)}{dt} = k_3 C_p(t) && C_2(0) = 0 \\
&\frac{dC_3(t)}{dt} = K_5 C_p(t) - k_6 C_3(t) && C_3(0) = 0
\end{aligned} \tag{8.5}$$

The total amount measured by PET, q(t), is the summation of the amounts present in the vascular and tissue part of the ROI, i.e $q(t) = q_1(t) + q_2(t) + q_3(t) + q_p(t)$ and expressing this equation in terms of concentrations we have:

$$C(t)V_{TOT} = C_1(t)V_{blood} + C_2(t)V_{blood} + C_3(t)V_T + C_b(t)V_{blood} \tag{8.6}$$

Remembering that

$$\begin{aligned} V_{TOT} &= V_{blood} + V_T \\ V_b &= \frac{V_{blood}}{V_{TOT}} \end{aligned} \tag{8.7}$$

the equation 8.6, after the division for the term V_{TOT}, can be written as:

$$\begin{aligned} C(t) &= C_1(t)V_b + C_2(t)V_b + C_3(t) \cdot \frac{V_T}{V_{TOT}} + C_b(t)V_b \\ &= [C_1(t) + C_2(t)]V_b + C_3(t) \cdot \frac{V_{TOT} - V_{bloood}}{V_{TOT}} + C_b(t)V_b \\ &= [C_1(t) + C_2(t)]V_b + C_3(t)(1 - V_b) + C_b(t)V_b \end{aligned} \tag{8.8}$$

The system of equations 8.5, which describes Model 1, is a priori uniquely identifiable, if it is defined in this way and with the parameterization relative to the parameter k_5. We use the transfer function method to analyze the idenfiability of this model: taking Laplace transforms of Equations 8.5 and rearranging them we have

$$\begin{aligned} sC_1(s) &= k_1C_p(s) - k_2C_1(s) \\ sC_2(s) &= k_3C_p(s) \\ sC_3(s) &= K_5C_p(s) - k_6C_3(s) \end{aligned} \tag{8.9}$$

Solving for C_1, C_2 and C_3

$$\begin{aligned} C_1(s) &= \frac{k_1}{s + k_2}C_p(s) \\ C_2(s) &= \frac{k_3}{s}C_p(s) \\ C_3(s) &= \frac{K_5}{s + k_6}C_p(s) \end{aligned} \tag{8.10}$$

So, the Laplace transform of the total concentration C(t) can be written as:

$$\begin{aligned} C(s) =& \frac{s^2(k_1V_b + k_3V_b + K_5 - K_5V_b) + s(k_1k_6V_b + k_2k_3V_b + k_3k_6V_b + k_2K_5 - k_2K_5V_b)}{s^3 + s^2(k_2 + k_6) + s(k_2k_6)} \\ &+ \frac{k_2k_6k_3V_b}{s^3 + s^2(k_2 + k_6) + s(k_2k_6)} \cdot C_p(s) + V_bC_b(s) \end{aligned} \tag{8.11}$$

The exhaustive summary of the model is:

$$\begin{aligned}
\phi_1 &= (k_1 + k_3 - K_5)V_b + K_5 \\
\phi_2 &= (k_1k_6 + k_3k_2 + k_3k_6 - k_2K_5)V_b + k_2K_5 \\
\phi_3 &= k_2k_6k_3V_b \\
\phi_4 &= k_2 + k_6 \\
\phi_5 &= k_2k_6 \\
\phi_6 &= V_b
\end{aligned} \tag{8.12}$$

where $\phi_1, \cdots, \phi_6$ are the known observational parameters: the model is identifiable since it is possible to solve for all the six unknown parameters of the model.

Bibliography

[1] S.Latini and F.Pedata. Adenosine in the central nervous system: release mechanisms and extracellular concentrations. *Journal of Neurochemistry*, 79:463-84, 2001.

[2] S.N. Schiffmann, G. Fisone, R. Moresco, R.A. Cunha and S. Ferré. Adenosine A_{2A} receptors and basal ganglia physiology. *Progress in Neurobiology*, 83: 277-92, 2007.

[3] V. Ralevica and G. Burnstock. Receptors for Purines and Pyrimidines. *Pharmacological Reviews*, 50(3): 413-91, 1998.

[4] B. Fredholm, R.A. Cunha and P. Svenningsson. Pharmacology of adenosine A_{2A} receptors and therapeutic applications. *Current Topics in Medicinal Chemistry*, 3(1):1349-64, 2003.

[5] P. Popoli, D. Blum, A. Martire, C. Ledent, S. Ceruti and MP. Abbracchio. Functions, dysfunctions and possible therapeutic relevance of adenosine A_{2A} receptors in Huntingtons disease. *Progress in Neurobiology*, 81: 331-48, 2007.

[6] K. Xu, E. Bastia and M. Schwarzschild. Therapeutic potential of adenosine A_{2A} receptor antagonists in Parkinsons disease. *Pharmacology Therapeutics*, 105: 267310, 2005.

[7] M. Morelli, AR. Carta and P. Jenner. Adenosine A_{2A} receptors and Parkinson's disease. Adenosine Receptors in Health and Disease: 589-608, 2009.

[8] P. Blake, B. Johnson and JW. VanMeter. Positron Emission Tomography (PET) and Single Photon Emission Computed Tomography (SPECT): Clinical Applications. *J Neuro-Ophthalmol*, 23(1): 34-41, 2003.

[9] M.E. Phelps. Positron emission tomography provides molecular imaging of biological processes. *Proceedings of the National Academy of Science*, 97(16): 9226-233, 2000.

[10] S. Todde, R. Moresco, P. Simonelli, PG. Baraldi et al. Design, Radiosynthesis, and Biodistribution of a New Potent and Selective Ligand for in Vivo Imaging of the Adenosine A_{2A} Receptor System Using Positron Emission Tomography. *J.Med.Chem*, 43: 4329-362, 2000.

[11] J.C. Price. Principles of tracer kinetic analysis. *Neuroimag Clin N Am*, 13: 689-704, 2003.

[12] R. Moresco, S. Todde, S. Belloli, P. Simonelli et al. In vivo imaging of adenosine A_{2A} receptors in rat and primate brain using [^{11}C]SCH442416. *Eur J Nucl Med Mol Imaging*, 32(4): 405-13, 2005.

[13] T. Mihara, A. Noda, H. Arai, K. Mihara, A. Iwashita et al. Brain Adenosine A2A Receptor Occupancy by a Novel A_1/ A_{2A} Receptor Antagonist, ASP5854, in Rhesus Monkeys: Relationship to Anticataleptic Effect. *J Nucl Med*, 49(7): 1183-88, 2008.

[14] D.J. Brooks, S. Papapetropoulos,F. Vandenhende et al. An Open-Label, Positron Emission Tomography Study to Assess Adenosine A_{2A} Brain Receptor Occupancy of Vipadenant (BIIB014) at Steady-State Levels in Healthy Male Volunteers. Clinical Neuropharmacolog, 33(2): 55-60, 2010.

[15] V.J. Cunningham and T. Jones. Spectral analysis of dynamic PET studies. *J Cereb Blood Flow Metab*, 13(1):1523, 1993.

[16] F. Turkheimer, R.M. Moresco, G. Lucignani, L. Sokoloff, F. Fazio, and K. Schmidt. The use of spectral analysis to determine regional cerebral glucose utilization with positron emission tomography and [18F]fluorodeoxyglucose: theory, implementation, and optimization procedures. *J Cereb Blood Flow Metab*, 14(3):40622, 1994.

[17] F. Turkheimer, L. Sokoloff, A. Bertoldo, G. Lucignani, M. Reivich, J. L. Jaggi, and K. Schmidt. Estimation of component and parameter distributions in spectral analysis. *J Cereb Blood Flow Metab*, 18(11):121122, 1998.

[18] M. Veronese, A. Bertoldo, S. Bishu, A. Unterman, G. Tomasi, C.B Smith and K.C. Schmidt. A spectral analysis approach for determination of regional rates of cerebral protein synthesis with the L-[1-11C]leucine PET method. *J Cereb Blood Flow Metab*, 2010.

[19] V.J Cunningham, E.A. Rabiner, J.C. Matthews, R.N. Gunn, S.Zamuner and Antony D. Gee. Kinetic analysis of neuroreceptor binding using PET. *International Congress Series*, 1265: 1224, 2004.

[20] F. Calon, M. Dridi et al. Increased adenosine A_{2A} receptors in the brain of Parkinson's disease patients with dyskinesias. *Brain*, 127(5): 1075-1084, 2004.

[21] A. Bertoldo, P. Peltoniemi, V. Oikonen, J. Knuuti, P. Nuutila and C. Cobelli. Kinetic modeling of [18F]FDG in skeletal muscle by PET: a four-compartment five-rate-constant model. *AJP-Endocrinol Metab*, 281: 524-36, 2001.

Acknowledgments

First of all I want to thank my professor Alessandra Bertoldo for the possibility to write my thesis with her. She spent a lot of time with me, supporting me in all the moments: I learned a lot during this time and I hope to work again with her in future.
A special thank also to Gaia and Mattia, for reviewing my thesis and for their help during these long months.
My greatful thanks to my family, who supported me with all I have done during my life: you are always in my thoughts, especially my brother Andrea, who makes me glad every single day.
Last but not least, I wish to thank a special person, Alessandro: he always supports and encourages me during this hard period, with patience and his importante presence. You are always in my heart and I am very happy to have the possibility to share my life together with you.